ROYAL INSTITUTE
OF TECHNOLOGY

Permanent-Magnet Synchronous Machines with Non-Overlapping Concentrated Windings for Low-Speed Direct-Drive Applications.

Florence Meier

Royal Institute of Technology
School of Electrical Engineering
Electrical Machines and Power Electronics

Stockholm 2008

Submitted to the School of Electrical Engineering, KTH, in partial fulfilment of the requirements for the degree of Doctor of Philosophy.

Copyright © Florence Meier, Sweden 2008
Printed in Sweden
Universitetsservice US AB

TRITA-EE 2008:041
ISSN 1653-5146
ISBN 978-91-7415-089-6

Abstract

Many geared electric drives can benefit from removing the gearbox and driving directly the load at low speed using a permanent-magnet synchronous machine (PMSM). PMSMs with non-overlapping concentrated windings are particularly attractive in low-speed direct drives since they allow, among other advantages, a high number of poles with a limited number of slots. Therefore, this thesis is dedicated to PMSMs with non-overlapping concentrated windings designed for low-speed direct-drive applications.

First, the design features specific to PMSMs with non-overlapping concentrated windings are presented and illustrated with examples based on finite-element (FE) simulations. Especially, it is shown that the selections of the stator core manufacturing method, the number of winding layers, the combination of pole and slot numbers, and the geometry of the tooth tips are crucial during the design stage of the machine.

Second, the benefits of removing the gearbox in a 4.5 kW, 50 rpm mixer used in a waste-water treatment plant are investigated. With its PMSM having buried ferrite magnets and concentrated windings, the designed direct-drive mixer has a higher efficiency than the commercialized geared mixer, but it is also heavier and more expensive due to the larger required housing, shaft and seals. In addition, the cost of the stator core and coil assembly was also higher than expected. Therefore, the difficulties in manufacturing a stator core with concentrated windings are investigated. Mainly due to economical aspects, no prototype motor has been built for the direct-drive mixer.

Finally, measurements on a prototype motor at disposal having a large constant-power speed range are performed. Three methods to measure the inductances without using a position sensor are provided and compared. One of the methods is a new test at load conditions to determine the inductance without the knowledge of the rotor position. Results from this method agree well with a conventional blocked rotor test, as well as with results from 3D-FE simulations. Furthermore, the measurements of the magnetic flux obtained with search coils placed in different parts of the stator are analyzed. The analysis allows highlighting the zigzag flux flowing from one magnet to another through a tooth tip, which is characteristic of PMSMs

with non-overlapping concentrated windings. It is shown that this zigzag flux leakage causes high iron losses in the tooth tips that represent approximately 50 % of the stator iron losses under field weakening operation. Using these measurements, the 3D-FE model of the prototype is also validated thoroughly.

Preface

The work presented in this thesis has been carried out at the division of Electrical Machines and Power Electronics, School of Electrical Engineering, Royal Institute of Technology (KTH), between October 2002 and July 2008. It is a project within the High Performance Electrical Machines and Drives (HPD) research program of the Center of Excellence in Electric Power Engineering. As one of the pilot projects within the HPD program, the main objective is to investigate and develop new concepts of electrical drives in close cooperation with industrial partners. ITT Water & Wastewater, Danaher Motion, and Höganäs have been involved in the project.

The following remarks may ease the reading of this thesis:

- p is the number of poles and not the number of pole pairs as it is in many publications.
- In this thesis, the term "concentrated windings" always refers to windings that are non-overlapping.
- Measurements have been performed on a prototype motor that is described in Appendix C. This motor is referred to as the "prototype" in Chapters 5, 6 and 7. No prototype has been built for the mixer application which is the subject of Chapter 4.
- This thesis is available for download in pdf-format at http://www.eme.ee.kth.se/publications.php. The pdf-file offers the possibility to view the pictures in color, zoom on them, do a keyword search, etc. Other publications from the author of this thesis (F. Meier or F. Libert) are also available on this site.
- The author's publications are distinguished from the other publications by the use of Roman numbers. They are listed in Section 1.5 (Chapter 1).

Acknowledgments

Since I started to work on my Ph.D. project, several people have been involved in the project. Hereby, I kindly acknowledge them.

First of all I thank my supervisor, Ass. Prof. Juliette Soulard, for her guidance, support, enthusiasm and trust. I am also very grateful to my second supervisor, Prof. Chandur Sadarangani, for his friendly approach in our discussions throughout the project, as well as his last minute reading of the thesis.

This Ph.D. project has been made possible with the financial support from the HPD program. I would like to thank the staffs from ITT Water & Wastewater, Danaher Motion, and Höganäs that have been involved in my project. From ITT Water & Wastewater, I particularly thank Dr. Jörgen Engström, Börje Ståhl, Dr. Øystein Krogen and Johan Hallberg with whom I enjoyed collaborating. I thank Danaher Motion for lending the prototype motor and its drive to me and helping me with the installation. Especially I thank Lic. Eng. Hans-Olof Dahlberg, Thord Nilson and Martin Giles. From Höganäs, I thank Dr. Lars-Olov Pennander and Lars Hultman for interesting discussions.

I further would like to thank Prof. Hans-Peter Nee for reading the thesis and for his valuable comments. Dr. Pia Salminen from Lappeenranta University of Technology is acknowledged for our collaboration that resulted in a publication. I thank Adam Pride from IMRA Europe for sharing his knowledge and the interesting discussions that followed.

Tommy Kjellqvist, Dr. Sylvain Châtelet, Dr. Peter Thelin, Lic. Eng. Mats Leksell, Jan Timmerman and Olle Brännvall are acknowledged for their help in the laboratory.

Thanks to Eva and Emma Pettersson for the help with the administrative work. Thanks also to Brigitt Högberg for successfully registering my courses and to Peter Lönn for the computer support.

I am very grateful to Dr. Oskar Wallmark for proof-reading my thesis as well as several of my publications and giving me various useful tips. I thank my former office mate Dr. Robert Chin for his help in the project and diverse friendly advices, as well as for sharing all these unhealthy cakes...

I thank the whole personal at EME as well as the former employees for the friendly atmosphere at EME.

Finally, I would like to thank my family. My husband Stephan Meier helped me in various ways in my project, from the scrupulous proof-reading of some of my publications to the help in the laboratory and with Emetor. Thanks also to Stephan for his support, endless encouragement and love and for being such a great dad which helped me to finish more quickly! Even my little son Simon helped me in his way. I believe that everything became much easier in the project after his birth, that is to say, thanks to him!

Florence Meier
Stockholm,
July 2008

Contents

1 Introduction

1.1 Background

Nowadays, electrical motors account for 65 % of the worldwide energy consumption [1]. As environmental concern increases, electrical drives with higher efficiency are desirable. Thus, replacing conventional induction machines with PMSMs has recently gained great interest. Indeed, PM machines have no rotor winding which results in lower copper losses and therefore feature a higher efficiency than induction machines.

For low-speed applications, below 500 rpm, PM machines may further eliminate the need of a gearbox. To adapt the speed and torque of the machine, a gearbox is traditionally coupled to a standard induction machine. It is advantageous to remove this mechanical element because it is costly, decreases the drive efficiency, and needs maintenance. Low-speed (or high-speed) drives without a gearbox are termed *direct drives*, since the machines are directly coupled to the load.

1.2 Objectives

The primary objective of the project is to define a suitable drive with a PMSM for a 4.5 kW, 50 rpm mixer used for waste-water treatment. This direct drive should replace an induction motor coupled to a gearbox in the commercialized mixer. A study carried out by the author illustrated the benefits of using PMSMs with non-overlapping concentrated windings compared to PMSMs with distributed windings when the number of poles is high [VI]. Therefore, the focus in this thesis is put on the design of PMSMs with non-overlapping concentrated windings as well as their manufacturing.

The second objective is to perform measurements on a prototype motor with non-overlapping concentrated windings and analyze them. A special concern is given to the machine's inductances and stator iron losses.

1.3 Main contributions of the thesis

In this thesis, it is shown that PMSMs with non-overlapping concentrated windings are particularly suitable for low-speed direct-drive applications.

The thesis relates the design features specific to PM machines with non-overlapping concentrated windings based on the author's work and relevant references. Especially, the relation between the combination of pole and slot numbers and the winding factor as well as the unbalanced magnetic pull are studied.

The difficulties in manufacturing a stator core with non-overlapping concentrated windings are investigated. It is shown how the choice of the manufacturing method influences the design and performance of PMSMs with such windings.

Different methods to measure the inductances without any position sensor are presented, compared and analyzed. A new method to find the inductances from a load test without using a position sensor is described.

Original measurements of the magnetic flux in a prototype with non-overlapping concentrated windings are presented and analyzed. It is shown that the inter-pole flux leakage through a tooth tip, that is particular to PMSMs with non-overlapping concentrated windings, is responsible for most of the stator iron losses during flux-weakening operation. The finite-element model is validated globally (e.g. back-EMF, torque) as well as locally (e.g. flux density in a tooth or yoke).

1.4 Outline of the thesis

The thesis is organized as follows:

Chapter 2 gives an overview of the low-speed direct drives existing today or under investigation.

Chapter 3 focuses on the design of PM machines with non-overlapping concentrated windings.

Chapter 4 presents the design of a PM motor for a low-speed direct-drive mixer used in waste-water treatment plant.

Chapter 5 investigates the manufacturing methods of stator cores from PM machines with non-overlapping concentrated windings.

Chapter 6 discusses the inductance measurements performed on the prototype motor.

Chapter 7 presents the measurements performed under flux-weakening operation as well as the analysis of the magnetic flux measurements in the prototype machine.

Chapter 8 concludes the thesis and presents possible future work.

1.5 List of publications

Part of the work reported in this thesis has been published in international conference proceedings or journals:

[I] **F. Meier** and J. Soulard, *"Inductance Measurements on a Permanent-Magnet Synchronous Motor Without Position Sensors"*, preliminary accepted for publication in IEEE Transactions on Magnetics, 2008.

[II] **F. Meier** and J. Soulard, *"Analysis of Flux Measurements on a PMSM With Non-Overlapping Concentrated Windings"*, accepted for publication in the proceedings of IEEE Industry Applications Conference, 43^{th} IAS Annual Meeting, 2008.

[III] **F. Meier** and J. Soulard, *"dq Theory Applied to a Permanent Magnet Synchronous Machine with Concentrated Windings"*, proceedings of IET International Conference on Power Electronics, Machines and Drives (PEMD), pp. 194-198, 2008.

[IV] **F. Libert**[1] and J. Soulard, *"Manufacturing Methods of Stator Cores with Concentrated Windings"*, proceedings of IET International Conference on Power Electronics, Machines and Drives (PEMD), pp. 676-680, 2006.

[V] **F. Libert** and J. Soulard, *"Design Study of Low-Speed Direct-Driven Permanent-Magnet Motors with Concentrated Windings"*, proceedings of the 6^{th} International Symposium on Advanced Electromechanical Motion Systems, (Electromotion), 2005.

[VI] **F. Libert**, *"Design, Optimization and Comparison of Permanent Magnet Motors for a Low-Speed Direct-Driven Mixer"*, Licentiate thesis, Department of Electrical Machines and Power Electronics, Royal Institute of Technology, 2004.

[VII] **F. Libert** and J. Soulard, *"Design Study of Different Direct-Driven Permanent-Magnet Motors for a Low Speed Application"*, proceedings of the Nordic Workshop on Power and Industrial Electronics (NORpie), 2004.

[1] Maiden name of the author of the present thesis.

[VIII] **F. Libert** and J. Soulard, *"Investigation on Pole-Slot Combinations for Permanent Magnet Machines with Concentrated Windings"*, proceedings of the International Conference on Electrical Machines, (ICEM), 2004.

[IX] **F. Libert** and J. Soulard, *"Design Study of a Direct-Driven Surface Mounted Permanent Magnet Motor for Low Speed Application"*, proceedings of Symposium on Advanced Electromechanical Motion Systems (Electromotion), 2003.

The author has also participated in the following publications:

[X] O. Wallmark, P. Kjellqvist and **F. Meier**, *"Analysis of Axial Leakage in High-Speed Slotless PM Motors for Industrial Hand Tools"*, accepted for publication in the proceedings of IEEE Industry Applications Conference, 43^{th} IAS Annual Meeting, 2008.

[XI] **F. Meier**, S. Meier and J. Soulard, *"Emetor – An educational web-based design tool for permanent-magnet synchronous machines"*, accepted for publication in the proceedings of the International Conference on Electrical Machines, (ICEM), 2008.

[XII] P. Salminen, **F. Libert**, J. Pyrhönen and J. Soulard, *"Torque Ripple of Permanent Magnet Machines with Concentrated Windings"*, proceedings of the 6^{th} International Symposium on Electromagnetic Fields in Mechatronics, Electrical and Electronic Engineering, (ISEF), 2005.

[XIII] **F. Libert**, J. Soulard and J. Engström, *"Design of a 4-pole Line Start Permanent Magnet Synchronous Motor"*, proceedings of the International Conference on Electrical Machines, (ICEM), 2002.

Chapter 3 completes the work published in [VI, VIII]. Chapter 4 summarizes and completes the publications [V-VII]. Chapter 5 covers [IV], Chapter 6 [I, III], and Chapter 7 [II].

2 Low-speed direct drives

This chapter is a review of the state of the art in low-speed direct drives. After having presented the general advantages of direct drives, various applications are described. For each application, its specific advantages are mentioned followed by examples of the required power and speed of the electrical machine. Various direct-drive solutions which are already commercialized or under investigation are then shortly described along with the machine topology. Finally, some features specific to low-speed electrical machines for direct-drive applications are presented.

2.1 Advantages of direct drives

Many applications require a low rotating speed and a high torque. Usually, conventional machines with speeds from 1000 to 3000 rpm are connected to gearboxes, in order to achieve the required low speed and high torque (Figure 2.1.a). The emergence of PM machine technology offers today another alternative. PM machines can rotate directly at low speed and high torque, making it possible to eliminate the gearbox in the drive (Figure 2.1.b).

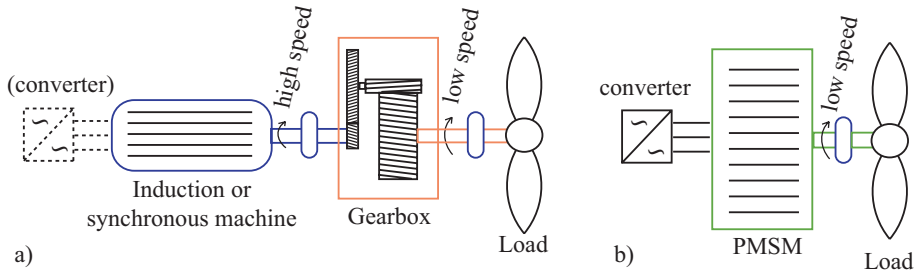

Figure 2.1: a) Geared drive; b) Direct drive.

Direct drives have many advantages over geared drives, mostly coming from the simplification of the transmission system. These advantages include [2, 3]:

- Reduced maintenance - A gearbox requires maintenance. Indeed, it needs to be regularly lubricated in order to minimize friction.
- Higher reliability - Without gearbox, important sources of failures are eliminated and the drive can have a longer lifetime.
- Reduced noise - A gearbox and other mechanical parts of the transmission system such as belts or pulleys are sources of noise. With fewer mechanical parts, the direct drives may thus be less noisy.
- Higher efficiency - Removing the gearbox means also removing a potential source of losses. The losses in the gearbox are mostly generated by friction between the gears.
- Reduced weight - A direct drive can be made lighter than a geared drive.

Direct drives can procure other advantages specific to the application, as will be seen in the examples.

2.2 Examples of low-speed direct-drive applications

2.2.1 Wind turbines

The number of wind turbine installations has increased greatly during the past years. Most of the installed wind turbines have a gearbox enabling a generator rotating at high speeds. In case of wind turbines, the main benefit of a direct drive is the reduction of failures and maintenance. In [4], a survey of statistical data of wind power turbine failures and downtime shows that the gearbox is the most troublesome component in a typical turbine: The gearbox is responsible for 20 % of the total downtime and requires in average 256 hours of reparation time per failure.

Depending on the turbine size, the power of the generator can be from a few kilowatts to several megawatts. The shaft of large turbines rotates at a speed of approximately 15 rpm when the wind is optimum.

Direct-drive wind turbines are widely studied and some are already manufactured. Different generator types can be used in a direct drive (see Appendix A for the description of different machines topologies). Some manufacturers utilize induction or synchronous machines. An example is Enercon that uses a direct-drive

doubly-fed induction generator (DFIG) in a 2 MW turbine (Figure 2.2). However, PM machines enable a significant weight reduction compared to DFIGs, which is of importance when the generator has to be lifted into the nacelle. Some examples of direct-drive wind-turbine projects with PM generators are listed below sorted by machine topology:

- Radial-flux PM (RFPM) - RFPM generators are quite common in direct-drive wind turbines. Harakosan commercializes one of the largest direct-drive wind turbines with its 2 MW Z72. Details on the design of this wind turbine along with its RFPM generator can be found in [5]. In another interesting project, VG Power proposes a RFPM generator with a reduced weight obtained by placing the bearing in the airgap. A 3 MW prototype is intended to be constructed, following the successful testing of a downscaled prototype [6].
- Axial-flux PM (AFPM) - AFPM generators are also widely investigated [7–9] and manufactured by some wind-turbine producers such as Jeumont Industry.
- Transverse-flux PM (TFPM) - TFPM are interesting because of their high torque density [10]. To the author's knowledge, no large wind turbines (over 1 MW) equipped with TFPM generators are currently installed. However, Éocycle Technologies commercializes TFPM generators with a power of up to 10 kW and intends to produce larger generators. The topology of these generators with claw poles partly in soft magnetic composites (SMC) is described in [11]. Another original TFPM topology is investigated in [12].

Figure 2.2: Enercon E-82 2 MW wind turbine [13].

2.2.2 Marine propulsion

Most of the cruise ships manufactured today have an electric propulsion [14]. Among other advantages, the electric propulsion offers a better passenger comfort and is more reliable than conventional drives with diesel engines or gas turbines [15]. Direct-drive PM motors also tend to replace synchronous machines connected to gearboxes. For this application, the main advantages of the direct drive is its lower weight and the gain in maneuverability for the ship. The PM motor can be placed in a rotatable pod directly connected to the propeller which makes it possible to change the position of the propeller (and thus of the ship) very easily and smoothly.

The largest ships require motors with a rated power over 10 MW. The speed of the propeller is then lower than 200 rpm [3, 14].

The most famous solution for direct-drive ship propulsion is ABB's azimuthing podded propulsor named Azipod ([16], Figure 2.3). RFPM motors are used in Azipods. Depending on the size of the pod, the motors have a rated power between 400 kW and 5 MW, run between 150 to 500 rpm and have 10 to 16 poles [3]. Other solutions have also been investigated, such as AFPM motors [15] or TFPM motors [17].

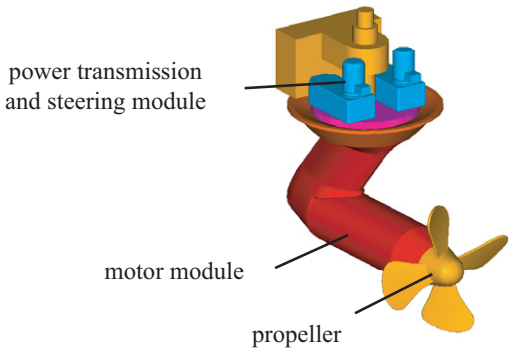

Figure 2.3: ABB's Azipod [3].

2.2.3 Elevators

Different solutions exist to lift an elevator cabin depending on the building size and architecture. Traditionally, induction machines have been used together with an hydraulic system or a gear. Another solution for large elevators is to utilize direct-drive DC or induction machines [18].

Elevators driven by gearless PM machines have recently gained popularity for medium-sized buildings, i.e., buildings with less than 20 floors. In addition to the common advantages of a direct drive such as an oil free system, less noise, and a higher drive efficiency, the gearless elevators do not need any machine room. Therefore, space is saved in the building. However, the drive is not exactly direct since cables or belts are used to move the cabin.

A typical passenger elevator for medium-sized buildings carries loads from 500 kg to 2500 kg at a speed of approximately 1 m/s. 5 to 20 kW motors are required with a shaft speed lower than 300 rpm. Larger elevators can require motor ratings of up to 500 kW.

All of the four largest elevator manufacturers[1] propose gearless elevators using PM machines. Otis with its Gen2^{TM} proposes a RFPM motor driving the elevator with a system of belts that replace the conventional steel cables. Kone adopted the solution of a flat AFPM machine (Figure 2.4.a). As can be seen in Figure 2.4.b, the AFPM machine can be placed inside the space needed for the counterweight, between the elevator's cabin and the wall [19]. Another similar solution with details on the design of a slotless AFPM machine is described in [20].

Solutions with linear motors are being investigated for lifting elevators of large buildings, such as in [21] with linear switched reluctance motors.

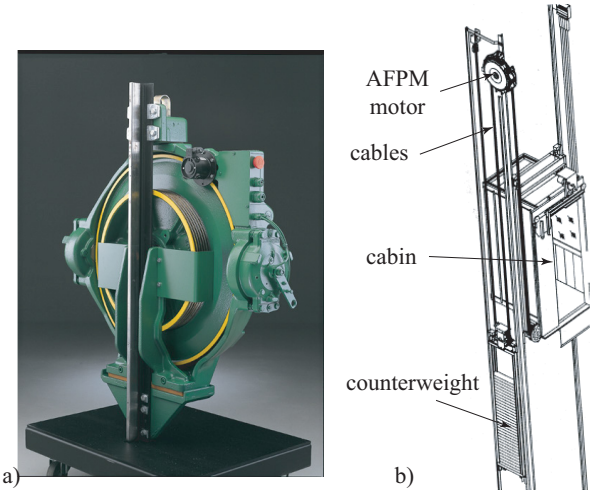

Figure 2.4: a) KONE EcoDisc® AFPM machine [22]; b) Kone MonoSpace^{TM}elevator [19].

[1]The four largest elevator manufacturers are Otis, ThyssenKrupp, Schindler Group, and Kone.

2.2.4 Washing machines

In a conventional washing machine, a DC or an induction motor drives the drum via a belt and pulleys (Figure 2.5.a). The main advantage of a direct-drive washing machine (Figure 2.5.b) comes from the suppression of the belt, pulley and eventual brushes of the DC motor. Indeed, these elements are the weak parts of the washing machine and are often the cause of failures.

A washing-machine motor for home appliance rates usually less than one kilowatt. The drum of the machine rotates approximately at 50 rpm during the washing process, up to approximately 1500 rpm or higher during the drain [23]. Therefore, the direct-drive motor of the washing machine should run over a large speed range which is achieved by operating under field-weakening.

LG produces the most famous commercialized direct-drive washing machine for home appliances. The motor, directly-connected to the drum, is a brushless DC (BLDC) PM motor (Figure 2.5.b). BLDC PM motors have trapezoidal back-EMF waveforms and are supplied with rectangular currents.

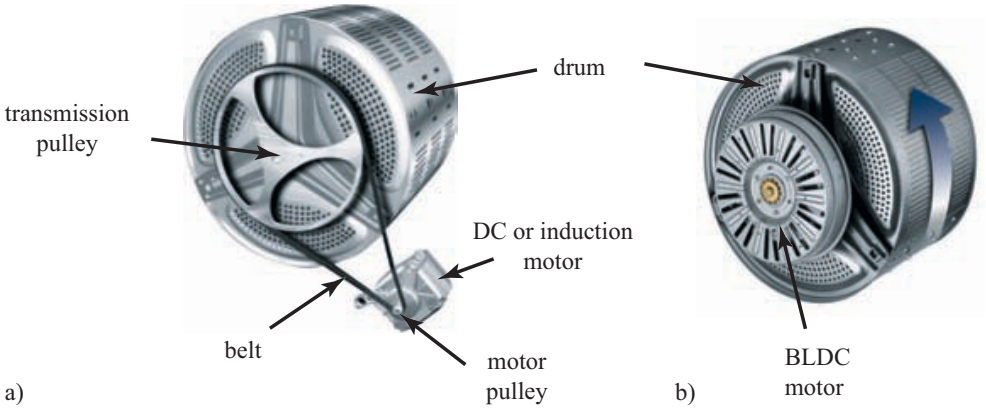

Figure 2.5: a) Conventional washing machine; b) LG's direct-drive washing machine [24].

2.2.5 Pulp and paper industry

Low-speed drives with gearboxes are widely used in the pulp and paper industry. However, a direct drive without gearbox allows, among other advantages, a gain of space and an easier installation.

Paper machines have rotational speeds between 200 and 600 rpm. Motor powers range from 30 kW to 1800 kW [25]. Direct drives with induction motors can compete with geared drives in some cases [26]. PMSM are also successfully used in direct drives for pulp and paper applications [3, 25]. These machines are RFPM motors with usually 12 poles [3]. Different designs of RFPM machines with non-overlapping concentrated windings are investigated in [27] and a 45 kW, 600 rpm prototype motor with V-shaped buried PMs has been built.

2.2.6 Others

Direct drives are also becoming more common in applications requiring precise speed and position controls. Such applications include machine tools, turning tables, radar, telescopes, etc. The motors used in these applications are the so-called torque motors which are brushless DC servomotors with (usually) surface-mounted PMs on the rotor. The torque motor can have sizes from 100 mm to more than 2 m [28]. In order to provide large torques, the torque motors have a large airgap diameter and, therefore, they look like a ring.

2.2.7 Waste-water treatment plant mixer

During the process of cleaning waste-water, mixers are used in large pools in order to keep the fluid in movement. Figure 2.6.a shows a pool emptied from the waste-water and four installed mixers. The present commercialized mixers from ITT Water & Wastewater[2] are driven by an induction motor coupled to a gearbox (Figure 2.6.b).

The advantages with using a direct-drive mixer include an increased efficiency and the introduction of speed control which gives the user a higher flexibility.

Low-speed waste-water mixers have rated powers of a few kilowatts. Their propeller rotates usually at a constant low speed (around 50 rpm) [29].

[2]World leader of submersible pumps, mixers and accessories, previously called ITT Flygt.

Two solutions for a direct-drive mixer have been investigated in the case of ITT Water & Wastewater's "banana-blade" mixer (Figure 2.6.b). The first solution consists in using hydraulic pumps [30]. This solution is not satisfactory as both initial and operating costs of the hydraulic direct-drive mixer are higher than the geared mixer.

The other solution is to use a PMSM that drives the mixer directly. This solution has been investigated by the author of this thesis. First, various PM motor designs have been compared ([VI], [VII], Chapter 4). Then, a motor with non-overlapping concentrated windings, buried PMs, and 56 poles has been chosen as the most suitable motor for the application. In [31], J. Hallberg proposed a mechanical design and investigated economical aspects for this motor. Hallberg showed that the total weight of the motor with its non-active components such as seals, bearings, and shaft, exceeded the requirements by almost 50 %. Furthermore, the cost of the new solution also exceeded the cost of the existing mixer by approximately 50 %. However, the direct-drive mixer most likely had a higher efficiency and, thus, a lower operating cost. Improvements on the manufacturing as well as the optimization of the non-active parts could help decrease the additional cost and weight. Chapter 4 describes further the design and manufacturing issues concerning the direct-drive mixer.

a)

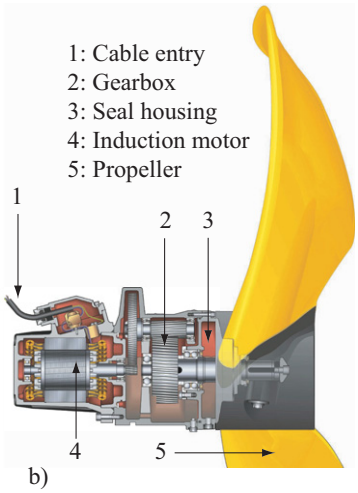

b)

Figure 2.6: a) Waste-water treatment plant pool with four mixers; b) ITT Water & Wastewater's banana blade mixer [29].

2.3 Low-speed direct-drive PM machines

2.3.1 Number of poles

The fundamental frequency f of the power-electronic converter is given by the required speed of the synchronous motor (n in rpm) and its number of poles p:

$$n = \frac{120f}{p}. \tag{2.1}$$

Machines with a low number of poles, designed for a higher rated speed, can be operated at low speeds if the supplied frequency is low, as long as the mechanical structure and shaft of the machine can cope with the higher torque. However, this solution is not efficient since the supplied frequency gets much lower than the rated frequency range of the converter. With a low frequency, the transistors have to be over-dimensioned in order to withstand the larger thermal variations [32]. Therefore, machines with a high number of poles are generally preferable, the supplied synchronous frequency being around 50 Hz.

2.3.2 Machine topology

With induction machines, the power factor drops with higher pole numbers due to an increased leakage inductance [26]. Therefore, induction machines are not really suitable for low-speed direct-drives. On the contrary, the power factor of PM machines is not affected in the same manner by their number of poles. With their high torque density, PM machines are, therefore, usually considered for low-speed direct drives.

As seen in the previous examples, RFPM, AFPM and TFPM machines are all suitable for low-speed direct drives. Appendix A describes several characteristics of these machines. The focus in this thesis is on RFPM machines and the main reason is that AFPM and TFPM are complex to manufacture and the weight of the non-active magnetic material is large and difficult to estimate [33]. However, an AFPM machine for a mixer application has been investigated by the author and is reported in [VI].

2.3.3 Active weight and iron losses

PM machines with a high number of poles can feature a low active weight[3]. Indeed, for the same required nominal torque, motors with a high number of poles have a lighter magnetic circuit than motors with few poles, as illustrated in Figure 2.7. Both machines in this figure have a maximum open-circuit airgap flux density of approximately 0.75 T. The flux density is identical but the flux from one pole to the other is inversely proportional to the number of poles. Since the flux is lower with a higher number of poles, the stator and rotor yokes can be made thinner without any higher risk of saturating the iron.

The relationship given in (2.1) shows that when the motor speed is low, the number of poles can be increased while keeping a relatively low frequency. Therefore, the iron losses for these low-speed applications are usually relatively low compared to the copper losses. Figure 2.8 shows the active weight and iron losses of PMSMs with different pole numbers designed for the mixer application requiring 50 rpm and 4.5 kW. All the designs have the same amount of copper losses. As can be seen, the active weight decreases with an increasing pole number. Since the volume of iron also decreases, the increase of the iron losses is limited when the frequency increases with the pole numbers. The dashed line shows how the iron losses change if the weight of the machines is kept constant. The iron losses increase more significantly due to the dependency on the frequency, since the frequency increases with the increasing pole number. The iron losses are calculated from a simple model: the losses are decomposed into the hysteresis and eddy current losses calculated in the teeth and stator yoke respectively. Only the values of the maximum open-circuit are used.

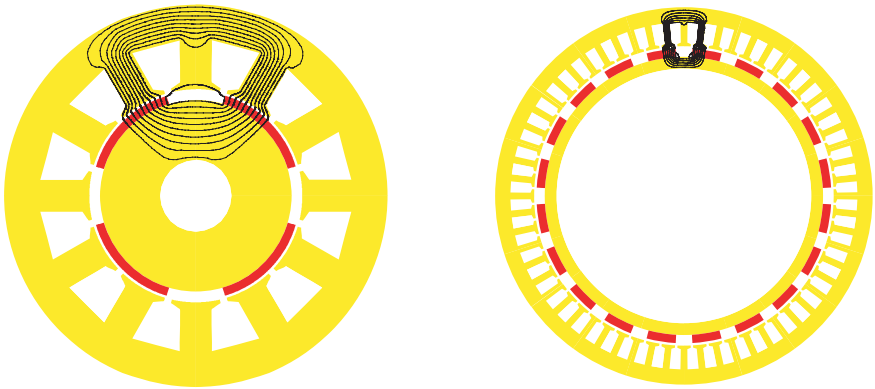

Figure 2.7: a) 4-pole PM machine; b) 20-pole PM machine.

[3]The active weight is defined in this thesis as the weight of the motor's parts that participate to the torque production, i.e. the stator and rotor iron, the PMs and the windings copper.

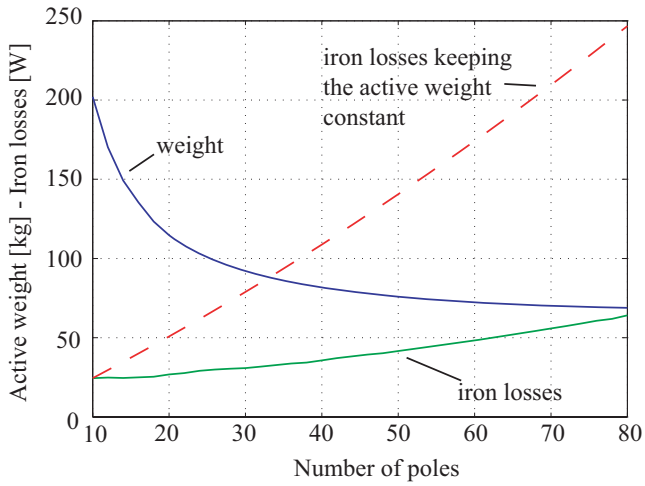

Figure 2.8: Active weight and iron losses as a function of the pole number for different PMSM designs.

2.3.4 Winding type

The higher the number of poles of the machine, the higher the number of slots, as can be seen in Figure 2.7.b. However, the space for the slots is limited, since the pole pitch is small. Therefore, with high pole numbers it is usually not possible to have a number of slots per pole per phase q higher than 1. The higher q, the more sinusoidal the magneto-motive force (MMF) and thus the lower the torque ripple and losses.

Non-overlapping concentrated windings are particularly suitable for low-speed direct drives since in these machines, the number of slots Q_s is close to the number of poles ($Q_s \approx p$) and, thus, $q = \frac{Q_s}{3p} \approx \frac{1}{3} < 1$ for 3-phase machines. Therefore, the space available for the slots is not an issue.

2.4 Summary

Low-speed direct-drives with PM machines are used in a large variety of applications, from a few kilowatts in washing machines or elevators to several megawatts in boats or wind turbines. The different applications reviewed in this chapter are placed in a power versus rated speed diagram in Figure 2.9.

The application of the mixer for waste-water treatment is presented. This geared application with the potential to be a direct drive is further investigated in Chapter 4.

Low-speed direct-drive PM machines features a high number of poles and thin stator and rotor yokes implying a low active weight. Non-overlapping concentrated windings are especially suitable for these applications and are, therefore, the subject of the next chapter.

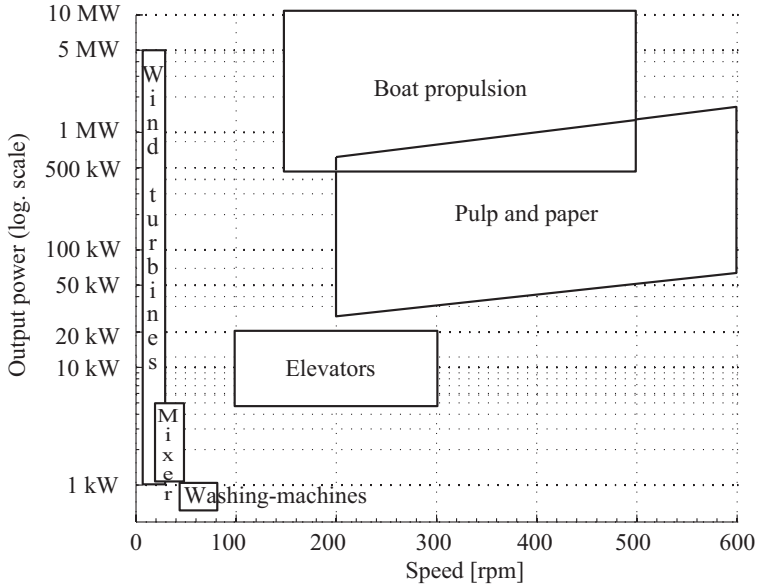

Figure 2.9: Power versus speed diagram for different low-speed direct-drive applications.

3 Design of PMSMs with non-overlapping concentrated windings

PMSMs with non-overlapping concentrated windings have become a competitive alternative to PMSMs with distributed windings for certain applications. Non-overlapping concentrated windings are indeed attractive for several reasons. Besides the short end-windings, a low cogging torque, good fault-tolerant capability, and a high constant power speed range can be achieved. Therefore, PMSMs with non-overlapping concentrated windings have recently been widely investigated.

The design of such PMSMs differs from the design of PMSMs with distributed windings. The goal of this chapter is to underline the particular design features of 3-phase PMSMs with concentrated windings. No analytical model is presented but relevant references are provided. Especially, the influence on the design of the combination of pole and slot numbers is investigated. Some examples and short studies based on FE simulations of PMSMs with concentrated windings illustrate some of the choices that have to be made during the design process.

3.1 Terminology

3.1.1 Non-overlapping concentrated windings

As mentioned in [34] and [35], many different terms can be found in the literature to refer to windings having non-overlapping coils with $q < 1$. These terms include: "concentrated windings" [36–39], "non-overlapping concentrated winding" [35], "tooth concentrated windings" [34], "tooth concentrated fractional windings" [40], "concentrated coil" [41], "fractional slot wound" [42], "fractional-slot with non-overlapped coils" [43], "fractional-slot pitch concentrated windings" [44].

A few comments can be made about these terms. The term "concentrated windings" has recently been employed to refer to the windings that are concentrated around the teeth, i.e. non-overlapping. However, "concentrated windings" refers traditionally to windings having one slot per pole per phase [34]. Therefore, in order to avoid any confusion, the term "concentrated windings" should be associated to "non-overlapping", "fractional slot" or "tooth". The term "fractional slot winding" alone is also not sufficient to refer to non-overlapping concentrated windings as fractional slot windings could be either non-overlapping or overlapping.

In this thesis, the author uses both "non-overlapping concentrated windings" and "concentrated windings", the second option being used to make the text easier to read. However, in this thesis, "concentrated windings" refers always to non-overlapping windings. It is the opinion of the author that the term "concentrated windings" is now well-known within the electrical machines community and any confusion is not so likely to occur.

3.1.2 Modular machines

PM machines with non-overlapping concentrated windings are sometimes classified into two types: traditional brushless PM machines and modular PM machines [45, 46]. Figure 3.1 illustrates the differences between these two motor types. In traditional brushless PM machines with concentrated windings, the ratio between the slot and pole numbers is equal to 3/2. This corresponds to a number of slots per pole per phase equal to $q = 0.5$ in the case of a 3-phase PMSM. The phases of the windings are alternated for each consecutive tooth and the coil span is 120° elec. This results in a relatively low "fundamental" winding factor equal to 0.867. Modular PM machines have a number of slot per pole per phase which is strictly lower than 0.5 and strictly higher than 0.25. As shown in Figure 3.1, two consecutive teeth or more are wound with the same phase. This results in a high "fundamental" winding factor, low torque ripple but also possible vibration and noise issues and high rotor losses.

Modular PM machines have an MMF distribution with fewer poles than rotor poles as illustrated in Figure 3.2 for a 28-pole, 24-slot modular PMSM. Thus, the MMF harmonic component that interacts in the mean torque production is not the fundamental but a higher harmonic component of the same order as the number of pole pairs $p/2$ [47]. It is then called *main harmonic component* in [47] or *synchronous frequency component* in [39]. The order of the synchronous frequency component for the 28-pole, 24-slot machine is then 28/2=14 (see also first line under the spectra in Figure 3.2). The corresponding winding factor is then called winding factor of main harmonic [47] or synchronous-component winding factor [39].

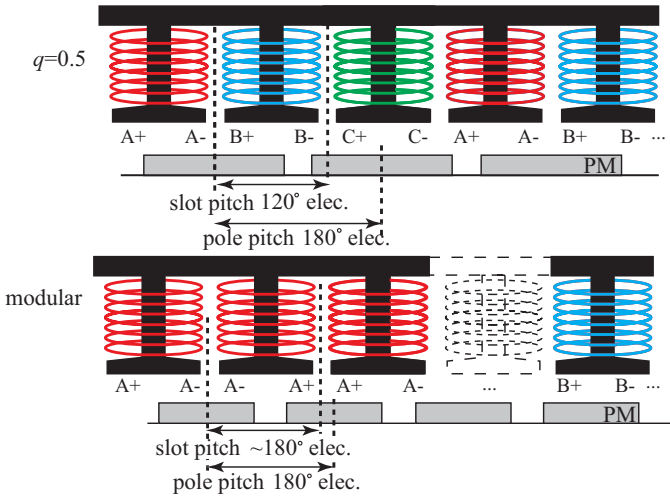

Figure 3.1: Two categories of concentrated windings of: a) Traditional brushless PM machines ($q = 0.5$); b) Modular PM machines ($0.25 < q < 0.5$).

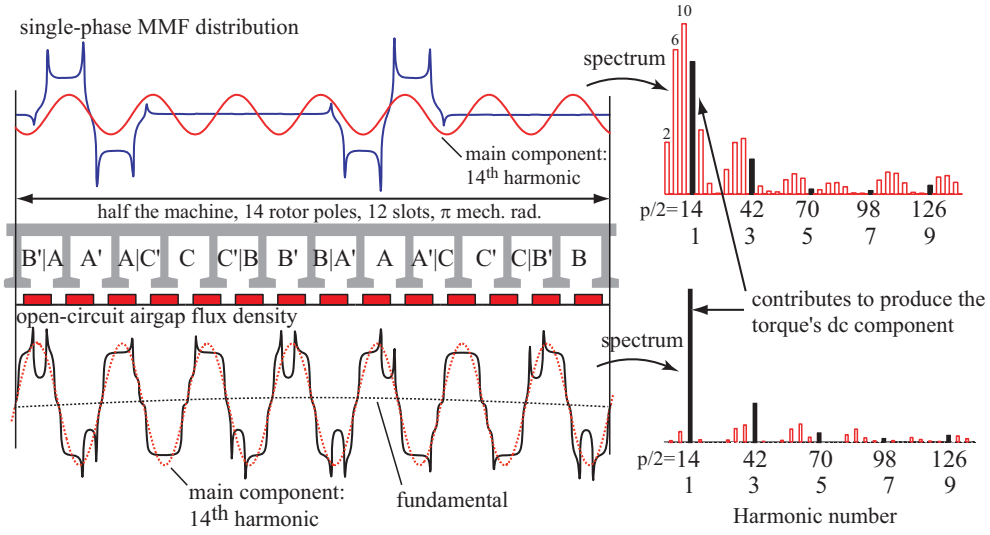

Figure 3.2: MMF distribution and open-circuit airgap flux density and their spectrum for a 28-pole, 24-slot PM motor.

Another possible description of the winding is to define the main harmonic component as the fundamental, considering the electrical angle instead of mechanical angle as previously done. This description considering electrical angle has been used in

e.g. [37]. The relation between the two sets of harmonic orders is shown under the spectra of Figure 3.2 for the 28-pole, 24-slot machine. This implies that all the sub-harmonics of "mechanical" order lower than $p/2$ have, when considering "electrical", orders with fractional values lower than 1.

The harmonic components in the MMF with fractional orders (or with orders other than $kp/2$, k being an integer if considering mechanical angles) do not play any role in the analytical calculations of the back-EMF and the mean value of the torque, if the slot effects are not taken into account. It is then convenient to have the "synchronous-component" winding factor equal to the component of order 1, disregarding the harmonics of fractional orders. Interestingly, if all the harmonics of fractional values are removed from the true MMF, the reduced MMF is corresponding to the distribution of a PMSM with distributed windings. This is illustrated for the 28-pole, 24-slot PMSM in Figure 3.3. If rotor loss or vibrations are to be investigated, the complete spectrum of the MMF has to be considered. It is then not practical to deal with fractional orders of harmonics and mechanical angles are preferable.

In the present thesis, the term fundamental winding factor is used to refer to the winding factor used in the mean torque calculation. In the section about the rotor losses (Section 3.2.3.4), mechanical angles are used and the term synchronous-component winding factor is exceptionally employed in order to avoid fractional orders of the harmonics.

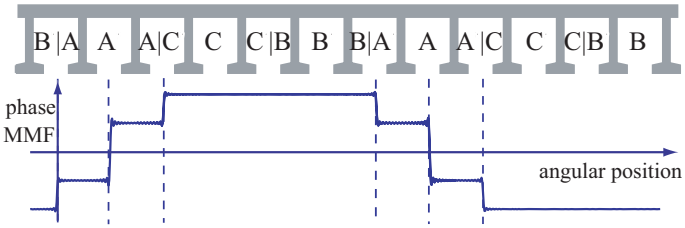

Figure 3.3: Single phase MMF distribution for a 28-pole, 24-slot PM motor when only considering the harmonics of integral (or $kp/2$) orders.

3.2 Design of PMSMs with non-overlapping concentrated windings

3.2.1 Manufacturing

The method to manufacture the stator core and windings should be considered at an early stage of the machine's design. Indeed, the chosen method determines the tooth shape (with or without tips), the slot fill factor or the stator core material (iron or SMC) of the machine. The different manufacturing technics are presented and analyzed further in Chapter 5 of this thesis. Table 3.1 summarizes some possibilities and their influence on the slot fill factor.

Table 3.1: Methods to manufacture the stator core and windings of a PMSM with non-overlapping concentrated windings.

method	stator core production	windings	slot fill factor
laminated core	punching	needle windings	low (≤ 0.5)
spiral-laminated core	punching (patented)		low (≤ 0.5)
joint-lapped core	punching (patented)		high
single-tooth segments	punching + welding	pre-wound windings	high (≥ 0.6)
SMC	press		
open slots	punching		

3.2.2 Selection of the number of layers

After reflecting on the manufacturing methods, the number of layers of the windings should be chosen. Single-layer windings have coils wound only on alternate teeth, whereas each tooth of the double-layer windings carries a coil. This is illustrated in Figure 3.4.

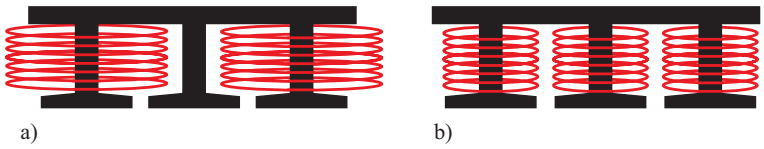

Figure 3.4: Three teeth and the coils: a) From a single-layer winding; b) From a double-layer winding.

The choice of the number of layers depends mostly on the application. Table 3.2 compares some characteristics of single-layer and double-layer concentrated windings. Ishak discussed fully these differences for the winding factor, EMF and inductances in [48] and for the losses in [49]. In [47], Bianchi defines rules to transform a double-layer to a single-layer winding and discusses the advantages of concentrated windings for fault tolerance.

Table 3.2: Comparison between single and double-layer concentrated windings.

	Single-layer	Double-layer
Fundamental winding factor	higher	lower
End-windings	longer	shorter
Slot fill factor	higher	lower
Self-inductances	higher	lower
Mutual-inductance	lower	higher
EMF	more trapezoidal	more sinusoidal
Harmonic content of MMF	higher	lower
Eddy current losses in the PM	higher	lower
Overload torque capability	higher	lower

Single-layer windings are preferred to double-layers windings when a high fault-tolerance is required since the phases of the windings are thermally and electrically isolated, the self-inductance is high (which limits the short circuit currents), and the mutual inductance is very low (which isolate the phases magnetically). Due to their higher inductance, single-layer windings are also preferred in applications requiring a wide speed range of constant power operation. Otherwise, double-layer windings are preferable to limit the losses and torque ripple. Furthermore, there are more possible combinations of pole and slot numbers to choose between with double-layer windings than with single-layer windings. Single-layer windings with unequal tooth widths are interesting for brushless DC operation [50]. The teeth that are not carrying any coils are thinner than the other teeth. The winding flux-linkage and the fundamental winding factor are then increased, which gives a more trapezoidal phase back-EMF [50].

3.2.3 Selection of number of poles and number of slots

The next step after selecting the number of layers is to determine the number of poles and the number of slots. The nominal speed or frequency gives a range of possible pole numbers. Then, the pole number should be selected in combination with the number of slots. This selection is done by looking at the winding factor, the cogging and torque ripple, the vibration, rotor losses and inductance of the machine associated with the specific combination.

3.2.3.1 Winding layout and winding factor

Theory

The winding layout and winding factor of a PMSM with concentrated windings depends on its combination of pole and slot numbers. Therefore, this combination should be carefully chosen in order to maximize the fundamental[1] winding factor and thus the torque.

For a given combination of pole and slot numbers, there are many possibilities to arrange the coils of each phase in the slots to form the winding layout. The most interesting winding layout is the one that gives the highest fundamental winding factor. There are different methods to find the winding layout. One method is similar to the one used for the synchronous machine with fractional slot windings [36], while another method is based on the star of slots [51]. These methods are described in appendix B. The first method is easy to apply for finding the layouts of double-layer concentrated-windings, but it is, in some cases, difficult to find the layouts for the single-layer windings. However, the method provided in [51] allows to find the layout of the single-layer windings from the double-layer windings layout in all possible cases.

The winding factor can be calculated by following different methods: using the EMF phasors [37, 47], [VIII], using the winding function [39] or using closed-form expressions [45, 52]. The relation between the combination of pole and slot numbers and the winding factor has been investigated by the author using the method based on the EMF phasors.

The winding layout can be found using one of the method described in appendix B. The vector S describes the layout of phase A. The slots are numbered from 1 to Q_s. The vector S consists of the numbers corresponding to the slots that contain conductors of phase A. If both layers of one slot contain conductors of phase A, the number of the slot is written twice in the vector. S has thus $2Q_s/3$ elements. For conductors A', a minus is added to the corresponding slot number. For example, the winding layout of a PMSM with $Q_s = 24$ and $p = 28$ and its vector S are shown in Figure 3.5 and equation (3.1).

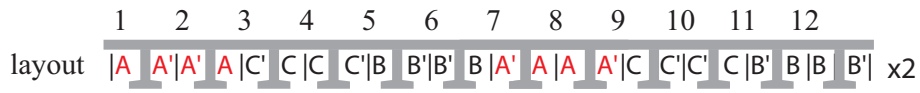

Figure 3.5: Winding layout of a 28-pole, 24-slot PMSM.

$$S = [\ 1 \quad -2 \quad -2 \quad 3 \quad -7 \quad 8 \quad 8 \quad -9 \quad 13 \quad -14 \quad -14 \quad 15 \quad -19 \quad 20 \quad 20 \quad -21\ ] \tag{3.1}$$

[1] See Section 3.1.2.

Using vector S, the corresponding EMF phasor $\overrightarrow{E_i}$ of a coil side i from phase A for the fundamental (or main harmonic of order $p/2$) is:

$$\overrightarrow{E_i} = \text{sign}(S(i))e^{j\frac{\pi p}{Q_s}|S(i)|}. \tag{3.2}$$

The fundamental winding factor k_{w1} can then be calculated as

$$k_{w1} = \frac{1}{n_l Q_s/3}\left|\sum_{i=1}^{n_l Q_s/3}\overrightarrow{E_i}\right| \tag{3.3}$$

where i is an element of S and n_l is the number of layers ($n_l = 2$).

The sum of the EMF phasors for the example of a 28-pole, 24-slot PMSM is then given in equation (3.4) and Figure 3.6.

$$\begin{aligned}\sum_{i=1}^{2\times 24/3=16}\overrightarrow{E_i} = e^{j\frac{\pi p}{Q_s}}(1 - 2e^{j\frac{\pi p}{Q_s}} + e^{2j\frac{\pi p}{Q_s}} - e^{6j\frac{\pi p}{Q_s}} + 2e^{7j\frac{\pi p}{Q_s}} - e^{8j\frac{\pi p}{Q_s}} \\ + e^{12j\frac{\pi p}{Q_s}} - 2e^{13j\frac{\pi p}{Q_s}} + e^{14j\frac{\pi p}{Q_s}} - e^{18j\frac{\pi p}{Q_s}} + 2e^{19j\frac{\pi p}{Q_s}} - e^{20j\frac{\pi p}{Q_s}})\end{aligned} \tag{3.4}$$

This results in a fundamental winding factor of $k_{w1} = 0.933$.

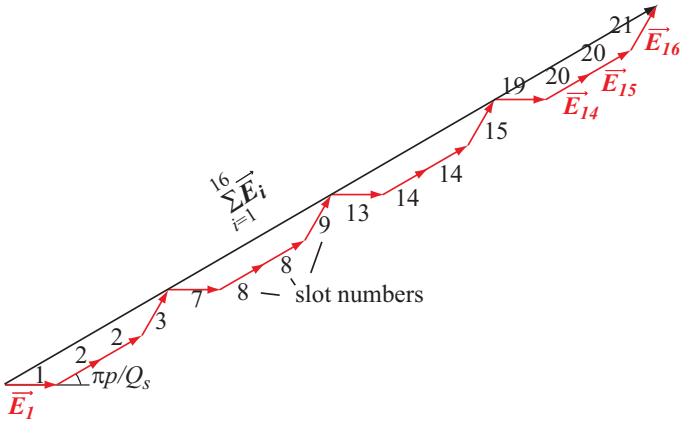

Figure 3.6: Sum of EMF phasors for one phase of a 28-pole, 24-slot PMSM.

The fundamental winding factors for different combinations of pole and slot numbers are given in Table 3.3 for double-layer windings up to 40 poles[2] and in Table 3.4 for the single-layer windings. The associated winding layout of some cases are reported in Table 3.5. The method used to construct these tables is described below as well as the trends of the fundamental winding factor versus combinations of pole and slot numbers.

[2]Values of fundamental winding factors for up to 80 poles can be found in [VI].

Table 3.3: Fundamental winding factors for different combinations of pole and slot numbers and double-layer windings.

Q_s\p	4	6	8	10	12	14	16	18	20	22	24	26	28	30	32	34	36	38	40
6	0.866		0.866	0.5		0.5	0.866		0.866	0.5		0.5	0.866		0.866	0.5		0.5	0.866
9	0.617	0.866	0.945	0.945	0.866	0.617	0.328		0.328	0.617	0.866	0.945	0.945	0.866	0.617	0.328		0.328	0.617
12	q=1		0.866	0.933		0.933	0.866								0.866	0.933		0.933	0.866
15			0.621	0.866		0.951	0.951		0.866	0.621								0.621	0.866
18		q=1		0.647	0.866	0.902	0.945		0.945	0.902	0.866	0.647							
21						0.866	0.89		0.953	0.953		0.89	0.866						
24			q=1			0.76	0.866		0.933	0.95		0.95	0.933		0.866	0.76			
27								0.866	0.877	0.915	0.945	0.954	0.954	0.945	0.915	0.877	0.866		
30				q=1					0.866	0.874		0.936	0.951		0.951	0.936		0.874	0.866
33										0.866		0.903	0.928		0.954	0.954		0.928	0.903
36					q=1						0.866	0.867	0.902	0.933	0.945	0.953		0.953	0.945
39												0.866	0.863		0.918	0.936		0.954	0.954
42						q=1							0.866		0.89	0.913		0.945	0.953
45														0.866	0.859	0.886		0.927	0.945
48							q=1								0.866	0.857		0.905	0.933
51																0.866		0.88	0.901
54								q=1									0.866	0.854	0.877
57																		0.866	0.852
60									q=1										0.866

	q=1/2, 1/4	q=3/8, 3/10	Q_s=21+6k, p=Q_s±1, k = 0, 1, 2 ...
	q=3/7, 3/11	q=5/14, 5/16	Q_s=24+6k, p=Q_s±2, k = 0, 1, 2 ...
	q=2/5, 2/7	not appropriate	k_{w1}<0.866

Table 3.4: Fundamental winding factors for different combinations of pole and slot numbers and single-layer windings.

Qslp	4	6	8	10	12	14	16	18	20	22	24	26	28	30
6	0.866		0.866	0.5										
12	0.5		0.866	0.966		0.966	0.866		0.5					0.5
18		0.5			0.866	0.902	0.945		0.945	0.902				
24			0.5				0.866		0.966	0.958		0.958	0.966	
30				0.5					0.866	0.874		0.936	0.951	

Table 3.5: Winding layouts for some combinations of pole and slot numbers.

Q_s, p or q	Winding layout
$q = 2/5,\ 2/7$	$\ldots\|C'A\|A'A'\|AB'\|BB\|B'C\|C'C''\|CA'\|AA\|A'B\|B'B'\|BC''\|CC\|\ldots$
$q = 3/8,\ 3/10$	$\ldots\|C'A\|A'A'\|AA\|A'B\|B'B'\|BB\|B'C\|C'C''\|CC'\|\ldots$
$q = 3/7,\ 3/11$	$\ldots\|C'A'\|AB'\|BB\|B'C''\|CA\|A'A'\|AB'\|BC''\|CC\|C'A\|A'B\|B'B'\|BC'\|CA'\|AA\|A'B\|B'C\|C'C''\|\ldots$
$q = 5/14,\ 5/16$	$\ldots\|C'A\|A'A'\|AA\|A'A'\|AA\|A'B\|B'B'\|BB\|B'B'\|BB\|B'C'\|C'C''\|CC\|C'C''\|CC\|\ldots$
$Q_s = 12 + 6k$, $p = Q_s \pm 2$ if $p/2$ even	$\ldots \underbrace{A\|A'A'\|A\ldots A\|A'A'\|A}_{Q_s/6}\underbrace{B'\|BB\|B'\ldots B'\|BB\|B'C}_{Q_s/6}\underbrace{\|C'C'\|C\ldots C\|C'C'\|C}_{Q_s/6}\ldots$
	$\underbrace{A\|A'A'\|A\ldots A'\|AA\|A'B'}_{Q_s/6}\underbrace{\|BB\|B'\ldots B\|B'B'\|B}_{Q_s/6}\underbrace{C\|C'C'\|C\ldots C'\|CC\|C'A'}_{Q_s/6}\underbrace{\|\ldots\|A\,B\|\ldots\|B'\,C'\ldots C}_{Q_s/6}$
$Q_s = 9 + 6k$, $p = Q_s \pm 1$	$\underbrace{A\|A'A'\|A\ldots A'\|AA\|A'B\|B'B'\|B\ldots B'\|BB\|B'C\|C'C'\|C\ldots C'\|CC\|C'}_{Q_s/3}\underbrace{\qquad\qquad}_{Q_s/3}\underbrace{\qquad\qquad}_{Q_s/3}$

Some combinations of pole and slot numbers do not give a balanced three-phase winding. It is the combinations where the denominator d of q is a multiple of the number of phases ($q = \frac{Q_s}{3p} = \frac{n_u}{d}$, with $d = \frac{3p}{\mathrm{GCD}(Q_s,3p)}$ and n_u numerator or q). GCD(Q_s,3p) is the greatest common divisor between the number of slots Q_s and three times the number of poles. These combinations are colored in red and black (dark cases without numbers) in Table 3.3 and Table 3.4.

Combinations with the same number of slots per pole per phase q have equal winding factors. Their winding layouts consist of the same basic sequence reproduced $X = \mathrm{GCD}(p/2,Q_s)$ times to fill the required number of slots (see Table 3.5). X can be called the machine periodicity [51] or the number of symmetries of the winding layout [VIII]. For example, the combination with 10-pole, 12-slot and single-layer winding has a fundamental winding factor of 0.966 with a layout $|A|A'|B'|B|C|C'|A'|A|B|B'|C'|C|$ and $q = 2/5$. Multiplying the number of slots and number of poles by any integer do not change the number of slot per pole per phase. Therefore, combinations with 20-pole, 24-slot, 30-pole, 36-slot and so on, have the same fundamental winding factor 0.966 and same basic sequence of winding layout repeated twice, three times, and so on, respectively.

For each value of Q_s (i.e. each line of Table 3.3) there is a periodicity of $2Q_s$: The winding layout and factors of the combinations of pole and slot numbers with Q_s slots and $p + 2kQ_s$ poles (k=0,1,2...) are identical. This is easily shown with equations (3.3) and (3.5) since $|S(i)|$ is an integer:

$$\forall i: \; e^{j\frac{p\pi}{Q_s}|S(i)|} = e^{j\frac{p\pi}{Q_s}|S(i)|}\underbrace{e^{j2\pi|S(i)|}}_{=1} = e^{j\frac{\pi(p+2Q_s)}{Q_s}|S(i)|}. \tag{3.5}$$

For machines with Q_s slots and $p+2kQ_s$ poles (and a low $q < 0.25$), the flux leakage between the PMs is high which decreases the fundamental torque component. Furthermore, they have high subharmonic components which may cause large amount of losses in the rotor. An example of a machine with 76-pole, 24-slot is illustrated in Figure 3.7.a. This machine has the same stator, winding layout and fundamental winding factor of 0.933 as the machine having 28-pole, 24-slot shown in Figure 3.7.b. As can be seen, the number of flux lines crossing the airgap and going around the slot is much lower for the machine with 76 poles. A FE-simulation at load conditions with the same current loading for both machines shows a decrease in the torque of approximately 40 %. The number of possible applications for machines with such low q is limited but they could be used in the case of magnetic gear applications. A machine with a very low speed and an integrated magnet gear is investigated in [53].

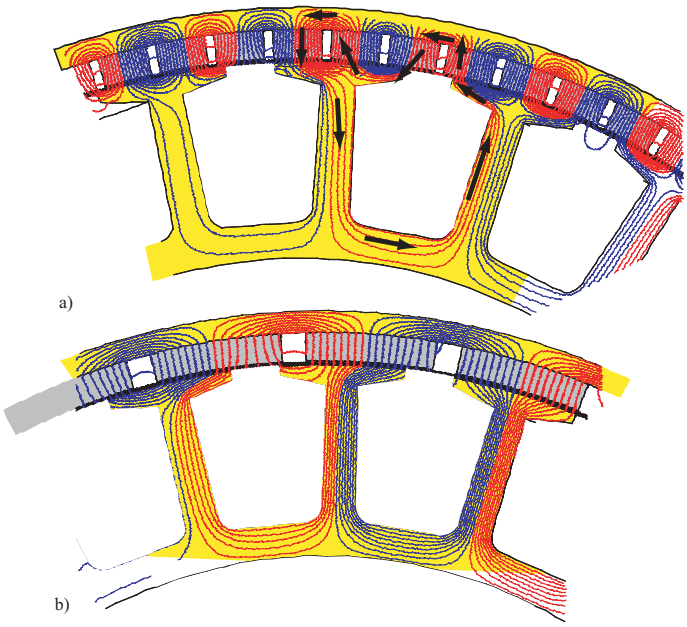

Figure 3.7: Flux lines at open-circuit: a) For a 76-pole, 24-slot PMSM; b) For a 28-pole, 24-slot PMSM (same stator).

For each Q_s (i.e. each line of Table 3.3) there is a symmetry around kQ_s (k =1, 2, 3...). This means that combinations of pole and slot numbers with $p = Q_s \pm k$ have an identical winding layout and factor. This is proved below:

$$\left|\sum_i e^{j\frac{p\,\pi\,|S(i)|}{Q_s}}\right| = \left|\sum_i \cos\frac{p\,\pi\,|S(i)|}{Q_s} + j\sum_i \sin\frac{p\,\pi\,|S(i)|}{Q_s}\right|$$
$$= \left[\left(\sum_i \cos\frac{p\,\pi\,|S(i)|}{Q_s}\right)^2 + \left(\sum_i \sin\frac{p\,\pi\,|S(i)|}{Q_s}\right)^2\right]^{1/2}$$

For $p = Q_s - k$, the sum of cosinus and sinus terms can be rewritten as:

$$\sum_i \cos\frac{\pi(Q_s-k)\,|S(i)|}{Q_s} = \sum_i \left(\cos(\pi\,|S(i)|)\cos\frac{\pi k\,|S(i)|}{Q_s} + \underbrace{\sin(\pi\,|S(i)|)}_{=0}\sin\frac{\pi k\,|S(i)|}{Q_s}\right)$$
$$= \sum_i \cos\frac{\pi(Q_s+k)\,|S(i)|}{Q_s}$$

$$\sum_i \sin\frac{\pi(Q_s-k)\,|S(i)|}{Q_s} = \sum_i \left(\underbrace{\sin(\pi\,|S(i)|)}_{=0} \cos\frac{\pi k\,|S(i)|}{Q_s} - \sin\frac{\pi k\,|S(i)|}{Q_s} \cos(\pi\,|S(i)|) \right)$$
$$= -\sum_i \sin\frac{\pi(Q_s+k)\,|S(i)|}{Q_s}$$

This leads to

$$\left| \sum_i e^{j\frac{\pi(Q_s-k)}{Q_s}|S(i)|} \right| = \left| \sum_i e^{j\frac{\pi(Q_s+k)}{Q_s}|S(i)|} \right| \tag{3.6}$$

which means that the winding factors for $p = Q_s \pm k$ are identical.

Influence of the combinations of pole and slot numbers

For the double-layer windings, the fundamental winding factor increases and decreases as shown in Figure 3.8 and Figure 3.9. The highest fundamental winding factors are found when the number of slots is closest to the number of poles ($k_{w1} \approx 0.955$, $q \approx 1/3$). In this case, the flux-linkage is maximized since the slot pitch is almost equal to the pole pitch. Figure 3.8 also shows the symmetry described above. The fundamental winding factor is as well plotted in Figure 3.9 in the case of the single-layer windings. In many cases, the winding factor for the single-layer windings is equal to the winding factor of the double-layer windings (crosses and dots are superposed in Figure 3.9). Around $q \approx 1/3$, the winding factors for some single-layer windings are higher than those from double-layer windings for the same value of q. The highest fundamental winding factor for the single-layer windings, $k_{w1} = 0.966$, is obtained for $q = 2/7$ or $q = 2/5$.

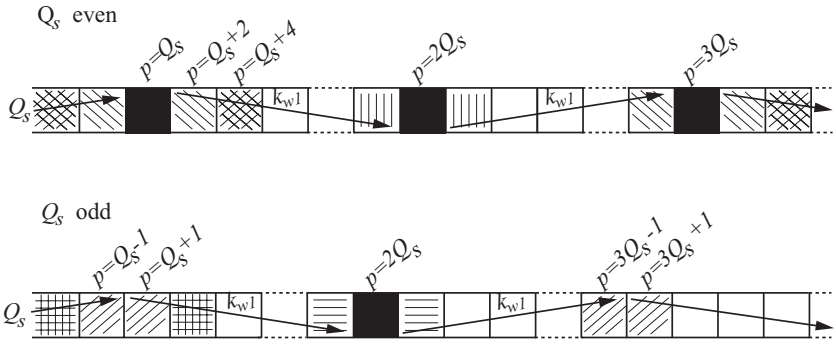

Figure 3.8: Evolution of the fundamental winding factor k_{w1} for double-layer windings. (Boxes filled with the same pattern have the same winding factor and layout. Black boxes are combinations where concentrated windings are not possible).

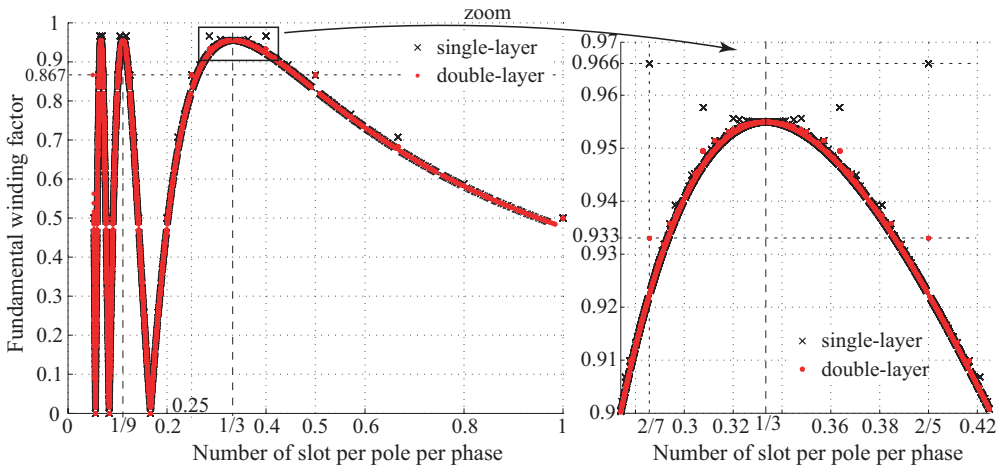

Figure 3.9: Fundamental winding factor as a function of q.

3.2.3.2 Noise and vibrations

Modular machines may be subject to high vibrations and noises depending on the combination of pole and slot numbers. The vibration and noise come mostly from the radial magnetic forces in the airgap while the tangential forces act on the rotor to produce the torque [54].

Theory

The radial magnetic force is given by Maxwell's tensor and can be computed from the normal and tangential component of the airgap flux density using:

$$\sigma(\theta,t) = \frac{1}{2\mu_0}(B_n^2(\theta,t) - B_t^2(\theta,t)) \tag{3.7}$$

where σ is the radial magnetic force density as a function of the angular coordinate θ and the time t, B_n is the normal, i.e. radial component of the airgap flux density, and B_t the tangential component. Additional theory on magnetic noise can be found in e.g. [54].

Unbalanced magnetic pull and combinations of pole and slot numbers

If the radial magnetic forces are not regularly distributed along the airgap, their sum results in an unidirectional pulling force that rotates with time and generates noise and vibration in the machine. This resulting force, called unbalanced magnetic pull, can be due to the asymmetry in the windings as illustrated in Figure 3.10.a and Figure 3.10.b. The radial magnetic forces are computed from a FE-simulation

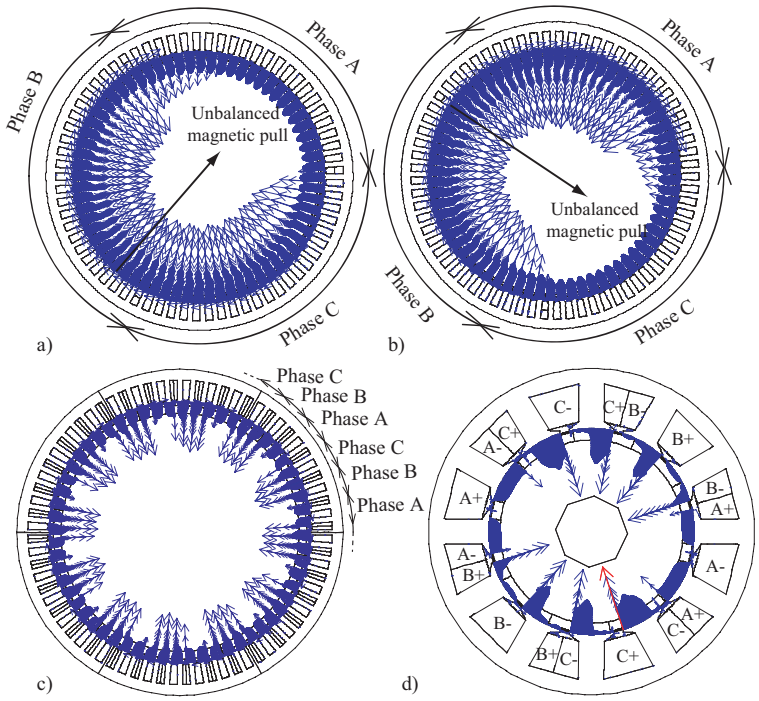

Figure 3.10: Magnetic forces on the stator of PMSMs with: a) and b) 68 poles and 69 slots, at different times; c) 60 poles, 72 slots; d) 10 poles, 12 slots.

for a motor having $p = Q_s - 1$. As can be seen, there is no symmetry in the winding layout, the slots carrying the conductors of the same phase being regrouped over one third of the machine. The unbalanced distribution of the forces is obvious. Figure 3.10.c shows an example when there is a symmetry in the winding layout in one sixth of the machine. In this case, there is no resulting force as the radial magnetic forces compensate each other.

The machines subject to an unbalanced magnetic pull are those that do not have any symmetry in their winding layout, the conductors orientation being not taken into account. For example, an 8-pole, 9-slot motor with the winding layout AAABB-BCCC is subject to an unbalanced magnetic pull. The conductors orientation has no influence on the radial magnetic forces since these forces are proportional to the square of the flux density (equation (3.7)). The number $X' = \mathrm{GCD}(p,Q_s)$ given in Table 3.6.a represents the number of symmetries in the winding layout without considering the conductor's orientation. The combinations of pole and slot numbers with $p = Q_s \pm 1$ and some combinations with an odd number of slots have $X' = \mathrm{GCD}(p,Q_s) = 1$. Thus, they are not recommended because of the unbalanced magnetic pull.

The number $X = \mathrm{GCD}(p/2,Q_s)$ is the number of rotational symmetries in the winding layout or the machine periodicity. The conductor orientation is taken into account in this case. The inverse of this number $1/X$ is the fraction of the machine that should be modelled in a FE-program. If $X = \mathrm{GCD}(p/2,Q_s) = 1$, the whole machine should be modelled, as there is no symmetry in the winding layout. This is the case for a machine with 10 poles and 12 slots, as the one represented in Figure 3.10.d. Its winding layout is $A^+A^-A^+B^-B^+B^-C^+C^-C^+$ in one half of the motor and $A^-A^+A^-B^+B^-B^+C^-C^+C^-$ in the other half. However, this machine has no problem with unbalanced magnetic forces, as the phase disposition (ABCABC) is symmetrical ($X' = \mathrm{GCD}(p,Q_s) = 2$) and the radial magnetic forces from both halves of the motor compensate each other, as can be seen in Figure 3.10.d.

Table 3.6: a) Number of symmetries in the winding layout without conductors orientation $X' = \mathrm{GCD}(p,Q_s)$; b) Number of symmetries in the winding layout with conductors orientation, $X = \mathrm{GCD}(p/2,Q_s)$.

a)

Qs\p	4	6	8	10	12	14	16	18	20	22	24	26	28	30	32	34
6	2		2													
9		3	1	1	3											
12			4	2		2	4									
15				5		1	1		5							
18					6	2	2		2	2	6					
21						7	1		1	1		1	7			
24							8		4	2		2	4		8	
27								9	1	1	3	1	1	3	1	1
30									10	2		2	2		2	2
33										11		1	1		1	1
36											12	2	4	6	4	2

b)

Qs\p	4	6	8	10	12	14	16	18	20	22	24	26	28	30	32	34
6	2		2													
9		3	1	1	3											
12			4	1		1	4									
15				5		1	1		5							
18					6	1	2		2	1	6					
21						7	1		1	1		1	7			
24							8		2	1		1	2		8	
27								9	1	1	3	1	1	3	1	1
30									10	1		1	2		2	1
33										11		1	1		1	1
36											12	1	2	3	4	1

Analytical model

Although it is easier to select a combination of pole and slot numbers that avoid the problems with the unbalanced magnetic force, machines with $p = Q_s \pm 1$ can be designed as long as the unbalanced magnetic force is taken into account. This

force should be carefully considered, especially when the machine has a high electric loading [55]. The bearings should be carefully chosen [56].

In [55], Ishak proposes an analytical model to predict the unbalanced magnetic force for these machines. He shows that the higher the phase current, the higher the unbalanced magnetic force. In [56], Hoefer measures the unbalanced magnetic force for a 2-pole, 3-slot PM machine. He shows that the unbalanced magnetic force causes a deflection of the bearings that increases with the line current and depends on the bearing stiffness. The experimental tests show that the deflection is an issue for the particular application. However, Hoefer concludes that the unbalanced magnetic forces are quite low and may not be a problem as long as the bearings are carefully chosen with a high radial stiffness.

Undesired noise can occur for modular machines that do not present any unbalanced magnetic force (with $X' = \mathrm{GCD}(p,Q_s) > 1$). In [57–59], Wang shows that modular machines may be subject to low-frequency resonant vibrations within their operational speed range. These vibrations occur only at certain speeds which may or may not be an issue depending on the application.

3.2.3.3 Torque ripple

Theory

The torque is pulsating because of [46, 60]:

- The cogging torque - It is generated by the variation of the magnetic permeance seen by the PMs due to the slotting of the stator surface, even when there is no stator excitation.
- The variation of permeance seen by the PMs due to magnetic saturation.
- Space harmonics - The interaction between the spacial harmonics in the field produced by the PMs and the harmonics in the field produced by the windings. If the machine is supplied with a sinusoidal current, the torque ripple without cogging can then be calculated from the harmonics in the back-EMF [46].
- Time harmonics - The inverter induces time harmonics in the field produced by the windings which generates a pulsating torque when interacting with the rotor field.
- Undesirable imperfections in the motor such as the eventual eccentricity of the rotor or uneven magnetization of the magnets.

Figure 3.11 defines how the cogging torque and torque ripple are calculated in this thesis.

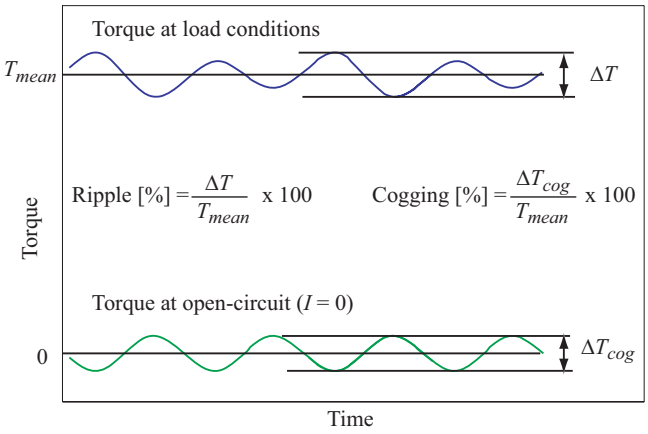

Figure 3.11: Definition of cogging and ripple torque.

Influence of the combination of pole and slot numbers

A very low cogging torque can be obtained if the slot and pole numbers are chosen so that the least common multiple (LCM) between them is large [61]. The closer the number of slots to the number of poles, the higher their LCM. Table 3.7 shows the values of LCM(p,Q_s). As can be seen, combinations of pole and slot numbers with $p = Q_s + k$ have a higher LCM(p,Q_s) than combinations with $p = Q_s - k$, though both combinations have the same winding factors. The value of LCM(p,Q_s) may then be a criteria to select the combination of pole and slot numbers.

Table 3.7: Least common multiples of the slot and pole numbers, LCM(p,Q_s).

Qs\p	4	6	8	10	12	14	16	18	20	22	24	26	28	30	32	34
6	12		24													
9		18	72	90	36											
12			24	60		84	48									
15				30		210	240		60							
18					36	126	144		180	198	72					
21						42	336		420	462		546	84			
24							48		120	264		312	168		96	
27								54	540	594	216	702	756	270	864	918
30									60	330		390	420		480	510
33										66		858	924		1056	1122
36											72	468	252	180	288	612

Furthermore, the cogging torque depends on many other parameters such as the slot opening width, magnet width, stator or magnets skewing [61]. Adjusting these parameters may reduce the cogging torque even if the combination of pole and slot numbers is not favorable. However, a low cogging torque does not always guarantee a low torque ripple.

There are several means to minimize the torque ripple of PMSMs, e.g. skewing of the stator or rotor or control-based techniques [62]. The torque ripple of PMSMs with concentrated windings is usually low (especially for modular PM machines [46]). Therefore, choosing the right combination of pole and slot numbers and adjusting some design parameters such as the PM pole arc width or the slot opening width may be sufficient to minimize the torque ripple. Figure 3.12 shows the torque ripple of PMSMs for different combinations of pole and slot numbers and relative PM widths[3] [XII]. The torque ripple is obtained from FE-simulations in which the windings are supplied with a sinusoidal current. As can be seen, there is at least one minimum in the torque ripple for each of the three combinations.

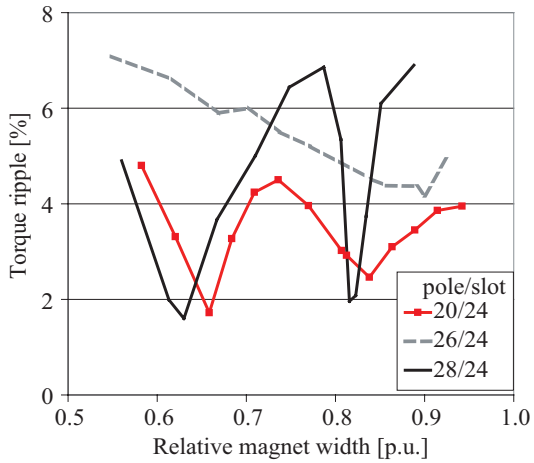

Figure 3.12: FE-simulated torque ripples as a function of the relative PM width for different combinations of pole and slot numbers [XII].

Furthermore, in the case of the simulated PMSMs described in [XII], the torque ripple of the 28-pole, 24-slot machine is, except in a few points, larger than the torque ripple of the 20-pole, 24-slot machine for a same relative PM width, although its cogging torque is supposed to be lower if only looking at the LCM(p,Q_s) (LCM(28,24) = 168 > LCM(20,24) = 120). Thus, a low cogging torque does not guarantee a low torque ripple. This is also shown in Table 3.8, that gives the FE-

[3]The relative PM width is defined as the pole arc over the pole pitch.

simulated cogging torque and torque ripple for a 20-pole, 24-slot surface-mounted PMSMs with different magnet widths. The PMSM with the smallest PM width has a low amplitude of cogging torque (0.89 % of the average torque) but its torque ripple is higher than for the machine that has a higher cogging torque (3.4 %). Therefore, a compromise should be found between cogging and torque ripple, depending on which of the cogging or torque ripple is the less desirable for the application.

Table 3.8: FE-simulated cogging and torque ripple of a PMSM with 20 poles, 24 slots and different relative PM widths.

Relative PM width [-]	Cogging torque [%]	Torque ripple [%]
0.76	0.89	4.27
0.84	3.4	3.6

Analytical model

An analytical model for predicting the cogging torque of surface-mounted PM machines can be found in [63]. The ripple in the torque, when there is no cogging, no magnetic saturation and when the supplied current is sinusoidal, can be evaluated analytically from the harmonics in the back-EMF [64]:

$$T_{\text{rip}} = 2\sqrt{(\hat{E}_7 - \hat{E}_5)^2 + (\hat{E}_{13} - \hat{E}_{11})^2 + (\hat{E}_{19} - \hat{E}_{17})^2 + (\hat{E}_{25} - \hat{E}_{23})^2}/\hat{E}_1 \qquad (3.8)$$

where E_n in this case is the amplitude of the n^{th} harmonic component of the phase back-EMF.

The back-EMF and its harmonic content can be calculated rather easily for the surface-mounted PMSMs using models as in e.g. [65]. The effect of the slotting has to be taken into account. Indeed, in the case of PMSMs with concentrated windings, the slot effect modifies significantly the harmonics in the back-EMF as can be seen in Figure 3.13. In this figure, the curve above is obtained from a FE simulation (where the slotting effect is included), whereas the curve below is obtained from analytical calculations using models from [65] without taking the slot effects into account. The slotting effect can be included in the analytical calculations by using a relative permeance function in the airgap depending on the rotor position as defined in [66].

Taking into account the saturation in the analytical model is difficult, which explains why the computation of the torque ripple very often relies on the results from FE-simulations.

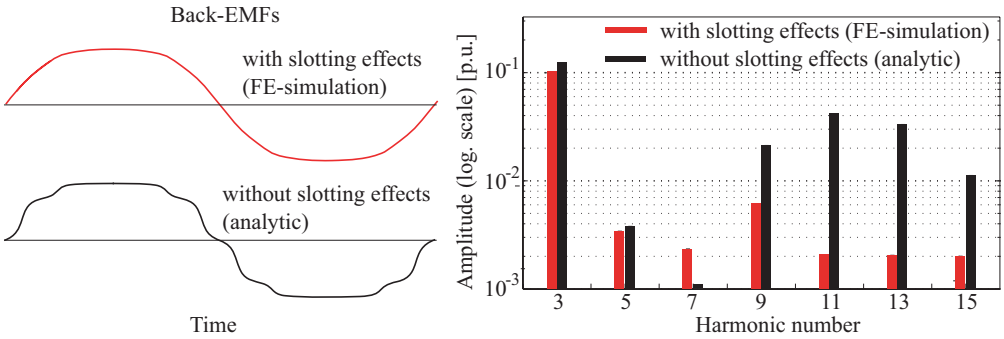

Figure 3.13: Back-EMF of a 28-pole, 24-slot PMSM with or without slotting effect.

3.2.3.4 Losses

Stator losses

Copper losses - PMSMs with concentrated windings have short end-windings, since the windings are not overlapping. These machines can then present lower axial length, copper losses and/or cost than comparable PMSMs with distributed windings as shown in [37] or [67]. Models to estimate the end-winding length, which is required for the calculation of the resistance, can be found in [37] or [68].

Iron losses - For low-speed PM motors, iron losses are generally rather low when compared to the copper losses (see Section 2.3.3). Therefore, they are often not considered for short studies. However, some particularities of PMSMs with concentrated windings can be noticed concerning the stator iron losses:

- In PMSMs with concentrated windings, there is a large zigzag leakage flux flowing through the tooth tips, as illustrated in Figure 3.7.b and Figure 3.14, due to the number of poles close to the number of slots. This zigzag leakage is responsible for rotational flux-density variations in the tooth tips and eventually for magnetic saturation that can cause high losses during flux-weakening operation. This implies also that evaluating the iron losses in the tooth tips is difficult (see Chapter 7).
- As for PMSMs with distributed windings, the stator iron losses in the tooth bodies of a machine with concentrated windings can be estimated rather accurately from flux-density waveforms in these regions. It should be taken into consideration that the flux-density waveforms in the consecutive teeth carrying the same phase are different. The difference is significant under flux-

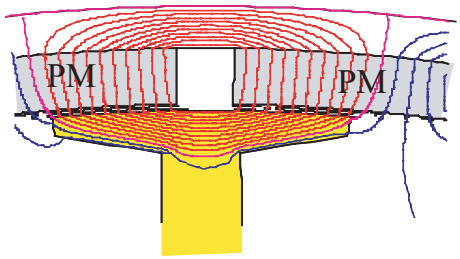

Figure 3.14: Zigzag leakage flux.

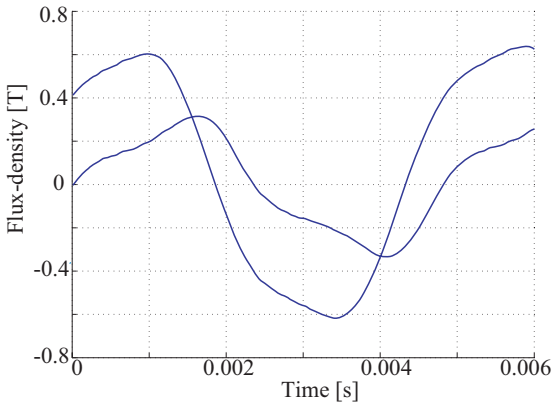

Figure 3.15: Flux-density waveforms in two consecutive teeth of a 28-pole, 24-slot PMSM with double-layer winding under flux-weakening operation.

weakening operation as is illustrated in Figure 3.15 with the measurements on a 28-pole, 24-slot PMSM with a double-layer winding. Figure 3.15 shows the radial components of the flux density in the middle of two consecutive teeth. The amplitude of the flux density is much lower in one tooth than in the other tooth. For this machine, flux-density waveforms are different in two consecutive teeth, while they are the same with different phase shift in every second teeth. This is due to the winding layout for which the phases are arranged in groups of two teeth and to the ratio of the number of poles to the number of slots.

- Iron losses in the yoke are also difficult to predict due to rotational flux-density variations in the regions over the teeth. Furthermore, the flux paths in the magnetic circuit are different between single-layer and double-layer concentrated windings PMSMs as shown in [47] and Figure 3.16. Figure 3.16.a and Figure 3.16.b show the flux lines with un-magnetized PMs and a current in phase A for a 28-pole, 24-slot PMSM with single-layer and double-layer wind-

ings, respectively. Both PMSMs have identical dimensions. In the case of the single-layer winding, the flux lines encircle several slots and the flux along the stator yoke is continuous over a quarter of the machine ($1/4 = 1/\mathrm{GCD}(p,Q_s)$). For the double-layer winding, the part of the stator yoke that is not over the slots from phase A does not carry any flux. At load conditions (Figure 3.16.c and Figure 3.16.d), the difference between the single-layer and double-layer windings is less significant due to the influence of the PMs.

Due to these particularities that are further investigated in Chapter 7, developing an analytical model to evaluate the stator iron losses for a PMSM with concentrated windings is a challenge.

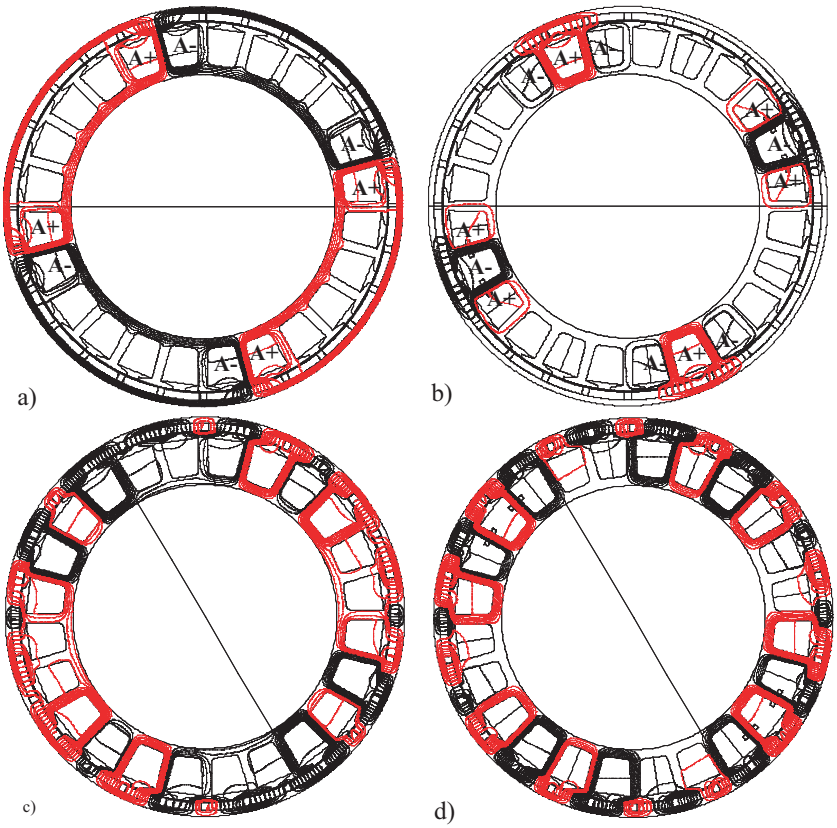

Figure 3.16: Flux lines with un-magnetized PMs and current in phase A: a) Single-layer windings; b) Double-layer windings.
Flux lines at load conditions (base speed): c) Single-layer windings; d) Double-layer windings.

Rotor losses

The main drawback of PMSMs with concentrated windings is the large rotor losses they may feature. These losses are caused by the large harmonic content in the MMF distribution.

The spectrum of the MMF for a 28-pole, 24-slot motor is shown in Figure 3.2. The harmonic component[4] that is synchronously rotating with the rotor and interacting to produce the mean torque has the order $p/2 = 14$. The other harmonics rotate asynchronously with the rotor and thus induce eddy currents in the PMs and rotor iron. As can be seen in Figure 3.2, there are large sub-harmonics in the spectrum: the harmonics of order 6 and 10 have even an higher amplitude than the 14^{th}, main harmonic component. These sub-harmonic components are responsible for most of the rotor losses according to [69, 70]. The number of sub-harmonics in the MMF distribution of a PMSM with concentrated windings depends on the combination of pole and slot numbers. Bianchi shows in [70] that for the same slot number, the rotor losses increase with an increasing pole number with some local minima for $q \approx 5/6$ and $q = 0.5$. The choice of the combination of pole and slot numbers can then be influenced by the MMF harmonic spectrum and specially the quantity and amplitude of the sub-harmonic components with a view to minimizing the rotor losses.

For example, a PMSM with 28 poles, 24 slots has a fundamental winding factor of 0.933 (Table 3.3) and 2 symmetries in the winding layout (Table 3.6.a). A PMSM with 20 poles and 24 slots has the same characteristics. The PMSM with 28 poles has a higher LCM(p,Q_s) and thus lower cogging. This does not guarantee that the torque ripple is lower than the PMSM with 20 poles, as has been shown in the previous section. Consideration on the rotor losses can then help to choose between both pole numbers. On the one hand, the MMF of the 28-pole, 24-slot PMSM has three large sub-harmonics components (2^{nd}, 6^{th} and 10^{th}) as can be seen in Figure 3.2. On the other hand, the MMF for the 20-pole, 24-slot PMSM has only a 2^{nd} and 6^{th} sub-harmonic component, as the synchronous component[4] is the $10^{th} = p/2$. Furthermore, the amplitudes of both sub-harmonics are lower than the synchronous component contrary to the 28-pole PMSM. Figure 3.17 shows the variation of flux density in the rotor iron at load conditions (obtained from a FE simulation) for a 28-pole, 24-slot and a 20-pole, 24-slot PMSM, both motors having the same stator. The magnetic circuit is linear during the simulation, and the DC component of the flux density has been subtracted in order to easily compare both waveforms. As can be seen, the waveforms have different frequencies and the amplitude of the flux-density variation is larger for the motor with 28 poles. The PMSM with 20-pole would then have lower rotor losses than the 28-pole motor,

[4]See Section 3.1.2 for the explanations on main-harmonic/fundamental component terms.

which may lead to the choice of this pole number, if other considerations as the frequency or PM size are of less importance.

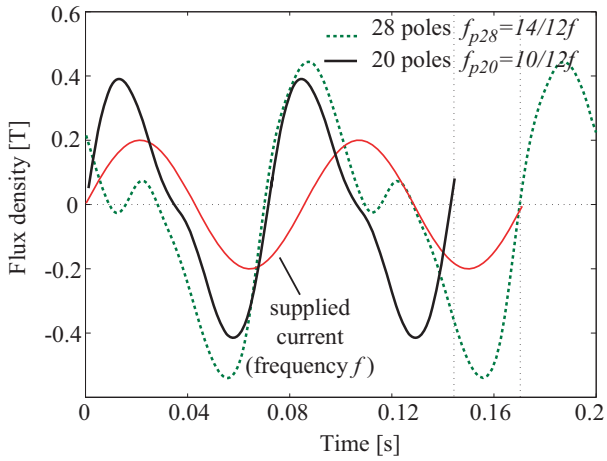

Figure 3.17: AC flux density in the rotor iron for a 28-pole, 24-slot and a 20-pole, 24-slot PMSM.

Besides carefully selecting the combination of pole and slot numbers, the rotor losses can be limited using the following means:

- Axial or circumferential segmentation of the PMs - By segmenting the PMs axially [71] or circumferentially [72], the reduction of their losses is significant. In [72] or [73], the PMs losses are more than halved by segmenting circumferentially the PMs into two pieces.
- Iron laminations in the rotor instead of a solid iron yoke.
- Change of PM material - Some PMs have a higher resistivity and therefore, lower losses are induced in them. Bonded PMs have a much higher resistivity than sintered PMs. In [74], EL-Refaie compares the performance of PMSMs with sintered PMs (resistivity of $1.5\,\mu\Omega m$) and bonded PMs (resistivity of $20\,\mu\Omega m$). In his study, he shows that the losses in bonded PMs are very low compared to the losses in the sintered non-segmented PMs. If the sintered PMs are segmented circumferentially in 4 pieces, their losses are about as high as the losses in the bonded PMs. Ferrite magnets have such a high resistivity that they are considered non-electrically conducting [75]. The losses in the magnets are then negligible in the case of the ferrite magnets, and they are very low in the rotor iron if the PMs are surface-mounted, as the equivalent airgap is large.
- Adjustment of some dimensions of the motor geometry - A large airgap decreases the losses but also the open-circuit airgap flux density and thus the

torque. The slot-opening width or placement of the PM in the rotor influence also the losses in the rotor [76].

- Number of layers in the windings - As mentioned in Section 3.2.2, PMSMs with single-layer windings and unequal teeth distribution have higher rotor losses than PMSMs with single-layer windings with equal teeth distribution which in turn have higher losses than PMSMs with double-layer windings [49].

Some analytical models for the calculation of PM losses are presented in [49, 72, 77].

3.2.4 Flux-weakening

Theory and literature study

Surface-mounted PMSMs with concentrated windings are good candidate for achieving a wide constant power speed range under flux-weakening operation, because of their high leakage inductance. Indeed, the design criterion for optimal flux-weakening operation [78] is more easily achieved with a high inductance:

$$\Psi_m = L_d I_r \tag{3.9}$$

where Ψ_m is the magnet flux linkage, L_d the d-axis inductance and I_r the rated current.

PMSMs with concentrated windings have high inductances due the large harmonic content of their MMF. This has been shown in [47] or [48]. The capacity of surface-mounted PMSMs with concentrated windings to achieve a wide constant power speed range has been shown in [79] by Magnussen, and in [73, 80–82] by EL Refaie. It is also verified in this thesis (Chapter 7). In [79], Magnussen investigates two PMSMs with double-layer concentrated windings and show their better field-weakening capability compared to a surface-mounted PMSM with distributed windings, using FE simulations. EL Refaie concentrates on PMSMs with single-layer windings, which have higher inductances than double-layer windings. He shows with measurements that a surface-mounted PMSM with 36-slot/30-pole can achieve speeds up to 5 times the base speed under constant power, and even higher speeds can be expected. In Chapter 7 of this thesis and Figure 3.18, measurements performed on a 28-pole, 24-slot surface-mounted PMSM with double-layer concentrated windings (described in Appendix C) show that this motor can run at a speed that is 6 times the base speed at a power equal to the base power.

PMSMs with buried PMs and concentrated windings have also been investigated e.g. in [73] or [83]. In [83], it is shown that a PMSM with buried PM and concentrated windings has a lower reluctance torque due to a higher d-axis inductance than

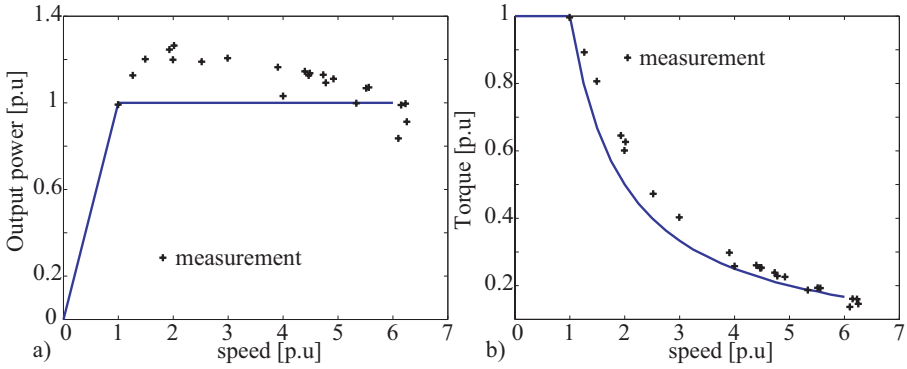

Figure 3.18: Measurements on the 28-pole, 24-slot prototype motor (Appendix C): a) Torque versus speed; b) Output power versus speed.

the machine with same rotor and distributed windings. However the flux-weakening capability is better due to the higher inductance.

Design considering flux-weakening capability

The flux-weakening capability of the PMSM depends mainly on the value of its d-axis inductance. Therefore, the design of the machine should be conducted in order to obtain the optimal value of this inductance. Furthermore, the risk of demagnetization of PMs under flux-weakening operation should be evaluated. As mentioned earlier, PMSMs with single-layer concentrated windings have higher inductances than PMSMs with double-layer concentrated windings because of the high harmonic content of the MMF distribution. The value of the inductance can also be increased by adjusting the dimensions of the tooth tips.

The influence of the tooth tips' dimensions on the inductance values is shown for an example in Figure 3.19 and Figure 3.20. In this example, the dimension of the tooth tip from a surface-mounted PMSM with 10-pole 12-slot is varied in thickness (the slot opening width is constant), as shown in Figure 3.19. The d- and q-axes inductances, which are given in Figure 3.20, are computed from a blocked-rotor test by feeding one phase with a sinusoidal current. In this figure, the d-axis inductance from the geometry with the larger tooth-tip is defined as a reference equal to 1 p.u. As can be seen, the thinner the tooth tip, the lower the d-axis inductance. Furthermore, for large negative d-axis currents, the d-axis inductance begins to drop due to the saturation in the tooth tips, as Figure 3.19 illustrates for a current of -1 p.u. This drop in the d-axis inductance coincide with large negative fields in the PMs that risk to demagnetize them. The q-axis inductance begins to drop for lower

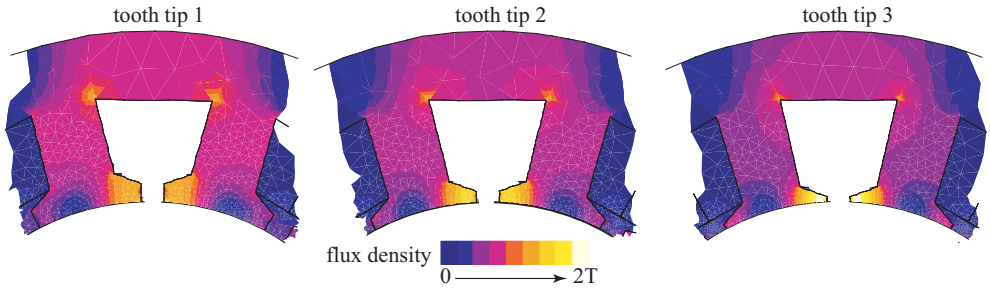

Figure 3.19: Flux density in the tested tooth tips at a current of -1 p.u in *d*-axis position.

q-axis current (in absolute value) when the tooth tip is thin, due to the saturation in the tooth tip. This is not an issue, as the machine has surface-mounted PMs and no saliency when the current is zero. At base speed, the *d*-axis current is zero and a lower *q*-axis inductance would actually improve the power factor. This short study shows that the tooth tips should be designed carefully as their dimensions can influence significantly the values of both *d*- and *q*-axes inductances, especially for machines with high electric loadings. Moreover, a FE tool facilitates greatly the design of the tooth tip.

The tooth tips are also the source of iron losses especially under flux-weakening operation (see Chapter 7). Decreasing their size may decrease the iron losses but also the *d*-axis inductance. Therefore a compromise should be found.

Another property to take into consideration when estimating the *d*-axis inductance is the end-effects, whose importance depends on the size of the machine. PMSMs designed for a low-speed application have often a large diameter for a short axial length. The fringing flux effects at both ends of the machines can then be relatively important when the machine is flat. These effects may increase the *d*-axis inductance value by approximately 10 % ([84], Chapter 6).

In [85], the "parameter plane concept" tool is described and used to compare different designs when changing parameters such as magnet remanence flux density, the number of turns in the windings or the airgap area, with a view to optimizing the flux-weakening capability of surface-mounted PMSMs with concentrated windings.

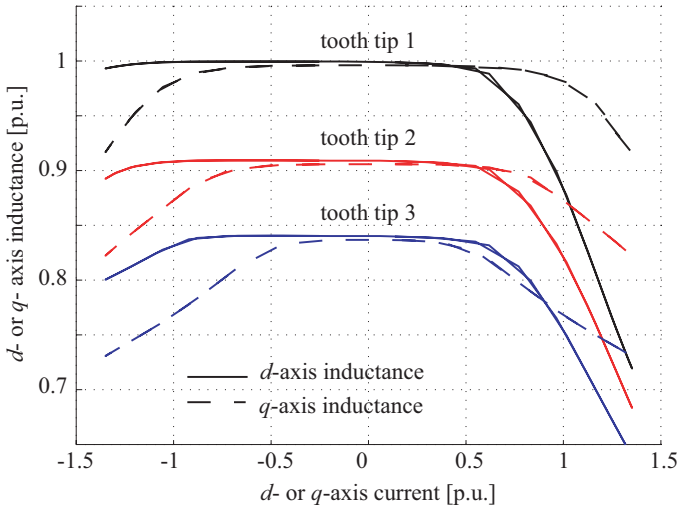

Figure 3.20: *d*- and *q*-axes inductances versus *d*- respective *q*-axis current for different tooth tip dimensions.

3.2.5 Fault-tolerance

For some applications, e.g. electrical actuators in aircrafts, tolerance to faults is critical for safety reasons. PMSMs with concentrated windings, especially with more than 3 phases, have good fault tolerance capabilities. Methods to select the combination of pole and slot numbers for fault-tolerant PMSMs with more than 3 phases can be found in [44, 86].

3.3 Summary

When designing PMSMs with concentrated windings, some choices specific to these machines have to be made, in order to obtain the most suitable design for the application. Figure 3.21 summarizes these choices and their influence on the design. At first, the designer should select the manufacturing method of the stator core, which gives an estimation of the slot fill factor. Then the number of winding layers should be selected, followed by the combination of pole and slot numbers. This combination can be selected to obtain a high fundamental winding factor, many symmetries in the winding layout, low amplitude and low number of sub-harmonics in the MMF distribution and eventually a low cogging torque (Figure 3.22). The design can then be conducted just as any PMSM with distributed windings. However, the tooth tips, if there are any, should be carefully designed, in order to obtain an optimal

inductance value decisive for a good flux-weakening capability or to avoid too high iron losses or torque ripple.

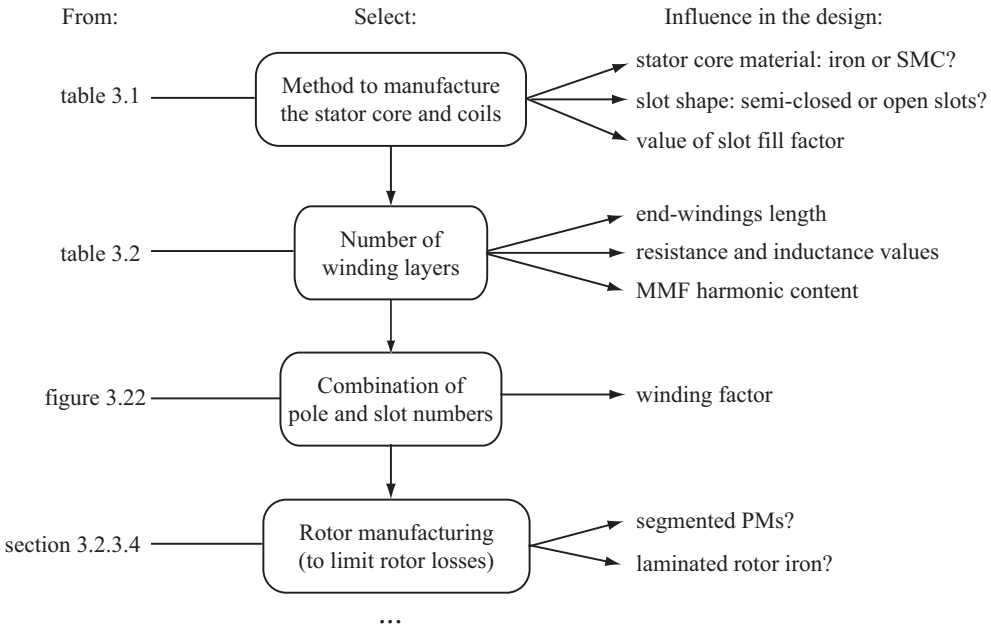

Figure 3.21: Characteristics of the design procedure of PMSMs with concentrated windings.

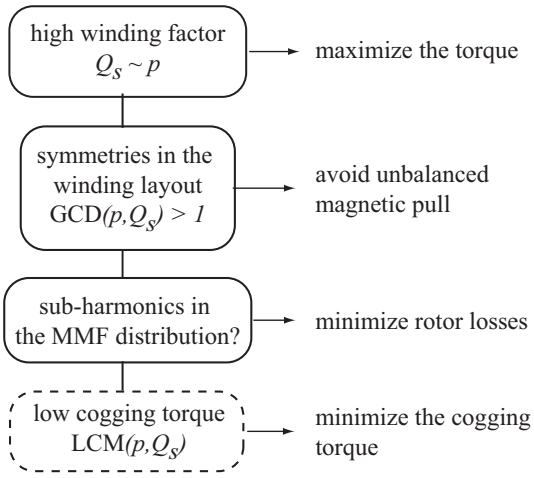

Figure 3.22: How to select the combination of pole and slot numbers.

Some references for analytical models useful for the design of PMSMs with concentrated windings can be found in Table 3.9. This list of reference is not exhaustive. Additional references can be found in EL-Refaie's thesis [39] or in the references given in the table. In [65, 66, 87, 88], Zhu proposes models to calculate the open-circuit field and armature field for surface-mounted PMSMs. It accounts for both overlapping and non-overlapping windings. In [89], Proca shows how the models from Zhu can be included in a procedure to design surface-mounted PMSMs. Thus, the torque ripple or back-EMF are derived from Zhu's models. In [39], EL-Refaie presents also a design procedure based on Zhu's models but with models specific to PMSMs with non-overlapping concentrated windings. His procedure includes also resistance, inductance, and losses calculations of such machines. The author of this thesis has also implemented Zhu's model in the web-based design tool Emetor[5] [XI]. This tool allows designing PMSMs with overlapping or non-overlapping windings.

Table 3.9: References to analytical models useful for PMSM design with concentrated windings.

Properties	Reference	Comments
Open-circuit airgap flux density	[65, 87]	inner/outer rotor surface-mounted PMSMs with parallel or radial PMs magnetization
Armature-reaction airgap flux density	[88]	for distributed windings (slotless stator)
	[65]	for concentrated windings
Slot effects	[66]	calculation of a relative permeance
Winding layout	[36]	also discussed in Appendix B
	[51]	based on the star of slot
Winding factor	[37, 47] Section 3.2.3	from EMF phasors
	[39]	from winding function
	[45, 52]	from closed-form expressions
Inductances	[39, 90, 91]	2D-models
Resistance	[37, 39]	DC resistance of single- or double-layer concentrated windings
	[92, 93]	with skin and proximity effects
Cogging torque	[61, 63]	based on [66]
Unbalanced magnetic pull	[55, 58]	
Rotor iron losses	[94]	in case of solid iron back
Rotor magnet losses	[49, 72, 77]	
Design procedure	[89]	for distributed windings
	[39]	for concentrated windings
	Emetor[5]	for distributed and concentrated windings

[5] www.eme.ee.kth.se/emetor

Many examples of PMSMs with concentrated windings can nowadays be found in the literature. A non-exhaustive list of such machines on which experimental tests were conducted is given in Table 3.10. The most popular combinations of pole and slot numbers are those giving a number of slots per pole per phase q equal to 2/5 or 2/7. PMSMs with $q = 0.5$ have sometimes an irregular distribution of teeth as in [35, 76] in order to increase the fundamental winding factor. The modular PM machine with the lowest number of poles is the one with 10 poles, 12 slots. Therefore, this combination of pole and slot numbers is the obvious choice for the applications requiring middle-range speeds in order to limit the nominal frequency. Other publications showing measurements on 10-pole, 12-slot motors that are not mentioned in Table 3.10 are [46, 47].

Table 3.10: Prototype PMSMs with concentrated windings in literature.

p/Q_s	q	layer no	PM	power [kW]	speed [rpm]	ref.	application
2/3	0.5	2	surface	2	18 000	[56]	vacuum pump
4/6	0.5	2	buried	11	6000	[83]	field weak.
6/9	0.5	2	surface	1.4	3000	[95]	SMC
8/12	0.5	2	surface	1.6	3000	[95]	SMC
10/12	2/5	1 & 2	surface	0.23	400	[48]	-
10/12	2/5	2	buried	45	420	[42]	pulp & paper
14/15	0.357	2	surface	20	2000	[96]	traction
16/24	0.5	1 & 2	bur. & surf.	45	1000	[76]	field weak.
20/30	0.5	1	buried	150	∼200	[35]	traction
22/24	0.364	2	buried	18.5	1700	[97]	automotive
24/18	0.5	2	surface	∼0.2	∼150	[98]	SMC bicycle
28/24	2/7	1	surface	0.26	250	[38]	bicycle
28/24	2/7	1	surface	0.80	250	app. B.2	field weak.
24/36	0.5	2	surface	5	240	[34]	wind turbine
26/36	0.462	2	surface	10	200	[34]	wind turbine
30/36	2/5	1	surface	6	600	[82]	traction

4 Design of a PM motor for a low-speed direct-drive mixer

In this chapter, the possibility to replace a geared mixer by a direct-drive mixer is investigated for the waste-water application described in Section 2.2.7. A design study is conducted to find the most appropriate design of a PMSM for the direct-drive mixer. The reasons behind the selections of the winding type, rotor configuration, PM placement, and PM material are revealed. After showing how the chosen PMSM may be manufactured, the direct-drive and geared mixers are compared and conclusions are drawn.

4.1 Design study

4.1.1 Design and optimization procedures

The design of a PMSM for the direct-drive mixer is conducted by solving an optimization problem, using an own-developed numerical design tool in Matlab[1]. The models used in the design tool, based on the assumption of a linear magnetic circuit, are described in [VI] and verified with FE simulations. Various optimized designs with different number of poles, rotor or winding types can then be calculated and compared. The optimization procedure is shown in Figure 4.1. The goal of the optimization is to minimize the active weight of the motor while fulfilling the motors specifications given in Table 4.1. The constraints that guarantee the required mechanical, thermal and magnetic behaviors of the machine given in Table 4.2 should also be fulfilled. Thus, all the designs are calculated for the same nominal torque (840 Nm) and nominal speed (50 rpm). The exterior diameter is limited to 500 mm and a limit of 5.5 kg is set on the PM weight (for the NdFeB magnets) because of the relatively high cost of the PM material (see Section 4.1.5). Some constraints on the teeth and stator yoke dimensions are defined in order to guarantee a mechanically rigid structure. The magnetic flux density in the teeth and stator and rotor

[1]The online PMSM design tool "Emetor" [XI] is a spin-off from the Matlab tool.

yokes are limited at open-circuit condition in order to prevent from saturation and thus too inaccurate results due to the assumptions made in the analytical models. The copper losses cannot exceed 700 W in order to avoid a low efficiency and high temperature in the windings. All the calculated motors have the same square slot shape with a tooth width constant along the tooth.

The influence of different parameters on the design can be seen in torque equation (4.1):

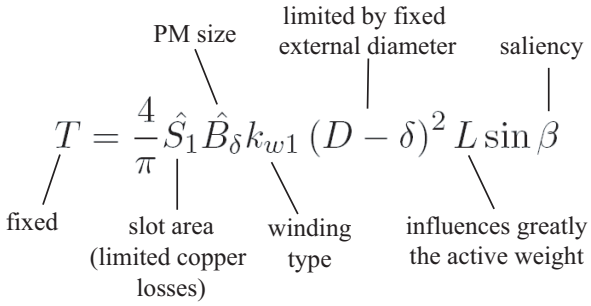

$$T = \frac{4}{\pi} \hat{S}_1 \hat{B}_\delta k_{w1} (D - \delta)^2 L \sin \beta \tag{4.1}$$

where

T torque.
$\hat{S}_1$ maximum of the fundamental current loading;
$\hat{B}_\delta$ maximum of the fundamental open-circuit airgap flux density;
k_{w1} fundamental winding factor;
D inner stator diameter;
δ airgap length;
L active length;
β angle between the d-axis and the current vector;

The torque T is constant and equal to its rated value. The fundamental current loading S_1 is directly related to the slot area, if the copper losses and external diameter are fixed and equal to their maximum allowable values (which is almost always the case). The slots size influences in turn the dimension of the airgap diameter $D - \delta$. The fundamental winding factor k_{w1} varies depending on the winding type; a lower fundamental winding factor should be compensated by a higher current loading, open-circuit airgap flux density or a larger active length. The fundamental open-circuit airgap flux density B_δ is limited by the constraint on the PM weight, and the PM weight depends on the active length. The active length influences greatly the active weight, if the external diameter is constant.

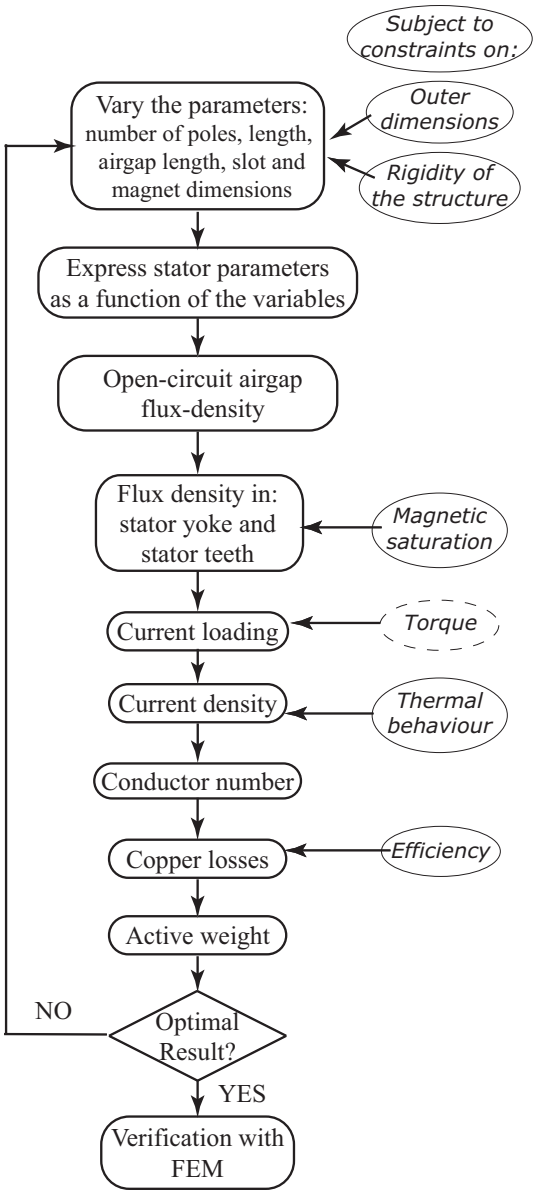

Figure 4.1: Optimization procedure.

Table 4.1: Design specifications of the direct-drive mixer motor.

Maximum outer diameter	500 mm
Maximum length	500 mm
Maximum weight	150 kg
Minimum efficiency	73 %
Nominal torque	840 Nm
Nominal speed	50 rpm

Table 4.2: Constraints (More details about the constraints can be found in [VI]).

Objective of the constraints	Description of the constraint
guarantee the rigidity of the mechanical structure	stator yoke height at least half the slot height slot width between 0.15 and 0.5 times the slot height tooth width at least 30 % of the slot pitch slot opening width at least 2 mm slot opening height at least 2 mm
avoid magnetic saturation	flux density in stator teeth under 1.6 T flux density in stator yoke under 1.4 T flux density in rotor yoke under 1.4 T fundamental airgap flux density under 1.1 T
prevent high temperature and guarantee a minimum efficiency	winding temperature set to 80 °C copper losses under 700 W
limit the price limit the machine weight	magnet weight under 5.5 kg machine weight under 150 kg

4.1.2 Distributed versus non-overlapping concentrated windings

Distributed windings

When the number of poles is high, the number of slot per pole per phase q is chosen equal to 1 in order to limit the number of slots. The fundamental winding factor k_{w1} is equal to 1. So do also the odd harmonics of the winding factor. Therefore the torque ripple of the machines with $q = 1$ is usually high, if there is no skew. The windings are overlapping giving rather long end-windings compared to the machine length, as the machines for low-speed application are often short with a large diameter.

Several designs of inner rotor surface-mounted PM (SMPM) machines with distributed windings, $q = 1$ and NdFeB magnets are calculated following the optimization procedure. The number of poles is varied from 20 to 70. Figure 4.2 shows how the active weight decreases for an increasing number of poles. For pole numbers over 50, it decreases slower due to the constraints on the rigidity of the structure. A possible design with 70-pole is presented in Figure 4.3.a. The external diameter of the machine is as large as possible and the active length as short as possible in order to minimize the active weight. As in addition the copper losses cannot exceed 700 W, the slots should have a minimum area and therefore they are thin and long. The torque ripple of these machines with distributed windings is approximately 10 %. The length of the end-windings is approximately 15 % of the machine's active length.

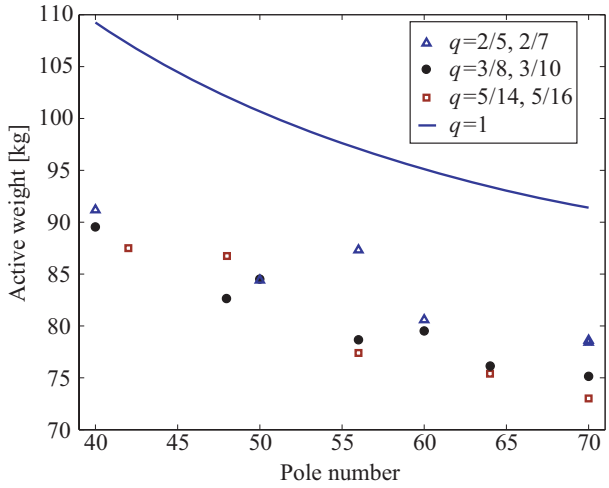

Figure 4.2: Active motor weight as a function of the pole number for SMPM motors with concentrated and distributed windings.

Non-overlapping concentrated windings

The commonly mentioned advantages of the non-overlapping concentrated windings are the short end-windings, low cogging torque and torque ripple, easy assembling of the stator and cheaper manufacturing as there are fewer slots. On the other hand, the fundamental winding factor is lower and the MMF has a large harmonic content which causes losses in the rotor PMs and iron (see Chapter 3).

In the case of the mixer application, double-layer concentrated windings are the most appropriate. Indeed, with the lower harmonic content in the MMF, the losses and torque ripple are lower than with a single-layer winding. Furthermore, there are no requirement on a wide speed range of constant power operation and no constraints on fault tolerance for the mixer.

The combinations of pole and slot numbers selected for the study give high fundamental winding factors. Moreover, the corresponding winding layouts present many symmetries to avoid an unbalanced magnetic force. They are the combinations with the number of slots per pole per phase q equal to 2/5 and 2/7 giving a fundamental winding factor k_{w1} equal to 0.933, q=3/8 and 3/10 with k_{w1}=0.945 and q=5/14 and 5/16 with k_{w1}=0.951.

Figure 4.2 shows the active weight as a function of the pole number for different values of q. The trend for SMPM motors with concentrated windings is that the active weight decreases with an increasing pole number. Some points do not follow this trend due to the fact that the active weight also varies with the number of slots. Thus, the motors with $q = 2/5$ or $2/7$ are slightly heavier than the others, because of their lower fundamental winding factor. Figure 4.2 reveals also that the motors with concentrated windings are approximately 15 kg lighter than those with distributed windings ($q = 1$). Since there are fewer teeth in designs with concentrated windings, both the slots and teeth can be wider, as Figure 4.3.b shows. As in addition the end-windings are shorter, the current loading S_1 can be higher for given copper losses (equation (4.1)). Furthermore, the PMs are allowed to be thicker and the open-circuit airgap flux density B_δ to be higher without saturating the teeth. This allows the motors with concentrated windings to be shorter and thus lighter even though the fundamental winding factor is lower and airgap diameter smaller than for machines with distributed windings. Another interesting characteristic is the reduction of the torque ripple from 10 % for machines with distributed windings to under 3 % with concentrated windings.

The advantages of the machines with concentrated windings are substantial with their lower active weight and lower torque ripple. Therefore these machines are a good choice for the mixer.

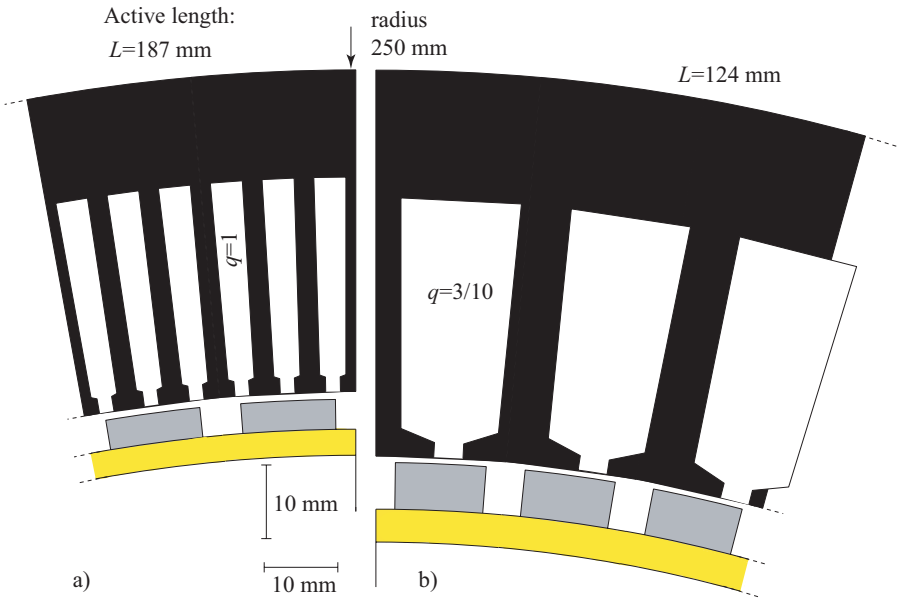

Figure 4.3: Geometries of two 70-pole SMPM motors: a) With distributed windings ($q = 1$); b) With concentrated windings ($q = 3/10$).

4.1.3 Inner versus outer rotor

The outer rotor structure is often chosen because of its suitability in the mechanical drive. For example, this structure is well adapted for in-wheel motors [38, 45] or wind turbines [99], as the wheel's or turbine's hub can be fixed directly to the outer rotor, which makes the system more compact.

In the case of the mixer, fixing the propellers blades on an outer rotor does not bring any decisive advantage [31]. Therefore, other aspects than the mechanical design should be taken into account for the choice of the rotor configuration:

- Thermal design - When running, the submersed mixer makes the waste-water circulate around the motor. This circulating water should be sufficient to dissipate the motor losses. The main source of losses, the windings, is located in the stator. Therefore, in the case of an outer rotor, the cooling would be less efficient as the stator windings are further away from the water.
- Magnetic design - A SMPM motor with an outer rotor has usually a larger airgap diameter than a SMPM motor with inner rotor having the same external diameter, as illustrated in Figure 4.4. The torque being proportional to the square of the airgap diameter (equation (4.1)), the length and thus the

weight of the machine can be decreased for a machine with an outer rotor. Therefore, the designs of outer-rotor SMPM motors obtained by following the optimization procedure are approximately 15 % lighter than the motors with an inner rotor, if only the active weight is considered [VI].

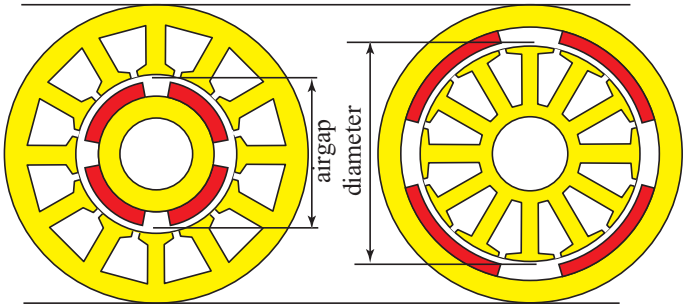

Figure 4.4: Inner- and outer-rotor PMSMs with same external diameter.

- Winding type - In the case of non-overlapping concentrated windings, PMSMs with outer rotors are slightly easier to wind since the teeth point outward, especially if the slots are open.
- PM placement - if the PMs are surface-mounted, they are subject to centrifugal forces during the rotation. The centrifugal forces are proportional to the radius and to the square of the speed. If the rotor is internal, the centrifugal forces tend to detach the PMs and a bandage or other protection is often necessary. However in the case of an external rotor, the PMs are pressed on the rotor iron by the centrifugal forces, making their detachment more improbable.
  Outer rotors with buried PMs are rare. The mechanical design is difficult and it is not guaranteed that the airgap diameter is larger with an outer rotor with buried PM than with an inner rotor.

Considering these different aspects, the solution of an inner rotor is chosen for the mixer's motor. The better cooling and the possible use of a buried PMs structure (see Section 4.1.4) are the main arguments for this solution.

4.1.4 Surface-mounted versus buried PMs

Radial-flux PMSMs can be classified in three categories: SMPM machines, inset PM machines and buried or interior PM machines. The main advantage of the SMPM machine is its simplicity and consequently a lower construction cost compared to other PM machines. The main drawback is the exposition of the permanent magnets to demagnetization fields.

The inset PM machines have surface-mounted PMs with iron interpoles that give a salient structure (Figure A.2 in Appendix A). Therefore, inset PM machines combine the advantages of the SMPM machines, with the possibility to have a reluctance torque due to the salient structure.

An advantage of the buried PM machine configuration is the possibility to concentrate the flux generated by the PMs in the rotor and thus achieve a high open-circuit airgap flux density. Moreover, machines with buried PM are salient and thus a reluctance torque is produced in addition to the alignment torque from the PM. They can also achieve wide speed range of constant power operation [78]. Finally, the buried PMs are well protected against demagnetization and mechanical stress.

There are many ways to place the buried PMs in the rotor (Figure A.2 in Appendix A). The most attractive solution for the application, as the number of poles is high, is to have tangentially-magnetized PMs (also called sometimes the spoke topology [100]), as illustrated in Figure 4.5.a. As for the SMPM configuration, optimized designs with different number of poles and concentrated windings are calculated, using the procedure described in Figure 4.1. Appendix D gives the model added to the design tool that are used to analytically calculate the open-circuit airgap flux density when the PMs are tangentially magnetized.

Figure 4.5 shows two 70-pole, 63-slot motors with tangentially-magnetized and surface-mounted PMs respectively. When the PMs are buried, the PM flux concentrates in the rotor iron which allows a higher open-circuit airgap flux density than with surface-mounted PMs. The current loading is then lower for the motor with buried PMs leading to smaller slots and a larger airgap diameter (equation (4.1)). The machine can then be shorter. Therefore, the motor with tangentially-magnetized PMs has an active weight that is approximately 20 kg lower than the SMPM motor, as can be seen in Table 4.3. Furthermore, the weight of the PM material is substantially lower. The advantages of the concentrated windings over distributed windings ($q = 1$) can also be noticed in this table: Besides the 20 kg lower active weight, the torque ripple is consequently decreased, especially in the case of tangentially-magnetized PMs. The torque ripple is obtained from 2D-FE simulations.

The configuration with tangentially-magnetized PMs is chosen for the mixer application as it gives a substantially lower motor active weight and especially the PM weight is decreased, which may give a lower cost. This configuration opens also for the use of cheaper PMs.

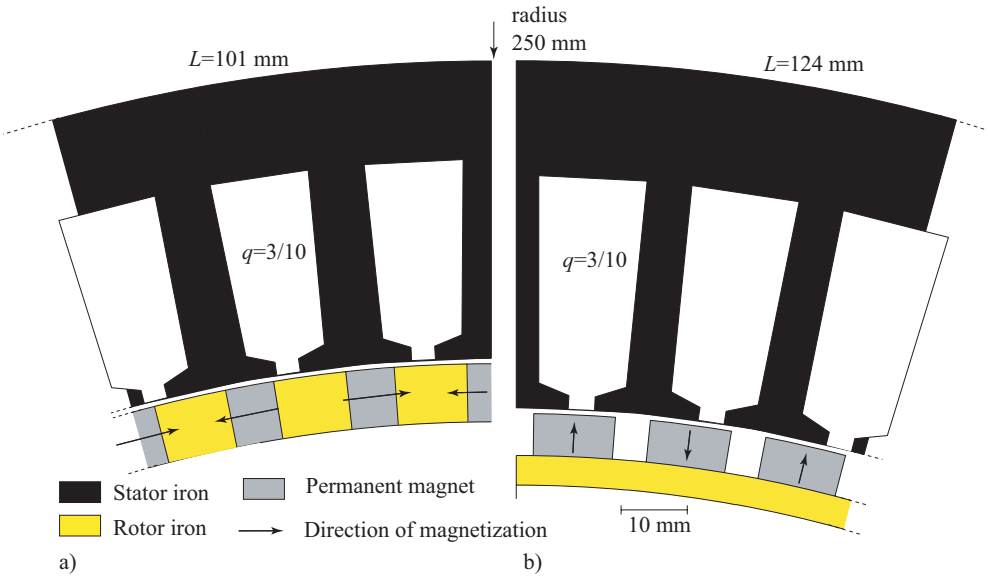

Figure 4.5: Geometries of two 70-pole, 63-slot motors: a) With tangentially-magnetized PMs; b) With surface-mounted PMs.

Table 4.3: Results for 70-pole SMPM and tangentially-magnetized PM designs.

Motor configuration	Design q, pole/slot	Active weight [kg]	PM weight [kg]	Torque ripple [%]
surface-mounted PMs	$q = 3/10$, 70/63	76.1	5	2.4
	$q = 1$, 70/210	91.4	5.5	9.3
tangentially-magnetized PMs	$q = 3/10$, 70/63	55.9	3.4	4.2
	$q = 1$, 70/210	76.4	5.5	41.7

4.1.5 Magnet material

Ferrite magnets

For the tangentially-magnetized PM motor designs, the NdFeB magnets may be replaced with ferrite magnets. Indeed, the flux concentration in the rotor allows reaching high open-circuit airgap flux density with a low weight of NdFeB magnets. Furthermore, the designs with NdFeB magnets are light thanks to the use of concentrated windings. With ferrite magnets, the designs, though heavier, may still be lighter than the induction motor and its gearbox. The ferrite magnets have poorer magnetic properties than the NdFeB magnets but they are much cheaper. The solution with ferrite magnets can then be a better compromise between the machine's weight and the machine's cost.

The advantages of ferrite magnets are listed below [75]:

- Ferrite magnets are very cheap compared to NdFeB magnets. In 2005, their cost was approximately 5.5 Euro/kg, whereas the NdFeB magnets costed approximately 50 Euro/kg [31]. Since 2005, the political and economical situation in China has led to a strong increase in the price of NdFeB magnets. The price for ferrite magnets has been stable until 2008 but it is also starting to change. In 2008, the price for NdFeB magnets is estimated around 120 Euro/kg while the ferrite magnets cost around 7 Euro/kg [101].
- Demagnetization can occur below $-40\,^{\circ}\mathrm{C}$ and over $200\,^{\circ}\mathrm{C}$ [102]. These temperatures will never be reached for the considered application: the mixer is submersed and the temperature in the windings is estimated around $80\,^{\circ}\mathrm{C}$.
- Ferrite magnets are electrically non conducting. This means that there is no problem of eddy currents in these magnets.
- No corrosion.
- They are easy to manipulate compared to NdFeB magnets, as they are not as strong.
- They are easy to magnetize.

Their drawbacks are:

- Ferrite magnets have poorer magnetic properties i.e. a low remanence flux density (0.3–0.4 T against 1.1–1.3 T for NdFeB magnets) and a low energy density (20–35 kJ/m^3 against 250–350 kJ/m^3) [103]. Therefore, PMSMs with surface-mounted magnets will have low open-circuit airgap flux densities. When the PMs are buried, it is possible with the flux concentration to reach the same open-circuit airgap flux density as in the NdFeB magnet machines, but the quantity of ferrite material is much more important. The weight of the rotor is therefore much higher. However it can be noticed that the ferrite magnets have a lower density than the NdFeB magnets (5000 kg/m^3 against 7500 kg/m^3).
- Since the rotor is larger with ferrite magnets, an outer-rotor structure has no longer a larger airgap diameter.
- The remanence flux density varies consequently with the temperature (-0.2 %/K) [103].

Design with ferrite magnets

The possibility to replace NdFeB magnets with ferrite magnets is investigated for a 56-pole, 63-slot tangentially-magnetized PM motor. This combination of pole and slot numbers is chosen because it gives a high fundamental winding factor (0.945) and no unbalanced magnetic pull. The number of poles is chosen as a compromise between the active weight that is low for a high slot number, and the manufacturing that is easier and cheaper with fewer PMs and teeth [31].

The machine with NdFeB magnets, shown in Figure 4.6.a has a PM width w_m of 10 mm. At open-circuit conditions, its fundamental airgap flux density is high, equal to 1.16 T. Since the ferrite magnets have a remanence flux density much lower than the NdFeB magnets (0.4 T against 1.08 T), they have to be wider in order to achieve a comparable airgap flux density. The influence of the ferrite magnet width w_m on the open-circuit airgap flux density is shown in Figure 4.7.a and Figure 4.7.b. As can be seen, the airgap flux density produced by the PMs is increasing with a reduced rate the wider the PM is. Therefore, it would not be efficient to try to reach a very high airgap flux density with ferrite magnets. Figure 4.8 shows how efficient the PMs are utilized in the machine. The operating points of PMs with a width over 30 mm get further away the maximum energy product operating point when the magnet width increases. The magnet is best utilized when its width is between 30 mm and 40 mm, giving a open-circuit airgap flux density of approximately 0.9 T.

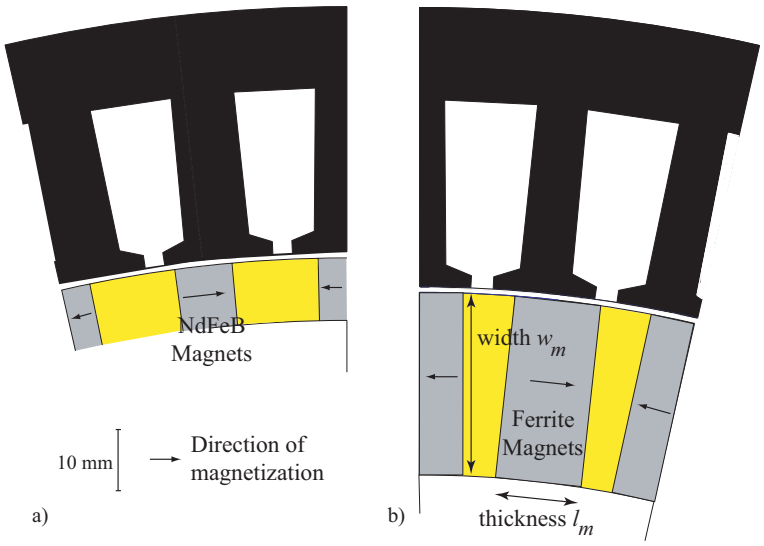

Figure 4.6: Geometries of two 56-pole tangentially-magnetized PM motors: a) With NdFeB magnets; b) With ferrite magnets.

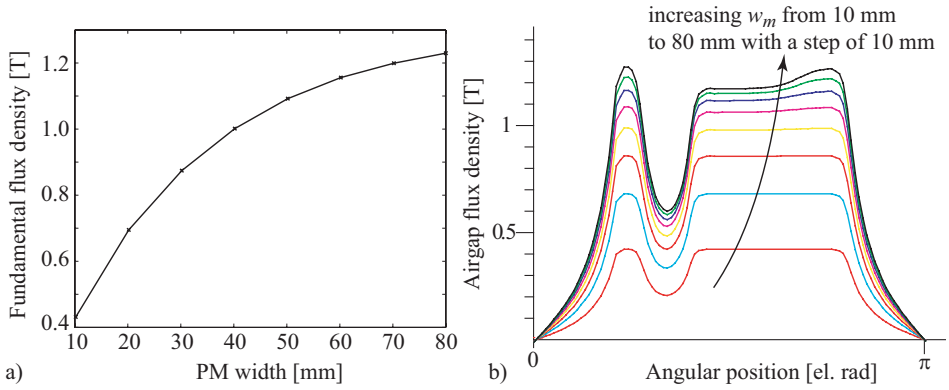

Figure 4.7: Open-circuit airgap flux densities for different ferrite PMs widths w_m.

The PM thickness l_m should also be adjusted in order to avoid saturation in the rotor iron. Furthermore, the PM thickness influences also the active rotor weight. Figure 4.9 shows how the open-circuit airgap flux density varies as a function of the PM thickness, the PM width being set to 30 mm. As can be seen, the fundamental open-circuit airgap flux density increases to a certain point with an increasing PM thickness. Over $l_m = 14$ mm, it decreases very rapidly, due to the saturation in the rotor iron. With $w_m = 30$ mm and $l_m = 14$ mm, the open-circuit airgap flux density is maximized. The flux density in the PMs is of approximately 0.2 T, which gives an

operating point in the magnet close to the one giving the maximum energy product, as can be seen in Figure 4.8. The cross-section of the design with w_m=30 mm and l_m=14 mm is represented in Figure 4.6.b.

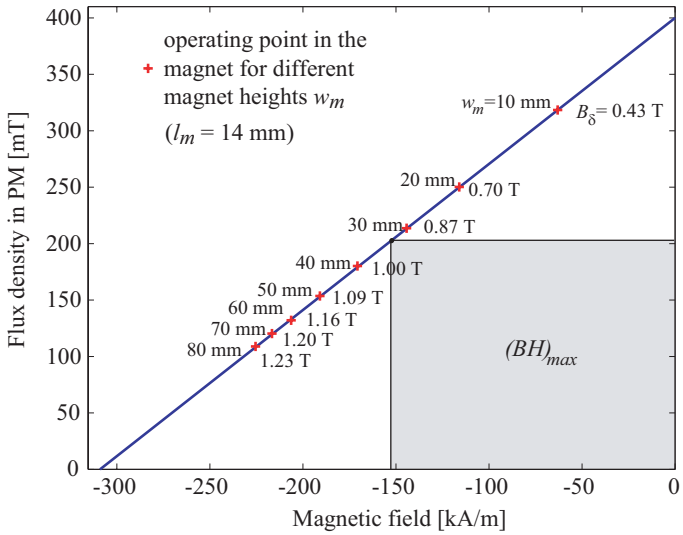

Figure 4.8: Magnetization curve of the ferrite magnet material with operating points of designs with different PM widths and same PM thickness.

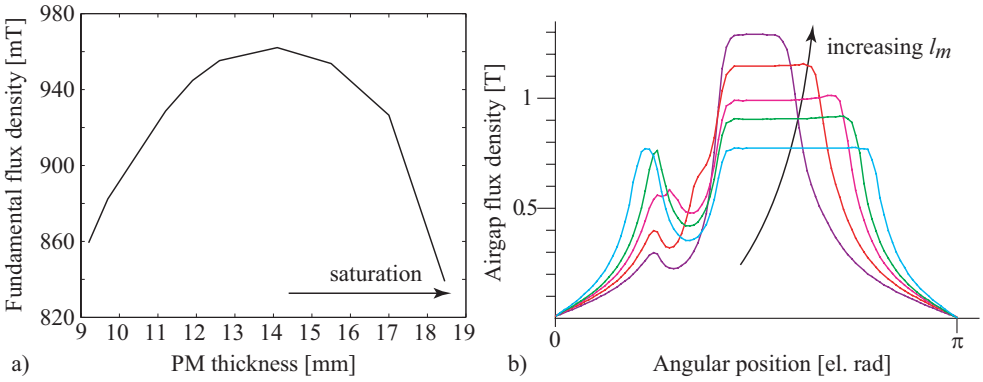

Figure 4.9: Open-circuit airgap flux densities for different magnet thicknesses l_m.

Comparison

The 56-pole, 63-slot designs with NdFeB or ferrite magnets can be compared using Figure 4.6 and Table 4.4. Both machines have the same torque, copper losses and active length. The machine with ferrite magnets has larger slots and a higher current loading in order to compensate for the lower open-circuit airgap flux density B_δ. As can be seen in Figure 4.6, the rotor of the machine with ferrite magnets is much wider. This results in a heavier rotor in the case of ferrite magnets and a higher total active weight ($\sim$+50 %). Both machines have the same torque ripple at load conditions. The iron losses at load conditions, calculated with FE simulations, are slightly higher for the machine with ferrite magnets, since there is more iron both in the stator and rotor. However, the losses in the PM are expected to be much lower with ferrite magnets. The machine with ferrite magnets is much heavier, but its cost is substantially lower ($\sim$-30 %).

Table 4.4: Some characteristics of the designs with NdFeB and ferrite magnets.

Results	Units	NdFeB	Ferrite
B_δ	T	1.16	0.96
PM width	mm	10.2	30
PM thickness	mm	9.4	14.1
Torque ripple	%	3.7	3.7
PM weight	kg	4.8	16.4
Rotor weight	kg	12.1	32.2
Total active weight	kg	62.2	97.2
Iron losses (stator+rotor)	W	73.9+6.3	76.7+12.8
Cost of active material	Euro	377	251

Table 4.5: Material price in 2005.

	NdFeB magnets	Ferrite magnets	Lamination plates	Copper wire
Price [Euro/kg]	55	5.5	1.65	3.1

The prices for the material used for the cost calculations are given in Table 4.5 and dated from 2005. They were not updated with more recent prices. If the prices from 2008 were taken into account, the difference in cost between the NdFeB-magnets motor and the ferrite-magnet motor would be about the same or even greater. Indeed, the NdFeB magnets cost in April 2008 approximately 17 times more than the ferrite magnets (instead of 10 times more) while the price of copper has almost doubled at the same time.

4.2 Method to manufacture the machine with buried PMs

4.2.1 Rotor

A motor with ferrite magnets fulfills the specifications for the direct-drive mixer. However, the originality of the rotor demands further investigations on how to manufacture it. The mechanical design of an optimized motor with ferrite magnets presented in Section 4.3.1 has been conducted by Hallberg in [31]. In order to keep the PMs in place, the iron pieces and the PMs are profiled as illustrated in Figure 4.10.a. The iron pieces and PMs are fixed to the aluminium hub by molding the gap between them and the hub with a plastic filler material [31]. The whole rotor is illustrated in Figure 4.10.b. With the new PM shape, the fundamental open-circuit airgap flux density is slightly decreased, reducing the torque by few percents. There is also some flux leakage at the bottom of the PM.

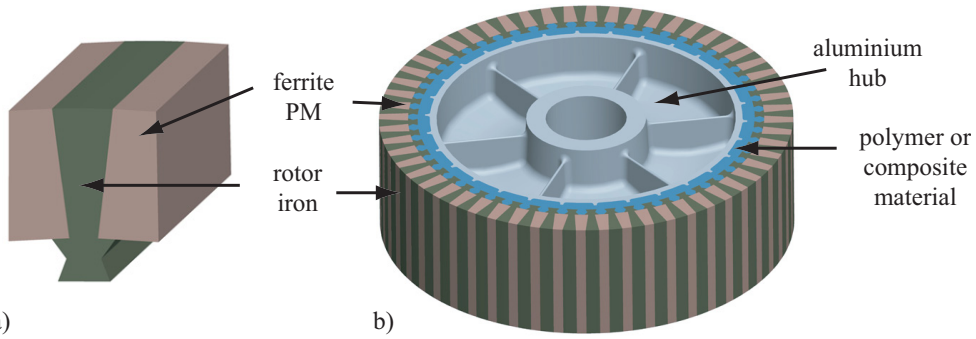

Figure 4.10: a) Two ferrite magnets and an iron piece; b) Assembled rotor proposed by Hallberg [31].

4.2.2 Non-active components

The non-active components are those components that do not participate to the torque production, such as the bearings, housing and seals. The motor being submersed, the housing of the machine should be carefully designed to avoid any water leakage. Figure 4.11.a shows a drawing proposed by Hallberg of the motor with its inactive components.

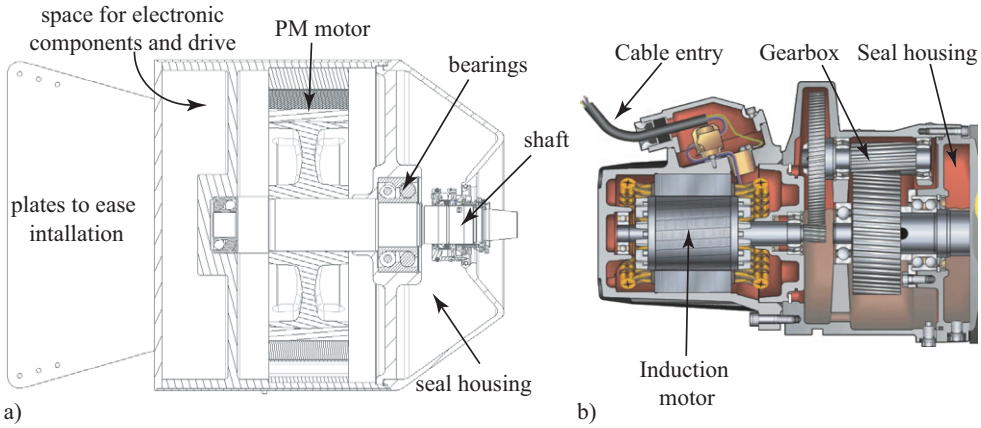

Figure 4.11: a) Hallberg's direct-drive mixer design [31]; b) Geared mixer (∼same scale).

4.3 Comparison of direct-drive and geared mixers

4.3.1 Final design

Taking into account the modifications for the manufacturing of the rotor, a final design with ferrite magnets and concentrated windings is calculated. Table 4.6 shows some characteristics of this design, while its geometry with flux lines at open-circuit conditions is given in Figure 4.12.

The motor losses are estimated in order to obtain a value for the efficiency. The iron losses are calculated from a FE-simulation at load conditions. Since the rotational speed is very low, the friction losses are also low. The value of 20 W is actually overestimated in comparison with measurements on an available prototype, described in Appendix C. The efficiency of the converter is defined as 98 %. The efficiency of the drive (converter+motor) is then approximately 80 %.

4.3.2 Comparison

Figure 4.11 shows the proposed direct-drive mixer and the geared mixer at approximately the same scale. As can be seen, the direct-drive mixer has a volume that is slightly bigger than the geared mixer. The estimated weight of the whole machine exceed the specified limit by 50 %. However, the size and weight of the non-active components, such as the housing and seals, have not been optimized and therefore, could most probably be decreased.

Table 4.6: Characteristics and performance of the final motor design.

Active component	Weight [kg]	Cost [Euro]
ferrite magnets	12.8	70.4 (27 %)
stator iron	22.6	37.4 (14 %)
rotor iron	44.4	73 (27 %)
conductors	26.9	83 (31 %)
total	106.6	264
Torque		
total torque	850 Nm	
reluctance torque	35 Nm	
cogging torque	0.6 %	
torque ripple	3.7 %	
Losses [W]		
stator iron	55	
rotor iron	5.5	
copper	690	
friction losses	20	
converter losses	105	
efficiency	80 %	
motor's power factor	0.9	

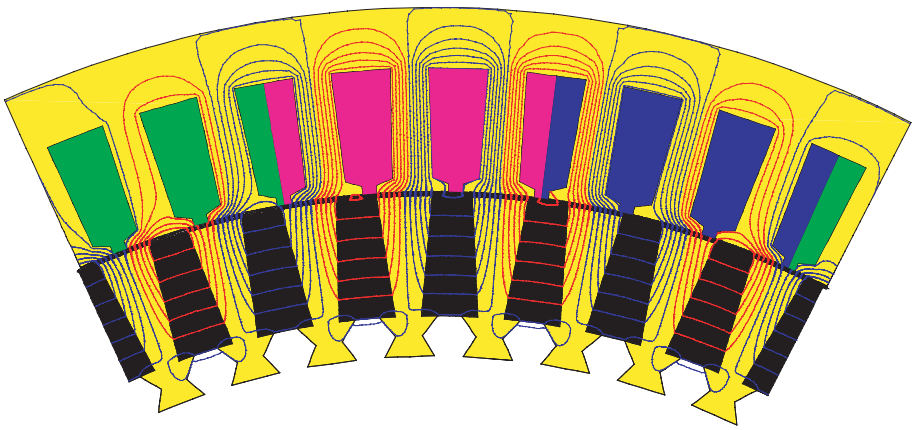

Figure 4.12: Final design of a PMSM with ferrite magnets with the flux lines at open-circuit conditions.

Hallberg estimated in [31] the cost to manufacture the considered motor, giving a range of possible prices for each component. The results presented below are the average values of the estimated costs for each component, for the prices in 2005. The propeller being the same for both mixers, it is not included in the total costs of the mixers. Figure 4.13.a shows that the cost of the direct-drive mixer exceeds the geared mixer cost by 50 %. This higher cost is due to several reasons:

- Size of the non-active components - The shaft, seals, bearings, and housing are larger and thus more costly since the PM motor has a large diameter. Figure 4.13.b shows the relative cost of each component of the direct-drive mixer without propeller. As can be seen, the seals, fixing plates and stator housing, which are components specific to the submersed application, represent almost half of the cost. The PM motor without its housing is then only approximately one third of the total cost.
- Converter - Unlike the induction motor of the geared drive, the PM motor needs a variable frequency converter in order to be able to start. The variable frequency converter is estimated to 10 % of the cost of the direct drive (Figure 4.13.b).
- Stator core - As can be seen in Figure 4.13.c, which shows the relative cost for the manufacturing of the PM motor's active components, the stator core

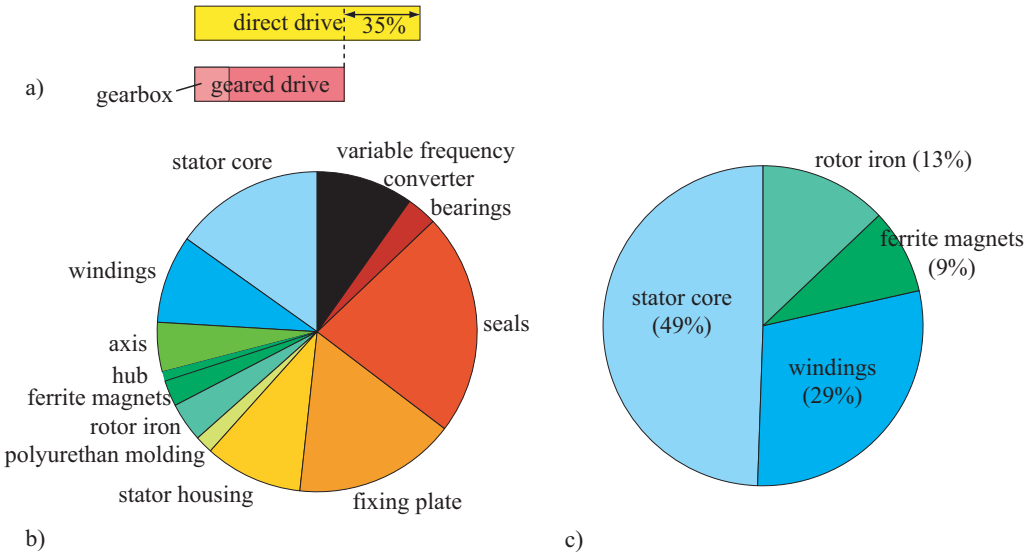

Figure 4.13: a) Costs of the direct and geared drives (without propeller);
b) Relative costs of the direct-drive mixer components without propeller;
c) Relative costs of the active components of the PM motor.

accounts for 49 % of the motor cost. The cost of the stator core manufacturing is much higher than the cost of the required iron material only, which is 14 % of the active material cost (Table 4.6). This is mostly due to the waste of iron during the manufacturing of the stator core.

- Stator windings - The stator windings represent 31 % of the cost of the motor's active components. The stator windings cost approximately 3 times the conductors material because they are considered hand-made [31]. Manufacturing aspects of the stator core and windings are further investigated in Chapter 5. Unexpectedly, the cost of the PMs is low, only 9 % of the total motor cost.

The direct-drive mixer costs more than the geared mixer. However, it has a better efficiency. The geared mixer's drive has an efficiency of 73 % against 80 % for the direct drive (Table 4.6). Figure 4.14 shows the initial and operating costs of both mixers in p.u. as a function of the number of years. The initial cost of the geared mixer is 1 p.u. The operating costs of the mixers are calculated for different electricity prices. An example of electricity price in Sweden for a medium-size industry is 0.53 öre/kWh without the taxes, which are 0.27 öre/kWh. The mixers are considered operating 50 weeks out of 52 in a year. As can be seen in Figure 4.14, the pay-off time of the direct-drive mixer is in this case approximately 3 years.

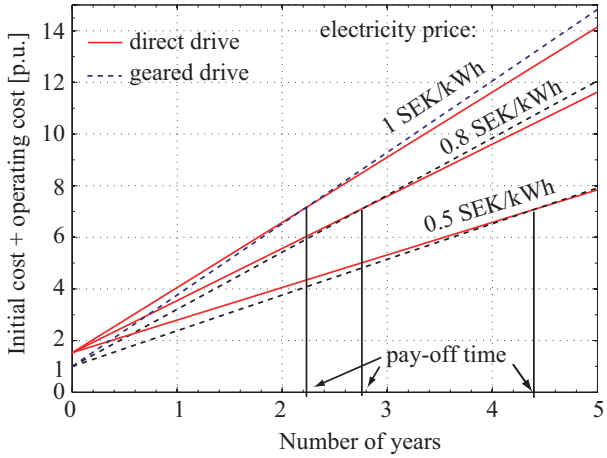

Figure 4.14: Initial and operating costs of the direct-drive and geared mixer.

4.4 Conclusions

The proposed direct-drive mixer is larger and heavier than the geared mixer and has a higher initial cost. Although the efficiency is higher, leading to a lower operating cost, convincing the customers to buy the direct-drive mixer may be a difficult task, especially since the geared mixer has a lifetime of 5 years and the pay-off time is already 3 years. Therefore, no prototype motor has been built and the project of the direct-drive mixer was put on hold.

A prototype motor would have been required to confirm the study. In particular, many questions remain concerning the manufacturing of the rotor and the cost of the direct drive. The designs were based on the assumption of a winding temperature equal to 80 °C, which could have been verified with a prototype. Furthermore, the influence of the temperature dependency of the magnet remanence flux density on the motor's performance could have been more deeply investigated. The FE-simulations could have been validated as well. The construction and evaluation of the prototype may have confirmed, or not, the decision of freezing the project.

The Ph.D. project went further on by evaluating another prototype with non-overlapping concentrated windings built by Danaher Motion. This prototype is described in Appendix C. Several questions are investigated with this prototype. One issue, revealed by the study on the direct-drive mixer, concerns the manufacturing of the stator for PMSM with concentrated windings, which was not as easy and inexpensive as expected. This issue is investigated in the next chapter.

5 Manufacturing methods of stator cores with concentrated windings

The investigations on the direct-drive mixer showed that the manufacturing of a stator with concentrated windings may not be as easy and inexpensive as expected. Therefore, the purpose of this chapter is to investigate the difficulties in manufacturing a stator core with concentrated windings. Existing solutions are compared in terms of cost, required equipment for the production and performance of the motor.

The presented methods are illustrated using the example of the prototype motor described in Appendix C and shown in Figure 5.1. This motor has an outer rotor and external diameter of 400 mm. The active weight of the stator iron is approximately 4 kg.

The production methods of the stator cores are first investigated followed by the methods to produce and assemble the coils.

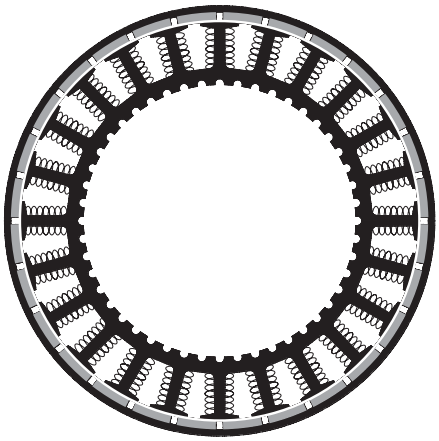

Figure 5.1: Geometry of the investigated outer-rotor PM motor.

5.1 Production methods of the laminated stator cores

First, different methods to manufacture the stator core are investigated. However, it should be considered that the selection of the method to wind the coils is related to the selected production method of the stator core.

5.1.1 Complete core

With this method, the entire section of the core is punched in one piece as shown in Figure 5.2.a. It is the conventional way to manufacture the laminations for machines up to a few 100 kW. If the machine does not have a laminated rotor or it has an inner stator as in the example of Figure 5.1, the centrepiece left after punching is not useful. Therefore, the quantity of wasted iron material can be large, approximately 80 to 90% of the total purchased iron material. In addition, for a stator with a large number of teeth, the required force for punching is considerable [31]. Single tooth punching is then an appropriate solution. It requires more time but has the advantage that a smaller press machine can be used. It could be possible to use the wasted material inside the ring for motors with smaller diameters, however causing some logistic problems for the motor manufacturer.

For the prototype PM motor in Figure 5.1, an iron sheet with the dimensions of 400×400 mm is required. The area of the stator core is only 18 % of the original iron sheet area. Out of the 22 kg of purchased iron, only 4 kg are used for the stator. With this method, the manufacturing technique and the machine tools are conventional, but the cost for the iron material is high due to the large amount of waste.

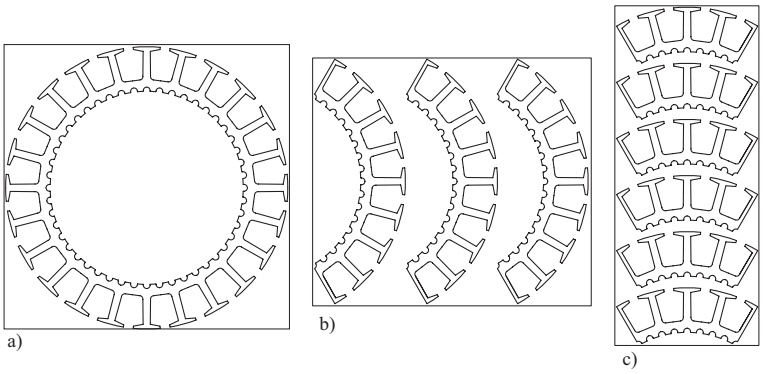

Figure 5.2: Stator laminations: a) Entire section is punched; b) 120° segments; c) 60° segments.

Instead of punching the laminations, which can be difficult if the diameter of the stator is large, the laminations can be laser-cut. However, this method is reserved for the construction of prototypes, because of its high cost and the impossibility to produce high volumes in a short time. The laser is indeed moving slowly, approximately 40 m/min and even slower if there are some sharp angles in the geometry [31]. Furthermore, laser cutting may cause more losses in the iron [104].

+: Conventional manufacturing technique.
−: High cost of iron material due to the large amount of waste.

5.1.2 Segmented core

With this method, the stator iron is split into segments as shown in Figure 5.2.b and Figure 5.2.c. As a consequence, the material cost can be decreased and the productivity improved. With segments of 120°, there is 50 to 60 % of iron waste [31], which is much less than for the previous described method. After layering, the segments are welded together.

For the prototype motor, the amount of wasted iron with three segments of 120° is 12.8 kg, which is approximately 30 % less compared to the case when the complete core section is punched at once. If the stator is divided in 6 segments of 60° (Figure 5.2.c), the amount of wasted iron is 9.2 kg, which is a reduction by 48 %.

The manufacturing of stators with segmented laminations is conventional, but the amount of wasted material is still high, although it is much reduced compared to the method when the whole section of the stator is punched. Finally, the segments need to be welded together, which increases the cost and production time. The welding can as well damage locally the magnetic properties and lead to extra losses in the iron [104].

+: Conventional manufacturing technique.
−: High cost of iron material due to the waste. Welding of the segments.

5.1.3 Spiral-laminated core

With this method, the core is manufactured from a long iron band. The slots are progressively punched in the band. The band is then rolled up in a spiral and welded together (Figure 5.3). The un-welded core resembles a slinky and is often called a "slinky" for that reason. This method allows to significantly reduce the material waste. The iron waste is estimated to be 30 to 40 % of the iron that is necessary when punching the entire section of the stator in a square sheet [31]. Different tech-

niques for rolling up the iron band are patented, [105–108]. The thickness of the stator yoke is a limiting factor for the application of this method. If the yoke is too thick (in order to avoid magnetic saturation or to guarantee the rigidity of the stator), the iron band cannot be rolled up. This limits the stator geometries that can be produced as a "slinky". The rolling process may also negatively influence the magnetic properties of the iron, leading to higher iron losses. Some motor manufacturers produce stators with this method for stator diameters up to 400 mm. It should then be possible to manufacture the example motor in Figure 5.1 with this method, the stator yoke being reasonably thick. The amount of wasted iron would be 7.8 kg, which is a significant reduction by 56 % compared to the method where the whole stator section is punched at once.

This method minimizes the amount of wasted iron, however, it requires special manufacturing techniques and production machines. In addition, not all the geometries can be produced this way.

+: Low quantity of waste.
−: Requires special manufacturing techniques and special production machines. Not all the geometries can be produced.

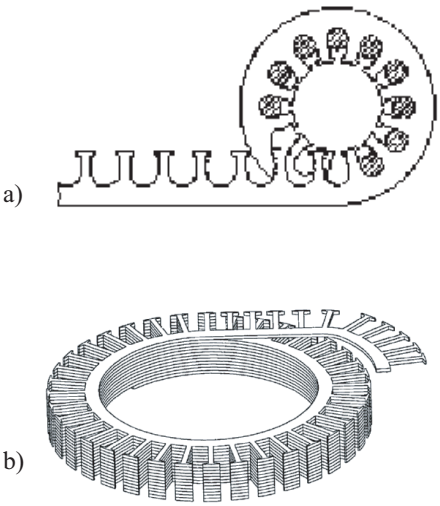

Figure 5.3: Examples of spiral-laminated stator cores: a) Outer stator from Mitsuhiro [107]; b) Inner stator from Lee [108].

5.1.4 Join-lapped core

Figure 5.4 shows a model of a joint-lapped core presented in [109]. With this method, the segments are connected together with some cylindrical convex or concave joints that allow the rotation of the segments. Many patents exist for similar methods. They describe different ways to connect the segments together, such as with joints or elastics [110, 111]. As for the method with spiral-laminated stator cores, the amount of wasted iron material is minimized. This manufacturing technique is not conventional and requires special tools.

+: Low quantity of waste.
−: Require special manufacturing techniques, especially for the joints.

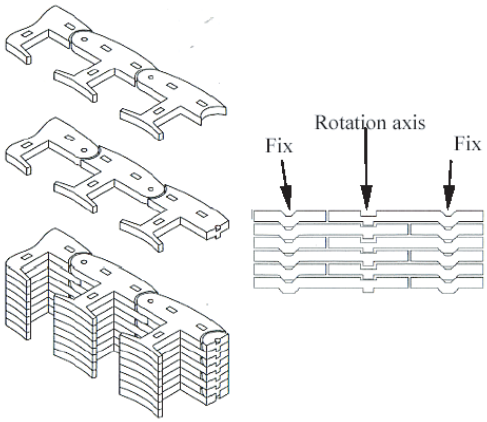

Figure 5.4: Akita's model of a joint-lapped core [109].

5.2 Production and assembly of the coils

With a laminated core, in one piece or segmented, the coils can be wound around the teeth using a special winding-machine equipped with a needle. If the laminated core has an adapted geometry, the coils can also be pre-wound before their assembly in the core.

5.2.1 Needle-wound coils

Non-overlapping windings can be automatically wound with a needle-winding machine. The coils are directly wound around the core by a needle. The drawback of this technique is the large space that is required between two neighboring coils in order to allow the needle to move, as shown in Figure 5.5. The space between two coils should be at least 3.5 to 4 times the wire diameter [31]. This results in a low slot fill factor. The designer should therefore consider higher copper losses or a better cooling system. Figure 5.5 shows two coils of the investigated prototype motor that are wound with a needle winder. The slot fill factor is approximately 0.4. With needle-wound coils, conventional manufacturing techniques can be used for the lamination and the production of the coils can be automated. However, the investment in a needle winder is necessary.

+: Conventional manufacturing technique for the lamination. Automatized production of the coils.
−: Low fill factor. Requires the investment of a needle winder.

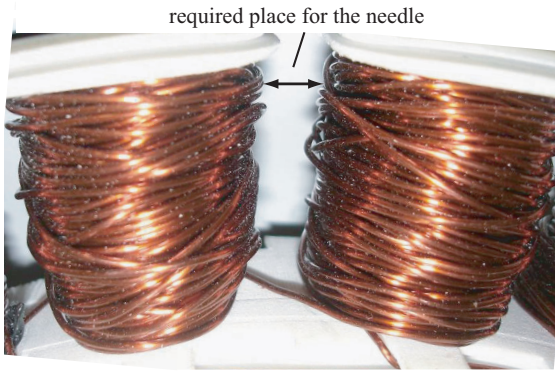

Figure 5.5: Two needle-wound coils of the outer-rotor prototype motor.

Figure 5.6 shows how a needle winder easily can wind the coils for a joint-lapped core [109], allowing a high slot fill factor. This manufacturing method requires special laminations and the investment of a winding-machine specific for this kind of lamination and windings.

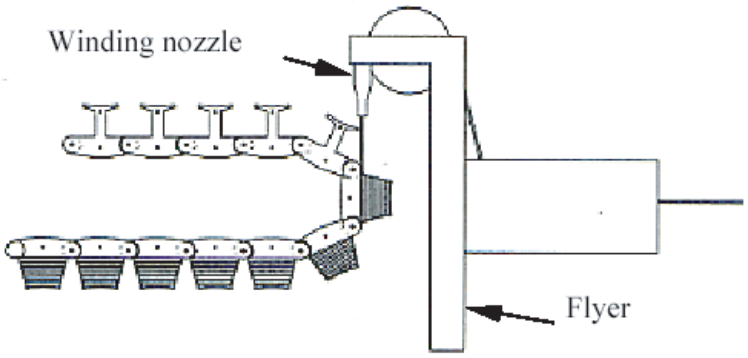

Figure 5.6: Winding the coils of a joint-lapped core from Akita, [109].

5.2.2 Manually-wound coils

A high slot fill factor can be achieved with any core geometry if the coils are manually wound around the teeth. The obvious inconvenient is the very slow and costly production.

+: Conventional manufacturing technique of the lamination. High fill factor.
−: Very costly, slow.

5.2.3 Pre-wound coils

The coils are wound before setting them into the stator core. The same method is used to wind the coils of a conventional distributed winding. However, the stator lamination profiles need to be adapted in order to guarantee a high slot fill factor and short end-windings. Different possibilities for the stator are discussed below.

Stator with single-tooth segments

A first solution for pre-wound coils is to use laminations that are segmented in a way to facilitate the insertion of the coils to their position in the teeth. Mecrow proposes in [112] a construction according to Figure 5.7, where the pre-wound coil can easily be passed along the core back and glided around the tooth. This method allows to achieve a high slot fill factor. The iron wasted during the punching of the lamination is minimized with this method, as seen previously. However, with a stator having many teeth, the time to assemble and weld the stator is increased.

Furthermore, with many teeth, the welding at each tooth causes higher losses and the possibility of leakage is higher if some segments are not well fitted together.

+: Easy to place the pre-wound coils in the core. High achievable fill factor.
−: Airgap between the segments. Welding. Not convenient with high number of teeth.

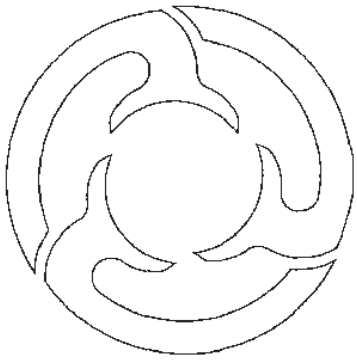

Figure 5.7: Mecrow's segmented lamination for easy insertion of pre-wound coils [112].

Stator in SMC

The high cost for the iron laminations caused by the quantity of wasted material can make SMC material a good solution to decrease the price of the motor. SMC material has the drawback of poorer magnetizing curves compared to conventional iron lamination but the production of SMC parts is easier and cheaper for high number of parts. SMC is also well adapted for concentrated windings as the teeth and stator yoke can be produced separately [95]. The coils are first placed around the teeth, which are then assembled to the stator yoke (Figure 5.8). The isotropic magnetic properties of the SMC allow round-shaped teeth that enable a high slot fill factor.

The solution of a stator in SMC may be of interest for the investigated prototype motor with needle-wound coils in order to minimize its manufacturing cost. 3D-FE simulations are performed to compare the performance of the motors with laminated and SMC stators. Both motors have identical rotors. For the stator in SMC, the tooth bodies have a rectangular cross-section and are axially shorter than the rotor. The SMC yoke and the tooth tips are as long as the rotor. Since ferrite magnets are used, the open-circuit airgap flux density is low, approximately 0.4 T. Thus, it is not decreased considerably with the stator in SMC. At nominal load, a 3D-FE simulation shows that the torque is decreased by 20 % compared to the laminated

motor, for the same current (Table 5.1). The torque reduction with the SMC stator can be partly compensated, since the slot fill factor can easily be increased. The fill factor of the laminated motor with needle-wound coils is 0.4. With SMC, the slot fill factor can be increased to 0.6 [95], allowing larger conductor diameters. The characteristics of the investigated motors are given in Table 5.1. For the improved SMC motor ("SMC2"), the phase resistance is decreased by 33 %, which allows to increase the current by 22 %, keeping the copper losses identical. With the new winding and increased current, the torque is 6 % lower than the torque of the motor with laminated stator. Iron losses were not investigated but are expected to be higher with the SMC stator, according to [95]. The geometry of the SMC stator could also be improved by better utilizing the isotropic magnetic properties of the material. The slot fill factor could also be increased further using special techniques. In [79], the coils are made up of rectangular conductors. The obtained slot fill factor is 0.74. In [95], the slot fill factor rises from 0.64 to 0.78 after pressing the coils as in Figure 5.8. For the prototype motor, where the flux densities in the machine are low, a stator in SMC could be an option to decrease the production cost, at similar performance, with an adapted design.

+: Cheap production, high fill factor achievable.
−: Poor magnetic properties of SMC (compared to iron lamination).

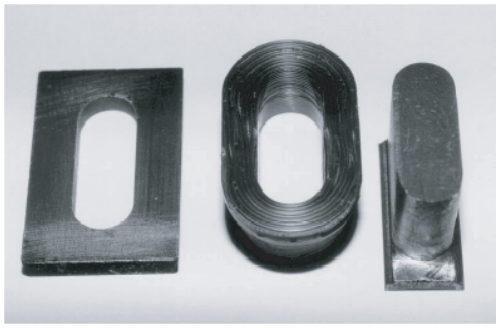

Figure 5.8: Part of stator yoke, pre-pressed coil, and tooth in SMC from Jack [95].

Table 5.1: Performance of the motors with laminated and SMC stators.

Stator	Laminated	SMC	SMC2
Open-circuit airgap flux density [T]	0.425	0.41	0.41
Slot fill factor	0.4	0.4	0.6
Copper losses	Identical		
Current [p.u.]	1	1	1.22
Torque [p.u.]	1	0.8	0.94
Iron losses [W]	40	Higher	Higher
Material cost	Higher	Lower	Lower

Stator with special tooth tips

A method using a special geometry of the tooth tips is described in Yamada's patent [113] and Figure 5.9. In a first stage, the pre-wound coils are easily placed around the teeth, the tooth tips being vertically aligned with the tooth body. A tool is then used to bend the tooth tips to their normal position. This method requires a large distortion of the tooth tips, which may cause some extra iron losses in the deformed parts. With this method, it is possible to have joint-lapped cores, which is more appropriate than welding the segments together, especially when the stator has many teeth. A high slot fill factor can be achieved. However, it requires special manufacturing techniques that are patented.

+: High achievable fill factor.
−: Requires a special manufacturing technique. Distortion of the tooth tips. Patented.

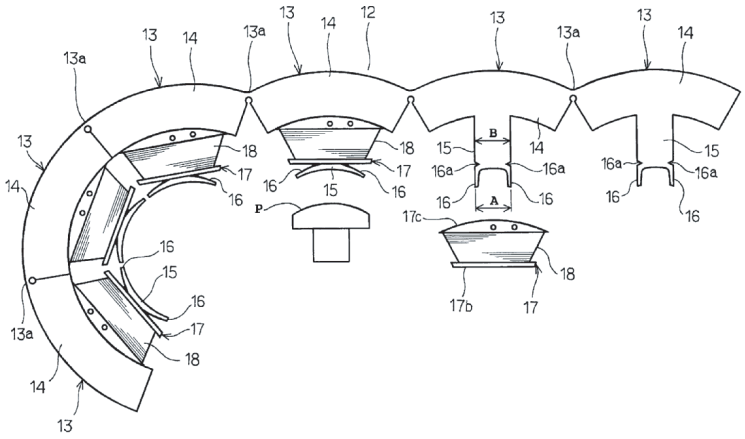

Figure 5.9: Yamada's patent [113].

Stator with open slots

When the stator slots are fully open, i.e. the teeth have no tips, it is possible to place pre-wound coils in the stator core even if it is not segmented. However, the drawbacks of this method are the lower open-circuit airgap flux density and the possibly higher torque ripple. The coils have also to be fixed to the stator core in some way. 2D-FE simulations are performed on the 28-pole prototype PM motor to check if it is advantageous having open slots to facilitate the mounting of the coils. The original motor with semi-closed slots is compared to a motor with open slots, the rotor being identical. Figure 5.10 shows the geometries of the two slots.

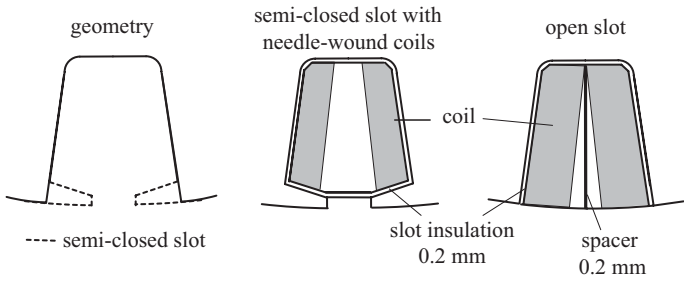

Figure 5.10: Comparison of the coils with a semi-closed and open slot.

At first, both motors have the same number of conductors, the same slot fill factor and the same copper losses. FE simulations show that changing from a semi-closed to an open slot geometry reduces the fundamental of the open-circuit airgap flux density by 34 % and reduces the torque at load by 31 % for the prototype motor. The tooth width of the stator with open slots was then increased to obtain the same slot area as the semi-closed slot stator. With larger teeth, the torque is reduced by 26 % compared to the semi-closed slot stator. As shown in Figure 5.10, the slot fill factor can be increased, from 0.4 to 0.6 with open slots. Keeping the copper losses constant, the current can thus be increased by 22 %. With this higher current, the torque of the open-slot motor is still 8 % lower than the torque of the motor with semi-closed slots and a lower slot fill factor.

Opening the slots changes other characteristics of the motor, as can be seen in Table 5.2. The absence of tooth tips influences the cogging torque and thus the torque ripple. For the simulated motors, the torque ripple is 3.4 % of the mean torque for a motor with semi-closed slots and higher with 4.9 % for a motor with open slots. Furthermore, with open slots, there is less iron in the stator and therefore lower iron losses. As can be seen in Table 5.2, the iron losses at nominal speed are more than halved when the slots are opened (the iron losses of the PMSM with semi-closed slots are chosen as a reference and set to 1 p.u.). Finally, opening the slots worsen the flux-weakening capability of the PMSM as the d-axis inductance drops consequently.

In the case of the investigated motor, open slots are not advantageous because of the significant decrease in the torque and in the inductance. Moreover, since the supplied current has an higher amplitude, a converter with a higher rating may be required, which may be a serious drawback. However, for other motors and applications, the advantages of the easy assembly, the high slot fill factor, and the possibly lower iron losses may overcome the drawbacks.

+: Conventional manufacturing techniques of the lamination and the coils. High fill factor achievable. Possibly lower iron losses.
−: Requires to fix the coils. Higher flux leakage due to the lack of tooth tips.

Table 5.2: Performance of the motors with semi-closed and open slots.

Slot	Semi-closed	Open	Open
Slot area	Identical		
Open-circuit airgap flux density [T]	0.425	0.294	0.294
Slot fill factor	0.4	0.4	0.6
Copper losses	Identical		
Current [p.u.]	1	1	1.22
Nominal torque [p.u.]	1	0.74	0.92
Torque ripple [%]	3.4	5.0	4.9
Stator iron losses [p.u.][1]	1	0.39	0.43
d-axis inductance [p.u.][2]	1	0.48	0.52

[1]The iron losses from the semi-closed PMSM are chosen as a reference and set to 1 p.u.
[2]The inductance from the semi-closed PMSM is chosen as a reference and set to 1 p.u.

5.3 Conclusions

There are several methods to manufacture a stator with non-overlapping windings. The choice of the manufacturing technique can be influenced by the followings:

- Cost of the stator - The amount of wasted iron material can make the stator core very expensive. It is an issue especially when the entire motor's cross-section is punched.
- Stator size - If the stator yoke is large or there are many teeth, some techniques are not possible, such as the slinky or the segmented stator that allows easy fitting of pre-wound coils.
- Rapidity of production - The production time influences the cost. It is an important issue when the coils are manually wound or when the stator core is divided in many segments.
- Achievable fill factor - With a high fill factor, the copper losses or the constraints on the cooling system can be decreased. With needle windings and a conventional lamination, the fill factor is very poor.
- Investment in new manufacturing equipment - New manufacturing equipment is possibly required for producing slinkies or winding coils with a needle-winder.

5.4 Summary

Different manufacturing methods of stator cores with concentrated windings have been investigated. When punching the stator core laminations in one piece, the amount of wasted iron material is substantial causing a high material cost. The waste can be decreased using a segmented stator core or a spiral-laminated core. However, the investment in special production equipment is required for these methods. The coils can be wound automatically with a needle winder. In general, this implies a low slot fill factor. Using pre-wound coils allows a higher slot fill factor. It is possible with single-tooth segments, stators in SMC, special tooth tips, and stators with open slots. It was shown that in the cases with SMC and open-slot stators, the performance of the motors could be improved by taking the specificities of the manufacturing methods into account during the design process. The production costs should be considered from case to case, as high equipment investments are required for certain methods.

In the next chapters, the measurements performed on the prototype motor are presented.

6 Inductances

This chapter is composed of two parts. In the first part, it is shown that *dq* theory can be applied to a PMSM with concentrated windings although the MMF space distribution of such machines is far from sinusoidal. In the second part, inductance measurements on the prototype motor described in Appendix C are presented and analyzed.

6.1 dq theory applied to a PMSM with concentrated windings

In this section, *dq* theory is applied to the prototype motor with surface-mounted PMs and double-layer concentrated windings. Although the assumption of sine-distributed windings is violated, it is shown with theory and measurements, that the *dq* model is reliable for torque and voltage calculations of the loaded machine.

6.1.1 Literature study

The *dq* theory is widely used to model and analyze PMSMs since it simplifies greatly the models and equations of those machines. When performing the Park transformation, some assumptions should be fulfilled in order to get reliable models: The windings should be sine-distributed and the magnetic circuit should not saturate [114]. In the case of surface-mounted PMSMs with non-overlapping concentrated windings, the assumption of sine-distributed windings is violated. It is therefore commonly not recommended to use the Park transformation for these machines [80, 114].

In this chapter, the implications of the assumptions of sinusoidal distribution of the windings are first mentioned. The validity of these implications is checked in the case of the 28-pole, 24-slot prototype motor. The dependency of the inductance on the rotor position due to variation of magnetic permeance and the harmonic content of the back-EMF are investigated. Finally, measurements are used to validate the *dq* model and phasor diagram of the motor.

6.1.2 dq theory and Park transformation

Models of a PMSM

A PMSM can be modelled with equations similar to the ones used for synchronous machines [115]. The PM creates a MMF $H_m l_m$, H_m being the coercive magnetic field intensity and l_m the PM thickness (Figure 6.1). It is then equivalent to a winding carrying a current $i_f = H_m l_m$ and having a self-inductance $\mathcal{L}_f$ and mutual inductances $\mathcal{M}_{af}$, $\mathcal{M}_{bf}$, $\mathcal{M}_{cf}$. When the magnetic circuit is linear, the fluxes ψ seen by the different windings are linked to the currents i with

$$\underbrace{\begin{pmatrix} \psi_a \\ \psi_b \\ \psi_c \\ \psi_f \end{pmatrix}}_{\psi_{abc}} = \underbrace{\begin{pmatrix} \mathcal{L}_a(\theta) & \mathcal{M}_{ab}(\theta) & \mathcal{M}_{ac}(\theta) & \mathcal{M}_{af}(\theta) \\ \mathcal{M}_{ab}(\theta) & \mathcal{L}_b(\theta) & \mathcal{M}_{bc}(\theta) & \mathcal{M}_{bf}(\theta) \\ \mathcal{M}_{ac}(\theta) & \mathcal{M}_{bc}(\theta) & \mathcal{L}_c(\theta) & \mathcal{M}_{cf}(\theta) \\ \mathcal{M}_{af}(\theta) & \mathcal{M}_{bf}(\theta) & \mathcal{M}_{cf}(\theta) & \mathcal{L}_f(\theta) \end{pmatrix}}_{\mathcal{L}_{abc}} \underbrace{\begin{pmatrix} i_a \\ i_b \\ i_c \\ i_f \end{pmatrix}}_{I_{abc}}. \tag{6.1}$$

The self-inductances $\mathcal{L}$ and mutual inductances $\mathcal{M}$ are functions of the rotor position θ in the general case. The subscripts a, b, and c refer to the three phases of the windings. The subscripts f refers to the PM.

If there is only a current i_a in phase a and the PMs, the flux seen by phase a is deduced from equation (6.1) as

$$\psi_a = \mathcal{L}_a i_a + \mathcal{M}_{af} i_f = \mathcal{L}_a i_a + \psi_m \tag{6.2}$$

where ψ_m is the PM flux linkage.

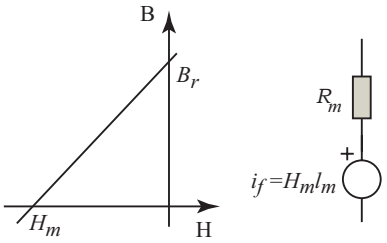

Figure 6.1: Magnetic properties and equivalent circuit of a PM.

Park transformation

The Park transformation allows substituting a three phase windings a, b, c placed in the stator to two windings d and q with their magnetic axes rotating synchronously with the rotor. The Park transformation for the synchronous machine [115] is adapted to the PMSM. The homopolar components are disregarded. The transformation matrixes B and B^{-1} are:

$$B = \frac{2}{3}\begin{pmatrix} \cos\theta & \cos(\theta - \frac{2\pi}{3}) & \cos(\theta - \frac{4\pi}{3}) & 0 \\ -\sin\theta & -\sin(\theta - \frac{2\pi}{3}) & -\sin(\theta - \frac{4\pi}{3}) & 0 \\ 0 & 0 & 0 & \frac{3}{2} \end{pmatrix} \tag{6.3}$$

$$B^{-1} = \begin{pmatrix} \cos\theta & -\sin\theta & 0 \\ \cos(\theta - \frac{2\pi}{3}) & -\sin(\theta - \frac{2\pi}{3}) & 0 \\ \cos(\theta - \frac{4\pi}{3}) & -\sin(\theta - \frac{4\pi}{3}) & 0 \\ 0 & 0 & 1 \end{pmatrix}. \tag{6.4}$$

The dq currents and fluxes are calculated with equations (6.5) and (6.6) respectively.

$$I_{dq} = BI_{abc} \tag{6.5}$$

$$\Psi_{dq} = B\Psi_{abc} = BL_{abc}B^{-1}I_{dq} \tag{6.6}$$

dq fluxes and currents are then linked by equation (6.7). Each component of the inductance matrix may depend on the position θ.

$$\underbrace{\begin{pmatrix} \psi_d \\ \psi_q \\ \psi_f \end{pmatrix}}_{\Psi_{dq}} = \begin{pmatrix} \mathcal{L}_d(\theta) & \mathcal{M}_{dq}(\theta) & \mathcal{M}_{df}(\theta) \\ \mathcal{M}_{dq}(\theta) & \mathcal{L}_q(\theta) & \mathcal{M}_{qf}(\theta) \\ \mathcal{M}_{df}(\theta) & \mathcal{M}_{qf}(\theta) & \mathcal{L}_f(\theta) \end{pmatrix} \underbrace{\begin{pmatrix} i_d \\ i_q \\ i_f \end{pmatrix}}_{I_{dq}} \tag{6.7}$$

Case of sine-distributed stator windings

The assumption of sinusoidal spatial distribution of the windings implies that:

1 The phase MMF created by a current i_a is a sinusoidal function of the position. Therefore, all its spatial harmonics are equal to zero.

2 The self-inductances and mutual inductances of the stator phases are independent of the rotor position in case of non-salient rotors (equation (6.8)) or vary with position with a second order harmonic in case of salient rotors (equation (6.9)).

$$\mathcal{L}_a(\theta) = L_a = L_b = L_c \tag{6.8}$$

$$\begin{aligned}\mathcal{L}_a(\theta) &= L_a + L_{a2}\cos 2\theta \\ \mathcal{L}_b(\theta) &= L_a + L_{a2}\cos(2\theta - 2\pi/3) \\ \mathcal{L}_c(\theta) &= L_a + L_{a2}\cos(2\theta - 4\pi/3)\end{aligned} \tag{6.9}$$

Taking into account this second implication when transforming to dq axes, it can be shown that the d- and q-axes inductances are independent of the position ($\mathcal{L}_d(\theta) = L_d, \mathcal{L}_q(\theta) = L_q$) and the cross-coupling inductance is equal to zero ($\mathcal{M}_{dq}(\theta) = 0$).

3 The flux created by the PMs seen by a phase winding is a sinusoidal function of the position (equation (6.10)). The back-EMF is then also a sinusoidal function of the position.

$$\begin{aligned}\mathcal{M}_{af}(\theta) &= M_{af}\cos\theta \\ \mathcal{M}_{bf}(\theta) &= M_{af}\cos(\theta - 2\pi/3) \\ \mathcal{M}_{cf}(\theta) &= M_{af}\cos(\theta - 4\pi/3)\end{aligned} \tag{6.10}$$

These implications are further discussed in [115] in the case of a synchronous machine. In the case of sinusoidal spatial distribution of the stator windings, the equations in dq axes are simplified from equation (6.7) to:

$$\begin{pmatrix} \psi_d \\ \psi_q \\ \psi_f \end{pmatrix} \begin{pmatrix} L_d & 0 & M_{af} \\ 0 & L_q & 0 \\ 3/2.M_{af} & 0 & 3/2.L_f \end{pmatrix} \begin{pmatrix} i_d \\ i_q \\ i_f \end{pmatrix}. \tag{6.11}$$

The d- and q-axes are not coupled and there is no dependency on the rotor position, which makes the Park transformation attractive. Moreover, the torque equations (6.13) or (6.14) in dq axes can be retrieved from the derivative of the magnetic energy W (equation (6.12)), in the case of a linear magnetic circuit.

$$T = \frac{\partial W}{\partial \theta} = -\frac{1}{2}\frac{\partial}{\partial \theta}\left({I_{abc}}^t \Psi_{abc}\right) = -\frac{1}{2}\left(B^{-1} I_{dq}\right)^t \frac{\partial L_{abc}}{\partial \theta} B^{-1} I_{dq} \tag{6.12}$$

For a salient motor:

$$T = \frac{3}{2}\frac{p}{2}\left(\Psi_m I_q + (L_d - L_q) I_d I_q\right) \tag{6.13}$$

For a non-salient rotor:

$$T = \frac{3}{2}\frac{p}{2}\Psi_m I_q \tag{6.14}$$

In the following sections, the case of non-overlapping concentrated windings is investigated.

6.1.3 MMF and inductances of non-overlapping concentrated windings

MMF

The spatial distribution of the armature reaction MMF in the airgap of PMSMs with non-overlapping concentrated windings is far from sinusoidal. As shown in Chapter 3, the MMF can contain sub-harmonic components that have sometimes higher amplitude than the synchronously rotating harmonic component, depending on the number of winding layers and on the number of slots per pole per phase. Therefore it is not possible to consider that the MMF from a non-overlapping concentrated-winding is sinusoidal. However, this does not prevent equations (6.11) and (6.14) to be fulfilled, as shown in the next sections.

Inductances

The self and mutual inductances can be obtained from the armature reaction flux that links a phase winding [116]. When the rotor is rotating, the armature reaction flux density is varying with the change of permeance in the magnetic circuit. This variation of permeance is reflected in the flux seen by a phase winding and thus in the inductance.

The inductance can be decomposed in different harmonic components. An inductance harmonic component of order h is proportional to the squared winding factor of order h over h. PMSM with non-overlapping concentrated windings have high self-inductance due to the presence of many harmonic components [80]. The large harmonic content in the inductance could suggest a large variation of the inductance as a function of the rotor position. However, the variation of permeance in the airgap is also one of the reasons for the cogging torque. PMSMs with non-overlapping concentrated windings are well-known for their low cogging torque if the combination of slots and poles is well chosen [61]. This last argument is in favor for a low variation of the inductance with the position, when the magnetic circuit is linear.

The dependency on the rotor position of the inductance is evaluated using FE-methods for the investigated prototype motor. Its cogging torque is approximately 3 %. The airgap flux density of the motor created by the armature reaction only is shown in Figure 6.2. It has a large sub-harmonic component due to the fact that the number of slots is lower than the number of poles. Figure 6.3.a shows the FE-simulated phase self-inductances as a function of the rotor position, for different slot opening widths. The magnetic circuit is linear. As expected for a surface-mounted PMSM, the inductance variation is very small, lower than 0.15 % and depends on

the value of the slot opening width. The slot opening width is varied from 24 to 56 % of the slot width. Due to the non sine-distributed windings, the inductance varies with the position with harmonics of orders higher than 2.

However, the influence of the position on the inductance in the *dq* model is negligible. With self- and mutual-inductances depending on the position as shown in Figure 6.3.a, the ripple in the *d*- and *q*-axes inductances calculated with the Park transformation is lower than 0.05 % and the cross-coupling inductances are close to zero. The ripple in the torque calculated from the *dq* model (equation (6.12)) is 1.4 %. The torque mean value when having constant *d*- and *q*-axes inductances is 0.2 % different to the torque when the inductances are considered position dependent.

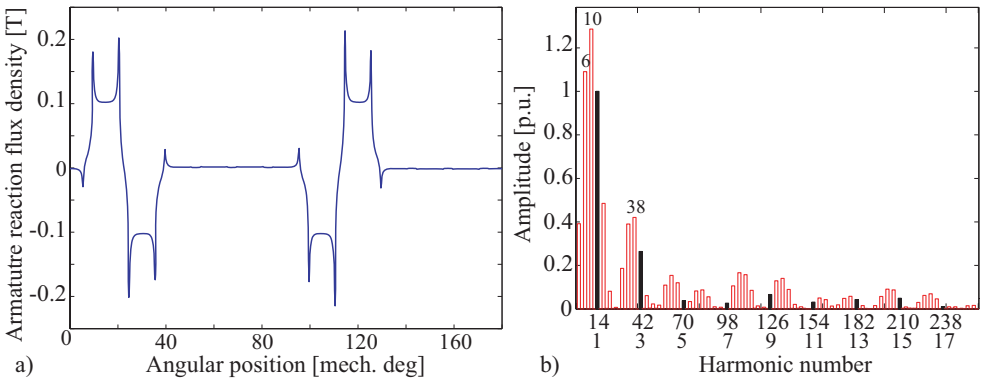

Figure 6.2: a) Armature reaction airgap flux density; b) Its spectrum.

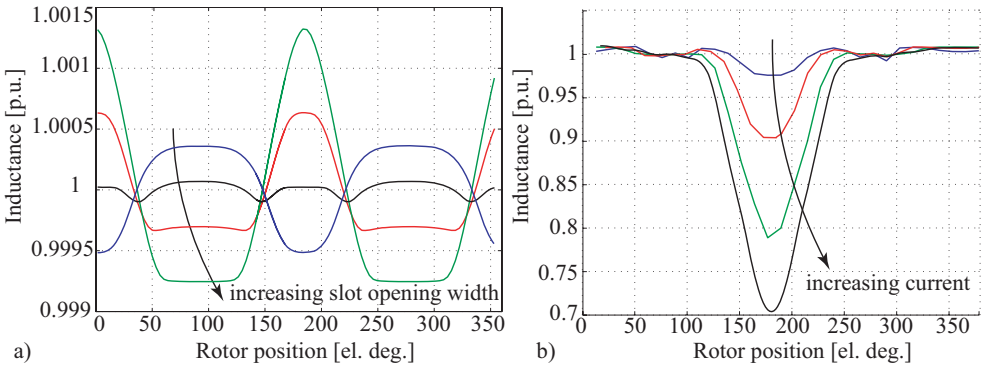

Figure 6.3: Inductance as a function of the rotor position: a) With a linear magnetic circuit; b) With a non-linear magnetic circuit.

When the magnetic circuit is non-linear, the variation of the inductance as a function of the rotor position cannot be neglected, as illustrated in Figure 6.3.b. One phase of the motor is supplied with a constant current while the rotor is rotating. Four FE-simulations are performed with different amplitudes of the constant current. As can be seen in Figure 6.3.b, the inductance drops largely, when the rotor is positioned at 180°, i.e. when the PM flux is added to the armature reaction flux which saturates the iron.

However, saturation effects are not specific to PMSMs with non-overlapping concentrated windings. Any PMSM with distributed windings can have a large variation of the inductance as a function of the position if the iron saturates. The solution to avoid this modelling problem is to define d- and q-axes inductances dependant on the d- and q-axes currents [114].

6.1.4 Harmonic content of back-EMF

The phase back-EMF is equal to the derivative with time of the flux linkage created by the PM. The amplitude of an harmonic in the flux-linkage is proportional to the product between the amplitudes of the harmonic in the open-circuit airgap flux density (Figure 6.4.b) and the harmonic of same order in the armature reaction flux density (Figure 6.2.b). Figure 6.4 shows the open-circuit airgap flux density of the 28-pole 24-slot motor and its spectrum. The flux density is analytically calculated with the models from [65] without taking into account the slot effects, whereas the FE simulations are performed with slots. Without the slot effects, the open-circuit airgap flux density has only harmonics of order 14, 42, 70, 98, etc. Multiplying these harmonics with the harmonics in the armature reaction flux density, the sub-harmonics, i.e. the harmonics of order 2, 6 and 10 and some other harmonics disappear in the flux linkage. The harmonic of order 14 corresponds to the fundamental in the back-EMF. The harmonic content of the back-EMF is better than the one of a motor with 2 slots per pole and per phase and the same PM width, as the 5^{th} and 7^{th} harmonics are lower (Figure 6.5). Taking into account the slots and zigzag leakage flux, the 9^{th}, 11^{th}, 13^{th}, and 15^{th} harmonics are attenuated, which gives a more sinusoidal back-EMF. In Figure 6.5, the back-EMF spectra derived from measurements, FE simulations and analytical calculations are presented.

The 3^{rd} harmonic of the back-EMF is large but it has no influence when transforming in the dq axes. The harmonics which have an order that is a multiple of 3 are also cancelled when applying the Park transformation [117].

Equation (6.10) is rewritten with a mutual inductance containing harmonics of orders 5^{th}, 7^{th}, 11^{th}, 13^{th}, and 15^{th} reflecting the harmonics in the measured back-EMF

as in Figure 6.5. The mutual inductances $\mathcal{M}_{df}$ and $\mathcal{M}_{qf}$ defined in equation (6.7) are then depending on the rotor position. Their ripple is approximately 2.4 %. This induces a 4 % ripple in the torque. The difference in the mean value of the torque when taking into account the harmonics in the back-EMF and neglecting them is 0.003 %, which is negligible. Therefore the back-EMF of the investigated motor can be considered sinusoidal when transforming to the dq model. Many other PMSM with non-overlapping concentrated windings have back-EMF that are close to a sinusoidal function.

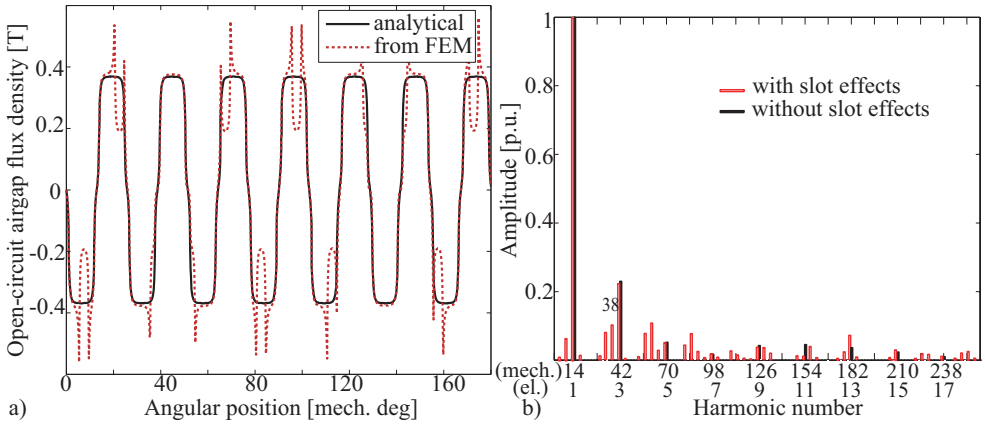

Figure 6.4: a) Open-circuit airgap flux density; b) Its spectrum.

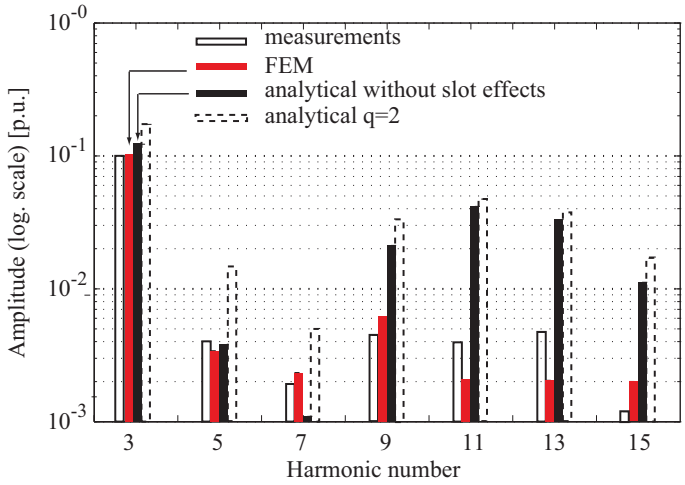

Figure 6.5: Spectrum of the back-EMF for different cases.

6.1.5 Calculations and measurements of the torque

The effects of the non-sinusoidal MMF have been shown to be negligible. The back-EMF is close to sinusoidal, and the self-inductances are equal and constant. Consequently, the calculated dq inductances can be assumed constant and the mutual dq inductances equal to zero. It should then be possible to calculate an accurate value of the mean torque using the dq theory and describe the steady state operation of the motor with a phasor diagram in the dq plane. This is verified with FE-simulations and measurements at load conditions.

Phasor diagram

The phasor diagram in the dq plane for a non-salient motor is given in Figure 6.6. The torque T, speed Ω, fundamental of the supplied voltage V, fundamental phase current I and phase angle φ, are measured in the flux-weakening region in order to avoid saturating the iron. The inductance L is obtained from a blocked-rotor test with the measurement of the d-axis flux shown in Figure 6.7. The nominal current of the machine is 3 A. As can be seen, the magnetic circuit begins to saturate for a current over +0.5 A. From the linear approximation of the flux, the d-axis inductance is calculated to 94 mH. If equations (6.15) and (6.16) are verified, the phasor diagram can be used to describe steady state operation. R is the phase resistance, ω the angular frequency and E_0 the back-EMF.

$$\varphi_{dq} = \arcsin((L\omega I_q - RI_d)/V) + \arctan(I_d/I_q) \tag{6.15}$$

$$V_{dq}^2 = (E_0 + RI_q + L\omega I_d)^2 + (L\omega I_q - RI_d)^2 \tag{6.16}$$

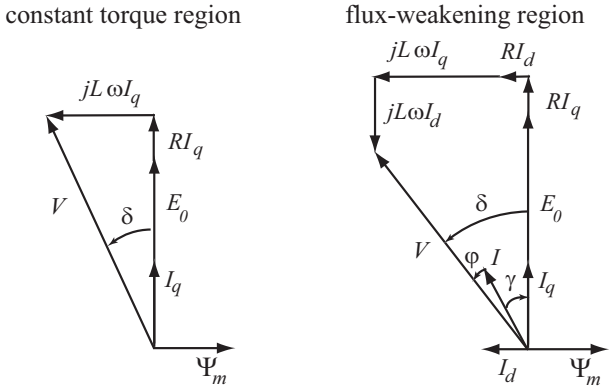

Figure 6.6: Phasor diagram of a non-salient motor.

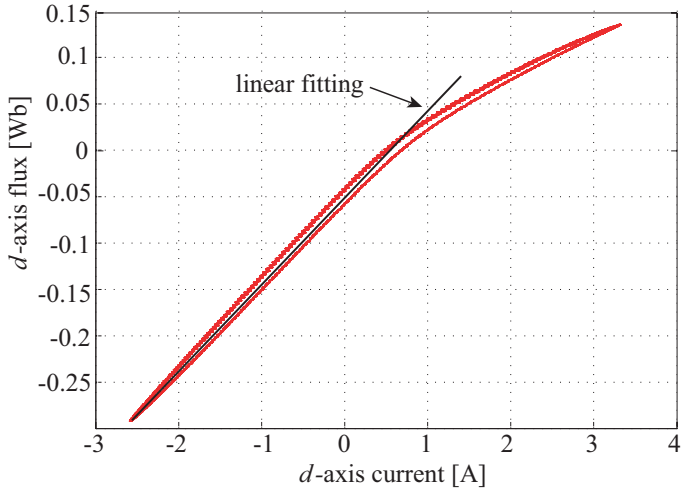

Figure 6.7: Measured d-axis flux as a function of the d-axis current and the linear approximation

Torque

The electromagnetic torque is calculated from equation (6.14) and for a d-axis current lower than 0.5 A. The torque measured at the shaft of the machine is lower than the calculated electromagnetic torque since the iron losses, friction losses and other miscellaneous losses are not taken into account in the calculation. In order to take these losses into account and fairly compare the measured torque with the electromagnetic torque, a loss torque is subtracted to the magnetic torque:

$$T_{dq} = \frac{3}{2}\frac{p}{2}\psi_m I_q - (P_{in} - P_{out} - P_{cu})/\Omega. \tag{6.17}$$

The losses are easily calculated by making the difference between the input power P_{in} and mechanical power P_{out} and subtracting the copper losses P_{cu}.

Table 6.1 gives the values of the different measured quantities. It is checked if equations (6.15) and (6.16) are verified. Considering the measurements accuracy, the dq calculated quantities agree well with the measured quantities. Therefore, the dq model of the motor with non-overlapping concentrated windings can be used to calculate the torque and steady-state operation of this machine.

Table 6.1: Comparison between measurements and dq values.

q-axis current I_q [A]	1.37	1.51	2.04	2.25	2.93
d-axis current I_d [A]	-2.00	-1.31	-1.94	-3.69	-3.79
V from measurements [V]	160.54	164.86	159.33	155.53	158.15
V_{dq} from (6.16) [V]	159.86	164.16	157.72	155.57	158.23
relative error on V [%]	0.43	0.42	-0.14	-0.03	-0.05
φ from measurements [deg]	-17.18	-9.11	4.29	27.42	35.19
φ_{dq} from (6.15) [deg]	-17.09	-9.06	4.33	27.46	35.27
relative error on φ [%]	-0.52	-0.55	-1.00	0.15	0.21
torque from measurements	9.12	10.14	14.13	15.05	19.92
torque T_{dq} from (6.17)	9.08	10.09	14.29	13.96	19.92
relative error on T [%]	0.47	0.49	1.15	~ 0	~ 0

6.1.6 Conclusions

dq theory is applied to a PMSM with non-overlapping concentrated windings. Although the windings are not sine-distributed, the torque and steady-state operation can be accurately calculated with the simplified dq model, if the magnetic circuit is not saturated. Indeed, the effect of the MMF space harmonics on the inductance is negligible and the back-EMF is close to sinusoidal.

In the next section, different methods to measure the d- and q-axes inductances are presented.

6.2 Inductance measurements on a PMSM without position sensor

6.2.1 Literature study

The control of a PMSM requires the knowledge of its inductances. Moreover, the determination of the speed capability of the machine under field-weakening operation depends strongly on the value of the d-axis inductance [78]. An accurate estimation of the inductances is therefore crucial for an efficient control of the machine.

However, this estimation is sometimes difficult; the values of the d- and q-axes inductances are depending on different phenomena such as saturation in the iron or cross-coupling between the two axes. Hence, analytical calculations of the inductances may be inaccurate [84].

FE simulations allow taking these phenomena more easily into account. Several methods are available to estimate the inductances using FE analysis. A fast and simple method is to calculate the inductances from a static simulation by computing the stored magnetic energy, as in [118]. However, the influences of the d- and q-axes coupling and the magnet flux linkage are not taken into account. Another possibility is to linearize the problem by fixing the iron magnetic permeability obtained from a first simulation and by computing the problem again. The inductances can then be calculated from the co-energy using the energy-perturbation method [119, 120], or from the flux linkages as in [121–123]. Alternatively, with FE programs that enable to couple a circuit to the meshed geometry, it is possible to calculate the inductances reproducing the methods used for the measurements, as described in [124] with a blocked-rotor method.

The inductances can be measured using different methods. A first common method is a test at standstill conditions with a blocked rotor. In [125], the windings are supplied with an AC voltage and the inductances are indirectly calculated from the measurement of the reactive power. In [124], the supplied voltage in the d- or q-axis changes stepwise while the current of the other axis is constant. The inductances are calculated by integrating the measured voltages and currents. Cross-coupling inductances for all d- and q-axes currents can be defined. This method requires a rather complicated experimental setup with a controlled voltage source inverter. Another common method is to analyze the measurements from a test at load [125–127]. This method requires the knowledge of the magnet flux linkage, and of the load angle or of the angle between current phasor and q-axis. In [128], the inductances are obtained from a no-load and load test without the need of a position sensor.

All the mentioned methods have their advantages and drawbacks. Among the drawbacks, a reliable position sensor is commonly required. Furthermore, the values of the simulated or measured inductances are different depending on the method. In this section, the differences or agreements between the results from two AC standstill tests and from a load test are investigated. The proposed methods require a simple experimental setup without the need of a position sensor. The first method is an AC standstill test in which the inductances are calculated from the flux linkages. With the same experimental setup, the inductances can also be calculated from the measurement of the reactive power. Finally, a new method is proposed to calculate the inductances from measurements performed at load, without any knowledge of the rotor position. A no-load test as in [128] is not required. The proposed methods can easily be reproduced using FE analysis. Results from the 2D- and 3D-FE simulations are compared to the measurements.

6.2.2 AC standstill methods

Standstill tests are commonly used to measure the inductances. There are different ways to analyze the measured data obtained from an AC standstill test and calculate the inductances. The first proposed method, referred to as Method I, is based on the indirect measurement of the flux linkage. The second method, Method II, is based on the measurement of the reactive power. For each method, measurements are compared to results from FE simulations.

Inductances calculated from the flux linkages (Method I)

A. Description of the method

Different setups are possible for AC standstill tests. The proposed method is a variant of the method described in [124]. Instead of a controlled voltage source inverter, a sinusoidal voltage source supplies the windings. Without any position sensor, the experimental setup is further simplified. Since the neutral of the windings of the tested motor is not accessible, two phases of the windings are parallel-connected, as shown in Figure 6.8. The d- and q-axes inductances, L_d and L_q, are calculated from the measured voltage u and the measured currents in each phase of the windings i_a, i_b, i_c, with the rotor blocked in two different positions. The position, called d-axis position, corresponding to an alignment of the phase a axis with the d-axis, gives L_d. The position in quadrature, the q-axis position, gives L_q. The d-axis position is found by supplying the windings with a DC current when the rotor is unblocked.

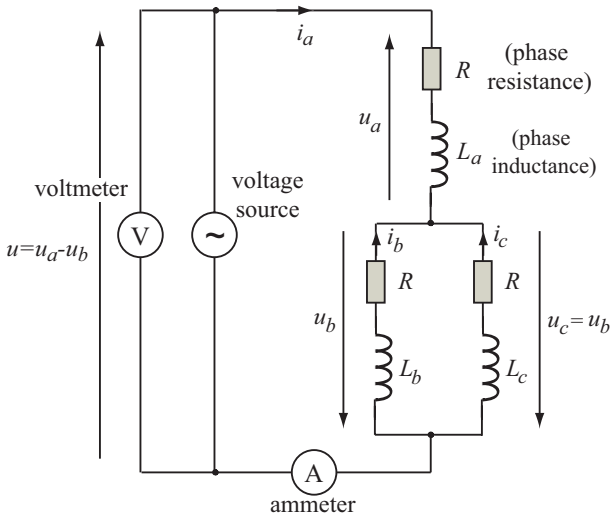

Figure 6.8: Inductance measurement setup for the AC standstill methods.

The phase voltages u_a, u_b, u_c are transformed into d- and q-axes components u_d, u_q using the Park transformation:

$$\begin{pmatrix} u_d \\ u_q \end{pmatrix} = \frac{2}{3} \begin{pmatrix} \cos\theta & \cos(\theta - \frac{2\pi}{3}) & \cos(\theta - \frac{4\pi}{3}) \\ -\sin\theta & -\sin(\theta - \frac{2\pi}{3}) & -\sin(\theta - \frac{4\pi}{3}) \end{pmatrix} \begin{pmatrix} u_a \\ u_b \\ u_c \end{pmatrix} \tag{6.18}$$

where θ is the position of the rotor in electrical radians.

Since u_b=u_c, the d- and q-axes voltages can be expressed as

$$\begin{cases} u_d = \frac{2}{3}(u_a - u_b)\cos\theta = \frac{2}{3}u\,\cos\theta \\ u_q = -\frac{2}{3}(u_a - u_b)\sin\theta = -\frac{2}{3}u\,\sin\theta. \end{cases} \tag{6.19}$$

u_d and u_q are then directly proportional to the measured voltage u, the position θ being constant since the rotor is blocked. The d- and q-axes currents, i_d and i_q, are calculated from the Park transformation of the measured currents in the phase windings, i_a, i_b, i_c as for the voltages in (6.18). d- and q-axes flux linkages, ψ_d and ψ_q, can then be calculated by integrating the voltages:

$$\psi_{di} = \psi_d - \psi_m = \int (u_d - Ri_d)dt = L_d i_d \tag{6.20}$$

$$\psi_{qi} = \psi_q = \int (u_q - Ri_q)dt = L_q i_q \tag{6.21}$$

where ψ_m is the magnet flux linkage and is not time dependent since the rotor is blocked. ψ_{di} and ψ_{qi} are the flux linkages created by the currents in d- and q-axes

respectively. R is the phase resistance. The constants of integration are calculated by setting the flux linkages ψ_{di} and ψ_{qi} to zero when the current is zero.

When the rotor is in the d-axis position, the d-axis inductance can be calculated from (6.20) for a q-axis current equal to zero. Similarly, the q-axis inductance can be calculated from (6.21) for a d-axis current equal to zero, when the rotor is in the q-axis position. In any given position of the rotor other than the d- and q-axes positions, it is possible to measure the effect of the cross-coupling between the axes, as in [124]. In this case, the d- and q-axes currents vary both sinusoidally. It is thus not possible to find the cross-coupling fluxes or inductances for whatever combination of values of the d- and q-axes currents. However, this method can give an idea of the influence of the cross-coupling between the axes on the inductances. Some values of the cross-coupling inductances can be calculated for particular values of the currents. However, without using a position sensor, it is difficult to find an accurate position other than the d- and q-axes positions.

B. Results from FE simulations and measurements

The presented method can easily be used to calculate the inductances from FE simulations if the FE program allows the coupling of an electrical circuit to the meshed geometry. The circuit used for the simulation is similar to the one in Figure 6.8. An AC source supplies the windings with a sinusoidal current. The speed is set to zero and the rotor is turned in the desired position. Integrating the voltage is not necessary since the fluxes seen by the coils are usually directly computed in the FE program.

Corresponding measurements were performed on the PMSM (Appendix C) using a power analyzer. A sinusoidal power generator supplies the motor. The rotor was positioned successively in the d- and q-axes positions. The measurements were done at 30 Hz with a RMS current of 3 A, which is the motor's nominal RMS current.

Figure 6.9 and Figure 6.10 show the measured flux linkages and inductances at 30 Hz and the 3D- and 2D-FE simulated results. An end-winding (e.w.) inductance of 30 mH obtained from a static 3D-FE simulation is added to the 2D-FE computation. The flux linkage obtained from 3D-FE simulations shows a thin hysteresis cycle which is likely due to imperfections in the mesh. As can be seen, there is a very good agreement between the 3D-FE results and the measurements. The inductances are obtained by interpolating the flux linkage with a fifth degree polynom. The difference with and without interpolating the flux is shown in Figure 6.9.b and Figure 6.10.b. There is a difference of 16 % between measurements and 2D-FE results for the d-axis inductance at negative d-axis currents and zero q-axis current. This difference is mostly due to the axial and fringing flux effects at the ends of the machine that are important since the machine is short.

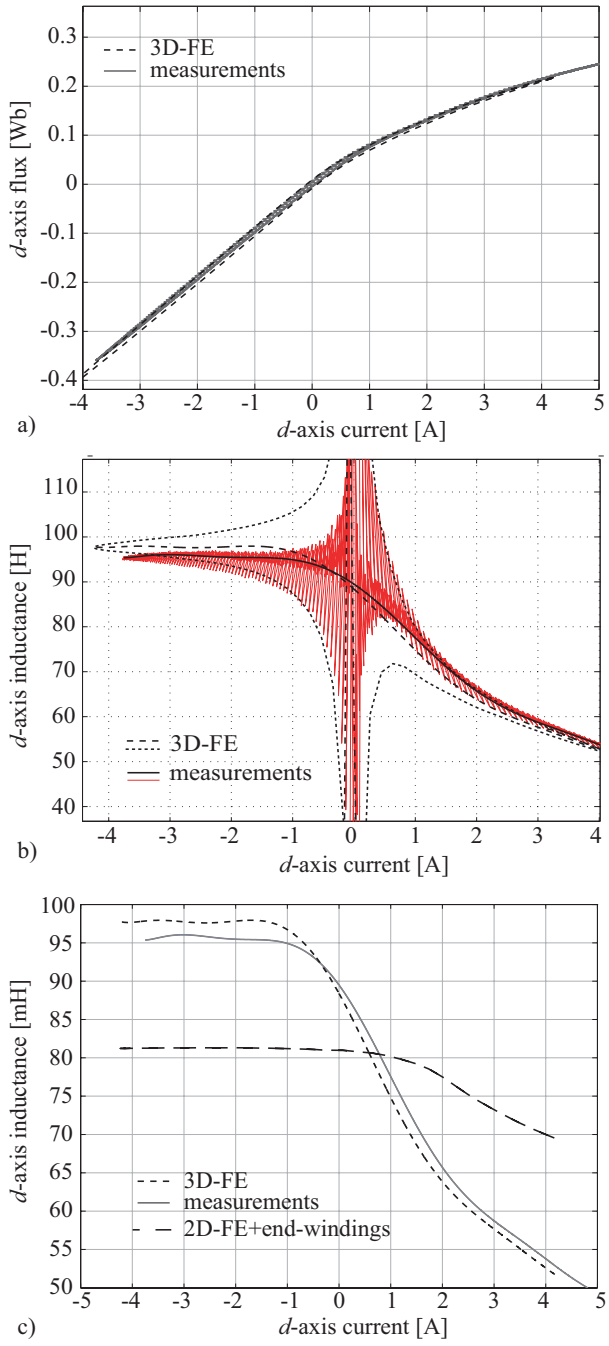

Figure 6.9: a) *d*-axis flux linkage obtained from Method I;
b) *d*-axis inductance obtained directly from the flux or from the polynomial approximation of the flux;
c) *d*-axis inductance obtained from the polynomial approximation of the flux.

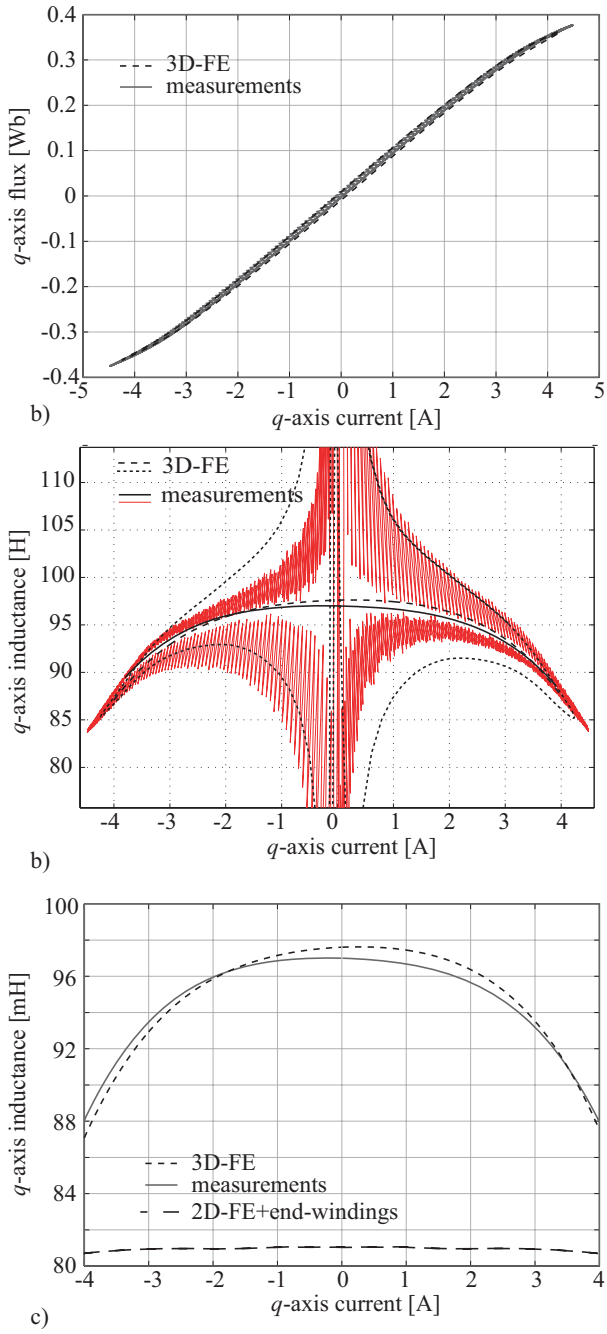

Figure 6.10: a) q-axis flux linkage obtained from Method I;
b) q-axis inductance obtained directly from the flux or from the polynomial approximation of the flux;
c) q-axis inductance obtained from the polynomial approximation of the flux.

C. Advantages and drawbacks

This method presents some advantages:

- There is no need to access the neutral point of the winding.
- Saturation of the iron is taken into account.
- The inductances can be measured as a function of the d- and q-axes current.
- Some values of the cross-coupling inductances can be measured.
- The method is easy to implement with a FE program.
- The d-axis inductance can be found without knowing the magnet flux linkage ψ_m.

Some drawbacks are:

- It may not be possible for the sinusoidal power generator to deliver the rated current if it is high. It is then not possible to find the values of the inductance when the machine is saturated. Furthermore, the maximum value of the supplied current should be chosen carefully in order to not demagnetize the PMs.
- The waveforms of the voltage and currents are needed. An accurate oscilloscope and adequate probes should be used. The waveforms have to be integrated, which requires to know the value of the resistance of the windings.
- When there are many poles, it is difficult to position accurately the rotor when there is no position sensor. This is specially true for a position different than the d- and q-axes, investigated to obtain the cross-coupling inductances.
- There are some transients when simulating with FE methods. The simulation should last long enough to attain the steady-state.
- Interpolation of the flux by a numerical curve-fitting function can introduce errors.

Inductances calculated from the reactive power (Method II)

A. Description of the method

The measurement setup is the same as previously; the rotor is blocked and two phases are connected in parallel as in Figure 6.8. The d- and q-axes inductances are calculated from the measurements of the reactive power Q, RMS current I and frequency f, with a rotor in the d- and q-axes position respectively:

$$L_d = \frac{2}{3}\frac{Q_{d\text{-axis position}}}{2\pi f I^2_{d\text{-axis position}}} \tag{6.22}$$

$$L_q = \frac{2}{3}\frac{Q_{q\text{-axis position}}}{2\pi f I^2_{q\text{-axis position}}}. \tag{6.23}$$

The value of the RMS current is varied up to the rated current. The method was proposed in [92].

B. FE simulations and measurements

The inductances calculated from measurements of the reactive power at 30 Hz and from FE simulations are shown in Figure 6.11. Contrary to the results from Method I, the measured d-axis inductance is lower than the 3D-FE simulated inductance. However, it is close to the 2D-FE simulated value that includes the end-winding inductance. The difference is due to the way the FE simulations are performed. To reduce the simulation time, the FE simulations are current-driven, which means that the current is sinusoidal but the voltage contains harmonics. During the measurements it is the contrary, the voltage is sinusoidal but not the current. This is illustrated in Figure 6.12 for the rotor in the d-axis position. Although the RMS value of both currents is 3 A, the current during the measurements reaches higher values than during the FE simulations. The iron gets more saturated and thus the measured inductance is lower. In the q-axis position, the saturation level is lower. Therefore, the measured q-axis inductance is close to the 3D-FE value and higher than the 2D-FE value, as was the case with Method I.

C. Advantages and drawbacks

This method presents some advantages:

- Only a power-meter is needed.
- Analyzing the measurements to calculate the inductance is easy.

The drawbacks are:

- It is not possible to find the value of the d-axis inductance with negative d-axis current.
- It is not possible to find the cross-coupling inductance.

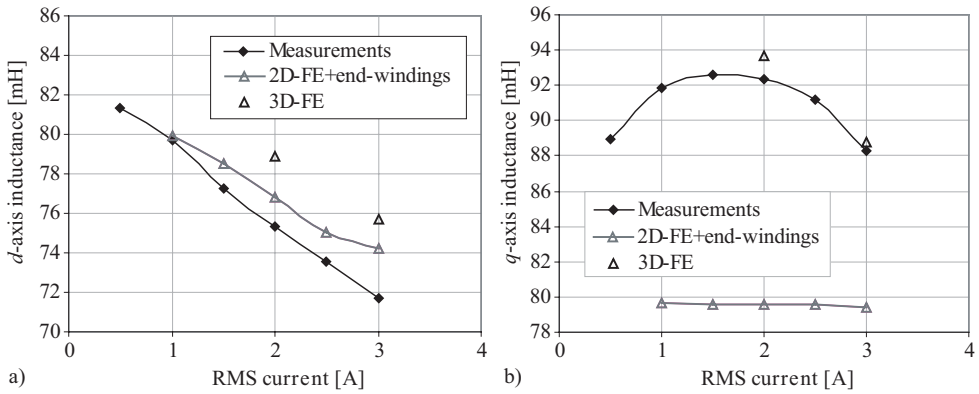

Figure 6.11: Inductances as a function of the RMS current, from measurements and FE simulations with Method II: a) *d*-axis inductance; b) *q*-axis inductance.

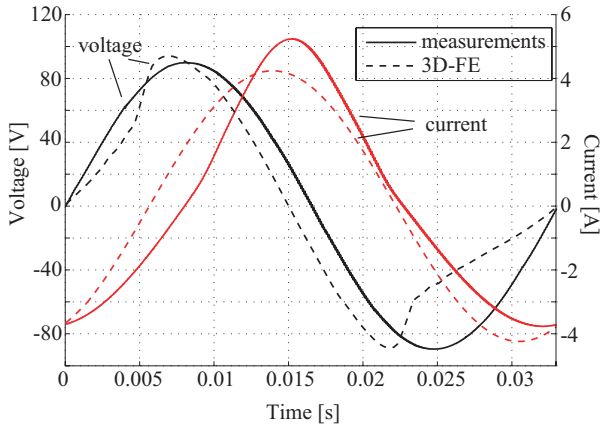

Figure 6.12: *d*-axis voltages and currents from AC standstill measurements and 3D-FE simulations.

D. Comparison of the two AC standstill methods

With Method I, the inductances are calculated from the flux linkage by integrating the measured voltage when the rotor is blocked in a known position. Besides the simple experimental setup, there are several advantages of using this method. Only two sets of measurements are needed, one in the *d*-axis and the other in the *q*-axis position. The inductances can also be calculated from the reactive power using the same measurement setup. Several sets of measurements for different current amplitudes at the *d*- and *q*-axes positions are necessary.

The values of the *d*-axis inductance obtained with Method I and II are shown in

Figure 6.13. The d-axis inductances obtained with Method I at positive and negative d-axis currents are plotted together as a function of the absolute value of the current. As can be seen, there is a large difference between them due to saturation effects. Figure 6.13 shows that the inductance values obtained from Method II are close to the average between the inductance values measured at positive and negative current obtained with Method I. This was verified both with measurements (Figure 6.13.a) and FE simulations (Figure 6.13.b). The inductance values obtained with Method II are therefore neither the values when the magnetic circuit is out of saturation nor when there is saturation, but a mix between these two.

Calculating the inductance from the reactive power is an alternative to Method I, avoiding both measuring the voltage and current waveforms and the integration of the voltage. However, the inductance values obtained with Method II are not exactly the desired values as the motor is usually driven at constant d- and q-axes currents when loaded.

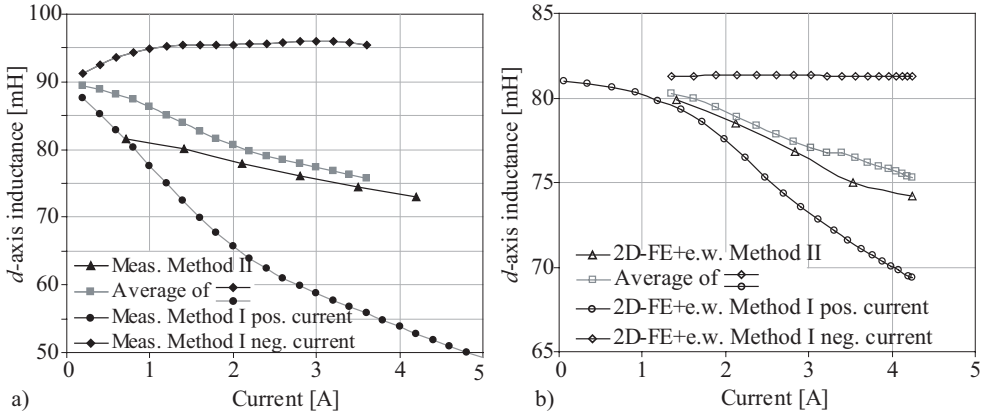

Figure 6.13: d-axis inductances obtained from the two AC standstill methods: a) From measurements; b) From 2D-FE simulations.

6.2.3 Inductances calculated from measurements at load (Method III)

A. Description of the method

The inductances are calculated from measurements performed when the motor is loaded. Using this method, referred to as Method III, it is possible to find the inductances when the load angle δ or the angle γ between current phasor and q-axis is unknown, i.e. there is no information on the position or it is not reliable.

Unlike in [128], d- and q-axes inductances and currents are obtained only from load tests. The induced back-EMF E_0 is obtained from the open-circuit voltage. The measurement setup is simple; a torque-meter measures the torque T and mechanical speed Ω while a power analyzer measures voltages, currents and powers. The method can be explained with different means: graphically with the help of the phasor diagram (Figure 6.14), or mathematically with equations (6.24)-(6.29).

The following quantities are measured: torque T, speed Ω, fundamental line-to-line voltage U_1, fundamental phase current I_1, active power P and the angle between the phase current and phase voltage φ. These known quantities are pictured in the phasor diagram shown in Figure 6.14.a, where V_1 is the fundamental of the supplied phase voltage, R the phase resistance and ω the angular frequency.

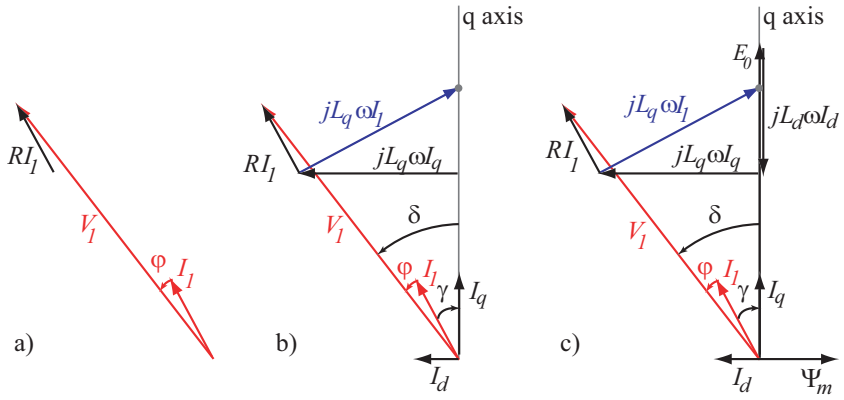

Figure 6.14: Phasor diagram for the flux-weakening region.

1 At first, a value of L_q is chosen by guess to find the q-axis. In the phasor diagram, this can be done by plotting $jL_q\omega I_1$, as shown in Figure 6.14.b. Indeed, the projection of $jL_q\omega I_1$ on the d-axis is $jL_q\omega I_q$. This procedure is equivalent to finding the value of I_q that gives the measured angle φ according to

$$\varphi = \delta - \gamma = \arcsin((L_q\omega I_q - RI_d)/V_1) + \arctan(I_d/I_q). \tag{6.24}$$

As can be seen in equation (6.24), when a value of L_q is assumed, I_d and I_q are the only unknown variables and I_d is given by

$$I_d = \pm\sqrt{I_1^2 - I_q^2}. \tag{6.25}$$

2 The d-axis inductance can then be calculated from the phasor diagram as in Figure 6.14.c or from

$$V_1^2 = (E_0 + RI_q + L_d\omega I_d)^2 + (L_q\omega I_q - RI_d)^2 \tag{6.26}$$

assuming that the back-EMF E_0 is constant and equal to its no-load value.

3 This process (steps 1 and 2) is iterated for different values of L_q for the same set of measurements (same speed and torque). Figure 6.15 illustrates, for different values of L_q, how to graphically find the value of I_q for which the angle φ calculated from equation (6.24) corresponds to the measured angle.

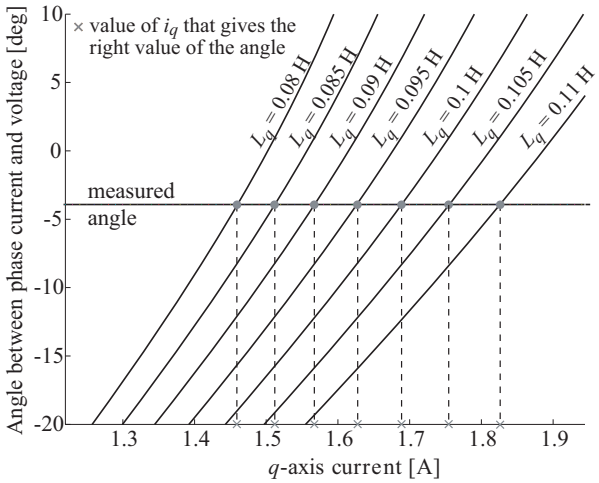

Figure 6.15: Angle φ calculated from different guessed L_q compared to the measured angle, as a function of the q-axis current.

4 For each set of currents and inductances, the torque equation should be fulfilled:

$$\frac{3}{2}\frac{p}{2}[\Psi_m I_q + (L_d - L_q) I_d I_q] - T_{\text{loss}} = T \tag{6.27}$$

The magnetic torque calculated from the flux linkages does not take the iron-losses, friction losses and other miscellaneous losses into account. Therefore, a loss torque T_{loss} is subtracted from the magnetic torque in order to consider these losses. The value of the loss torque is obtained from the difference between the input power and the mechanical power, and the subtraction of the copper losses:

$$T_{\text{loss}} = (P_{in} - T\Omega - 3RI^2)/\Omega \tag{6.28}$$

The difference between the calculated and measured torque should be in the range of the torque measurement accuracy, otherwise the solution is disregarded. Up to now, several possible inductance and current values have been found for a same speed and torque, as illustrated in Figure 6.16.a with the encircled data as an example.

5 Other measurements at different torques and speeds are analyzed following the same procedure (steps 1-4). Figure 6.16.a shows L_d and L_q for different speeds and torques. As can be seen, L_d, unlike L_q, does not vary much with the current. Using an estimation of the saliency, the region of variation of L_q can eventually be limited.

6 L_d can now be expressed as a function of I_d with a polynomial extrapolation. This is possible since L_d is approximately constant for a given speed and torque. Figure 6.16.b shows a curve that fits well to the found values of L_d. L_d is extrapolated to a second order polynomial function in this case.

7 Finally, L_q is calculated as a function of I_d from the torque equation (6.27) using the extrapolated expression of L_d:

$$L_q = L_d(I_d) - \left(\frac{2}{3}\frac{2}{p}(T + T_{\text{loss}}) - \Psi_m I_q\right)/(I_d I_q) \tag{6.29}$$

With this value of L_q, I_d is obtained by finding the value that fulfills (6.24) and (6.26).

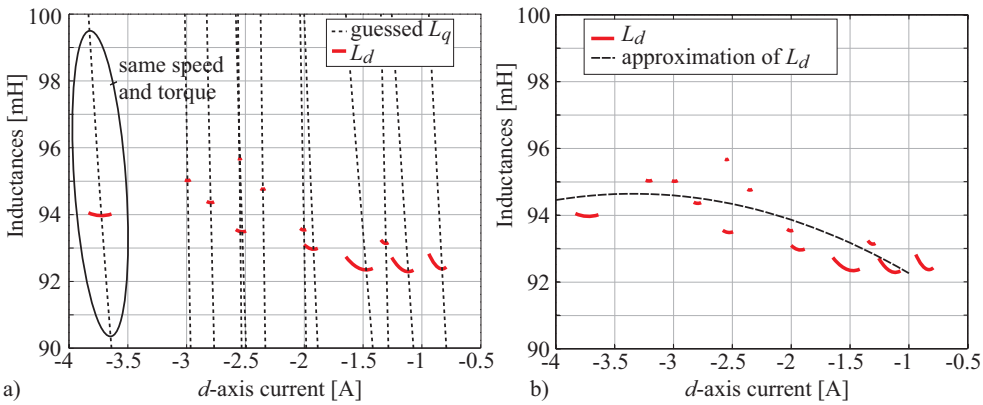

Figure 6.16: a) d- and q-axes inductances for different speeds and torques; b) Polynomial extrapolation of the d-axis inductance.

B. FE simulations

Load time-step simulations with FE methods can be used to calculate the inductances. To simulate the load, a sinusoidal current supplies the windings and the rotor is rotated at a constant speed. Unlike with Method I, several simulations are required to find different values of inductances as a function of the current. The load angle and the d- and q-axes currents are known. The inductances can then be calculated directly from the flux linkages computed during the simulations. The torque equation (6.27) should be verified with the found values of inductances and with $T_{\text{loss}} = 0$.

Figure 6.17 shows the values of the inductances calculated from FE simulations with Method III compared to the inductances calculated from the AC standstill tests (Methods I and II). For a large negative d-axis current, the inductances from Method I and III agree well. For Method III, a discontinuity of the d-axis inductance around $I_d = 0$ can be observed. The discontinuity is due to the back-EMF that is kept constant to its no-load value, whereas in reality it varies when the motor is saturated [129]. As a result, the calculated values of the d-axis inductance at low d-axis current are unreliable. The values of the q-axis inductance obtained from Method III agree well with the values obtained from Method I when the d-axis current is close to zero. As the d-axis current is increased, the q-axis inductance decreases, which shows the influence of the cross-coupling between the d- and q-axes.

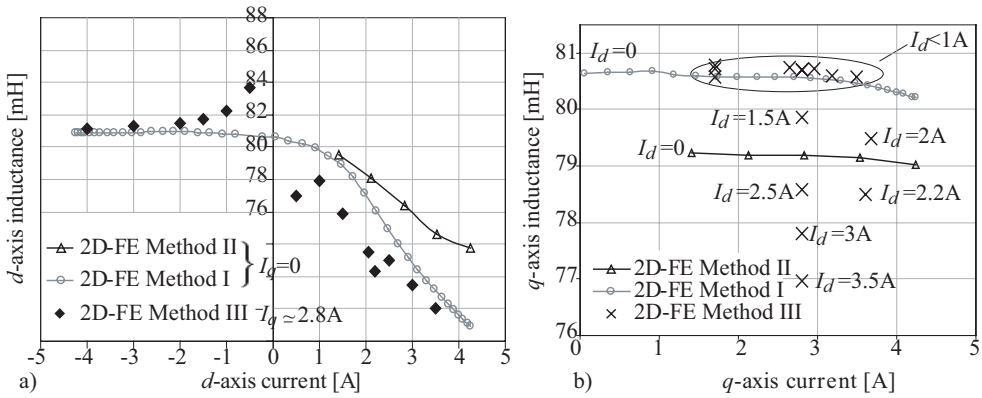

Figure 6.17: FE-calculated inductances from Methods I, II, and III: a) d-axis inductance; b) q-axis inductance.

C. Measurements

Figure 6.18 shows the d- and q-axes inductances calculated from the measurements at load condition with Method III compared to the inductances found from the AC standstill test following Method I. The d-axis inductance measured with Method III is only approximately 2 % lower than the value of the inductance found with Method I for a zero q-axis current. The value of the d-axis inductance is quite sensitive to the value of the back-EMF. A decrease of 2 % of the magnet flux linkage results in a 3 % decrease of the d-axis inductance. Furthermore, the values around zero d-axis current are not reliable because of the assumption of a constant back-EMF [129]. Introducing a varying value of the back-EMF could suppress this problem. However, for a large negative d-axis current, the iron should not be much saturated and the magnet flux linkage should be close to its no-load value.

Except for a few points, the values of the q-axis inductance calculated with Method I are in good agreement with the inductance values from Method III, although the load angle was unknown.

It has not been possible to test Method III when the motor is operated with a positive d-axis current. The method should work as well in this case, but the assumption of a constant back-EMF is a problem if the motor is saturating with positive d-axis current. This assumption may also lead to inaccuracies if there is a large variation of temperature in the motor during the measurements. Indeed, the back-EMF varies with the temperature. However, the temperature variation can be taken into account, if it is measured near the PMs, by using the coefficient of temperature variation of the PM remanence flux density given by the PM manufacturer and thus making the back-EMF temperature dependent.

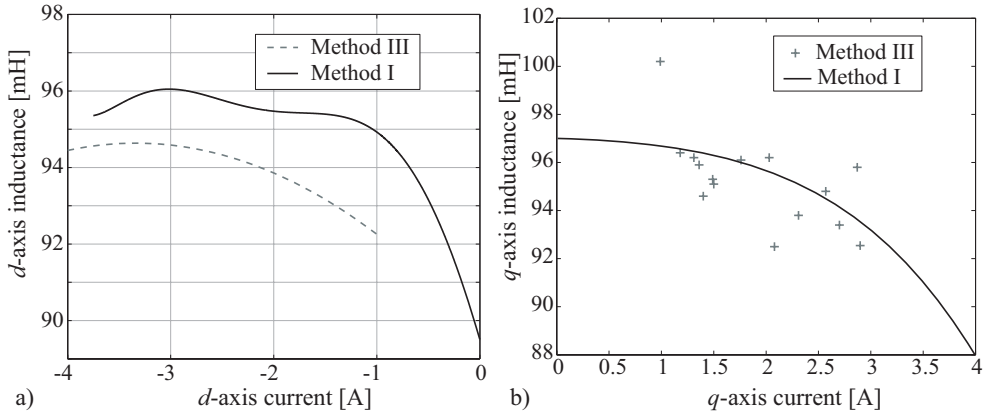

Figure 6.18: Measured inductances obtained with Method I and III: a) d-axis inductance; b) q-axis inductance.

D. Advantages and drawbacks

The advantage of this method is that it gives the inductance that is useful, for example to implement the control model in the drive.
However, this method has several drawbacks:

- The method is complicated.
- The method has been tested on one motor only.
- The back-EMF value E is not known at load. The no-load value is usually used. Other methods exist to get the value of E from FE simulations. This is specially important when the d-axis current is positive. Furthermore, the back-EMF varies with the temperature.
- The results are not reliable when the current is close to zero.

6.2.4 Conclusion

Three methods to obtain the inductances from measurements without position sensor or from FE simulations are presented and compared. The two first conventional methods use measurements when the rotor is blocked and the windings are connected to a sinusoidal source. The inductances can be calculated from the flux linkage by integrating the measured voltage, or from measuring the reactive power. The inductances calculated from the flux linkage are obtained as a function of the current, i.e. for different saturation levels of the iron in the machine. On the other hand, the inductances calculated from the reactive power are obtained for an average level of saturation in the machine corresponding to the value of the RMS current and thus, are not exactly the desired values.

The third and original method uses the measurements when the motor is loaded. The d- and q-axes inductances are found without knowing the load angle or the position of the rotor. It has been shown that measurements at load (Method III) and measurement of the flux linkage with blocked rotor (Method I) give values of inductances that are very close.

The inductances can be calculated from FE simulations by applying the proposed methods. The results from the 3D-FE simulations and the measurements are in good agreement. However, the inductances calculated from the 2D-FE simulation are not as close due to the shortness of the motor.

The inductances of the prototype motor have been measured because its flux-weakening capability depends on them. Additional measurements performed on the prototype, especially under flux-weakening operation are presented in the next chapter.

7 Analysis of Flux Measurements

In this chapter, measurements of the magnetic flux in the teeth and stator yoke of the prototype motor described in Appendix C are analyzed. The flux is measured indirectly by integrating the voltage induced in a search coil. Many results can be deduced from these original measurements performed at different conditions. At open-circuit conditions, the zigzag leakage flux flowing from one magnet to another through a tooth tip, which is large for PMSMs with non-overlapping concentrated windings, can be evaluated. The airgap component of the inductance and the slot leakage inductance can be measured during a blocked-rotor test. The comparison of the measurements with the results from 2D- and 3D-FE simulations allows validating the FE models and investigating locally the flux paths in the machine. Finally, at load conditions, the possibility to calculate the iron losses from the flux variations in different parts of the machine is investigated.

7.1 Measurement setup and FE model

The measurements are performed on the 28-pole, 24-slot, surface-mounted PMSM (Appendix C). Its nominal speed is 200 rpm and it can rotate over 1000 rpm at constant power under field-weakening operation. As mentioned in the previous chapter, 3D-FE simulations are required because the motor is short with a large diameter, and the rotor with its PMs is longer than the stator. 2D-FE simulations are also performed, although the results do not completely agree with the 3D-FE results and measurements because in the 2D-FE model, the machine's active length is set to the length of the stator lamination stack, i.e. 20 mm. The 2D-FE simulations are interesting because of the possibility to plot equiflux lines. The 3D-FE model of the machine is described in Appendix E.

Eleven search coils are placed in different parts of the prototype, as illustrated in Figure 7.1.a. The names defined in Figure 7.1 for the search coils are used in this chapter to ease the identification of the search coils. Since the search coils were placed after that the prototype has been built, the search coils placed on the tooth body are wound over the coil of the stator winding. One search coil of 10 turns is placed around the top of the tooth body near the tooth tip (sc_{th1}). Another coil of

10 turns is placed at the same height on a tooth next to the first search coil (sc_{th2}). This tooth carries a coil that belongs to the same phase of the winding as the coil under the first search coil. On another tooth, four coils of 3 turns each are wound at different heights (sc_{a1-d1}) and another four search coils are placed around the consecutive tooth at the same heights (sc_{a2-d2}). Finally one search coil of 7 turns is wound around the stator yoke (sc_{e1}). The voltages induced in the search coils are measured with a digital power analyzer and numerically integrated in Matlab in order to obtain the flux waveforms. The amplitude of the measured voltages at open-circuit and load conditions ranges from 0.5 V to 2 V depending on the search coil's turn number.

With FE tools, the flux can be calculated using different methods. Some search coils can be placed as in the prototype (Figure 7.1.b) and connected to an electrical circuit. Since this method increases the simulation time to a certain extent, only four search coils are added to the FE model. Two search coils (sc_{FEth1}, sc_{FEth2}) are placed around two consecutive teeth as for the measurements and two are placed around the stator yoke (sc_{FEe1}, sc_{FEe2}). The flux can also be calculated by adding a 2D path or a 3D grid in the iron. The advantage of this method is that the flux calculated from the grid can be decomposed in its radial, tangential and axial components. Grids (g_{a1-d1}, g_{a2-d2}) are defined at different places in the teeth in the 3D-FE model, as shown in Figure 7.1.b.

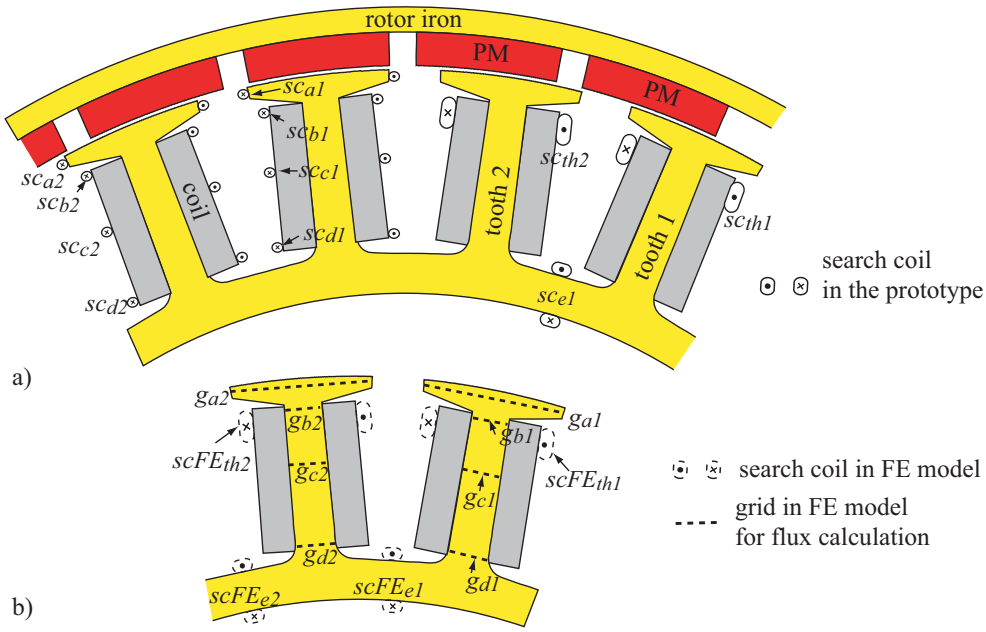

Figure 7.1: Placement of search coils: a) In the prototype; b) In the FE model.

7.2 Results at open-circuit condition

The analysis of the flux measurements at open-circuit conditions gives two interesting results. First, the measurements from the search coils allow retrieving the phase back-EMF waveform. The phase back-EMF waveform cannot be measured directly because the windings of the PMSM are Y connected with a neutral point that is not accessible. Because of the non-overlapping concentrated windings, the phase back-EMF is proportional to the sum of the voltages induced in the search coils of two consecutive teeth (sc_{th1}, sc_{th2}). As can be seen in Figure 7.2, there is approximately 3 % difference between the measured and 3D-FE simulated value of the amplitude of the back-EMF. This could be due to the value of the PM remanence flux density that is slightly lower in the prototype than in the FE model. The 2D-FE amplitude of the back-EMF is 12 % lower because the rotor is shorter in the 2D-FE model than in the 3D-FE model and prototype. This measurement of the back-EMF from the search-coils has been used in the spectrum analysis in the previous chapter (Section 6.1.4).

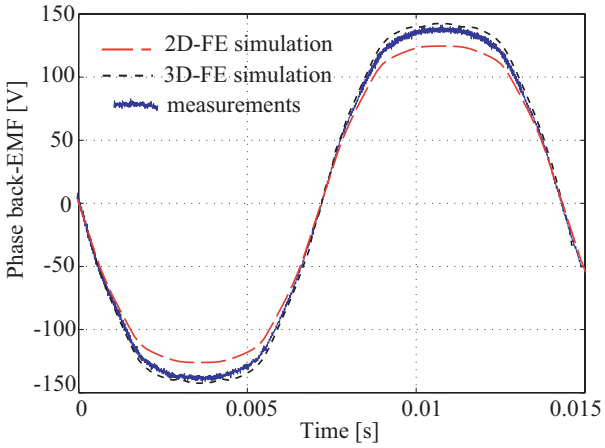

Figure 7.2: Measured and FE-simulated phase back-EMFs.

Second, the measurements at open-circuit conditions allow highlighting the zigzag leakage flux flowing through the tooth tips. PMSMs with non-overlapping concentrating windings have a number of teeth close to the number of poles. Because of this particularity, at certain rotor positions, part of the flux flows from one magnet to another through a tooth, as it is illustrated from a 2D-FE simulation in Figure 7.3.a. Analytical models for this zigzag leakage flux have been presented in [130] and compared with results from FE simulations. Figure 7.4.a shows the radial and tangential components of the flux density in a tooth tip obtained from the measurements and

3D-FE simulation at open circuit. The search coil "sees" only the radial component. Thus, the tangential component of the flux density cannot be measured. As can be seen, when the tangential component is maximum, the radial component is zero, which corresponds to the rotor position in Figure 7.3.a where the zigzag leakage flux is maximum. The radial component is maximum and the tangential component is zero when the tooth faces the magnet, as shown in Figure 7.3.b. These curves show the presence of the zigzag leakage flux. However, measuring directly the zigzag leakage flux is difficult. Additional search coils would be required and they should be wound around the tooth tips partly in the airgap and placed in precise positions.

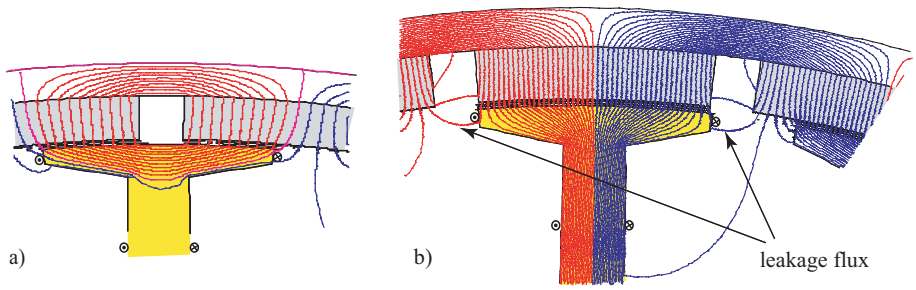

Figure 7.3: Equiflux lines in a tooth from a 2D-FE simulation for different rotor positions.

Nevertheless, another indication of leakage flux can be found from the search coils. Indeed, by subtracting the flux entering the tooth (obtained from the search coil wound around the tooth tip sc_{a1}) to the flux in the top of the tooth body (sc_{b1}), the flux leaking from the tooth tip is obtained. Figure 7.4.b shows this leakage flux in per unit, the reference being the maximum of the entering flux. The maximum of these curves corresponds to the case when a PM faces the tooth as in Figure 7.3.b. In Figure 7.3.b obtained from a 2D-FE simulation, 2 flux lines over the 50 plotted leave the tooth tip. This corresponds to the maximum of the 2D-FE simulated and measured curve in Figure 7.4.b ($0.04 = 2/50$). The 2D-FE results and measurements agree well, unlike the irregular 3D-FE curve. In Figure 7.4.a, the 3D-FE flux-density waveform agrees globally well with the measured waveform. However, a closer look to this curve shows some irregularities that cause the un-smoothness of the curve in Figure 7.4.b. These irregularities are certainly due to the position of the grid that may not match well to the meshed volume elements. The 3D-FE model shows some limits in the particular calculation of this leakage flux that requires high precision. Adapting the grid and mesh, and simulating with a smaller time step may give smoother results if required. However, this has not been carried out, since the 2D-FE results and measurements agree well.

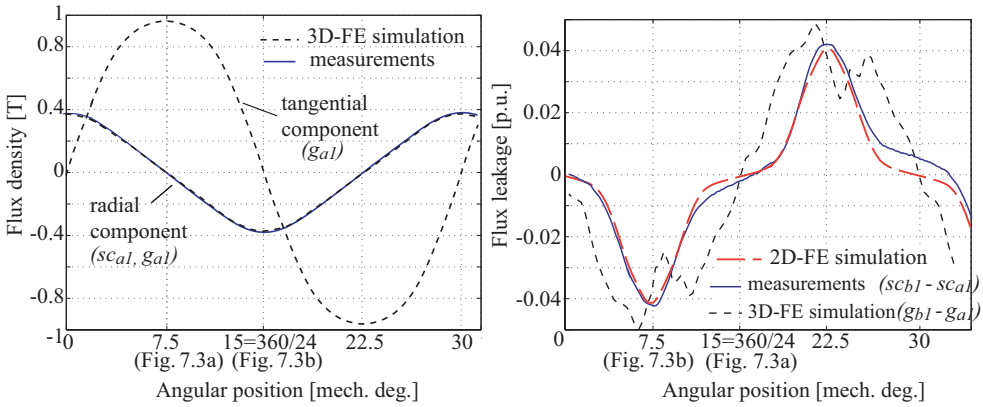

Figure 7.4: a) Radial and tangential component of the flux density in a tooth tip at open-circuit condition;
b) Difference between the flux flowing in the tooth and the flux flowing in the tooth tip at open-circuit condition.

7.3 Results from a blocked-rotor test

The inductance can be decomposed in its airgap, slot, and end-windings components. The airgap component of the inductance includes the magnetizing inductance and the harmonic leakage inductance due to the harmonics in the MMF distribution other than the synchronous-frequency component. The values of the inductance components are generally compared to results from FE simulations as in [82]. In this section, the possibility to measure the inductance components with the search coils is investigated in order to validate the results from FE simulations and check the repartition of each component in the total inductance.

The blocked-rotor test described in Chapter 6, Section 6.2.2 (Method I) is used to measure indirectly the airgap and slot components of the inductance. During the test, phases b and c of the motor are parallel connected because of the star connection of the windings. The rotor is positioned so that the axis of phase a is aligned with the d-axis.

The airgap component of the inductance is calculated from the measured or FE-calculated flux in the tooth tips ($sc_{a1} + sc_{a2}$, $g_{a1} + g_{a2}$) multiplied by the adequate number of turns. The difference between the flux near the stator yoke ($sc_{d1} + sc_{d2}$, $g_{d1} + g_{d2}$) and the flux in the tooth tips ($sc_{a1} + s_{ca2}$, $g_{a1} + g_{a2}$) multiplied by the same number of turns and divided by the current gives the slot leakage inductance. With FE methods, the inductance can also be separated into the usual components, slot leakage, airgap component or end-windings inductances, using the stored magnetic

energy calculated in different parts of the motor divided by the square of the current:

$$L_d = \frac{4}{3}\frac{E_{\text{magn}}}{I_d^2} \tag{7.1}$$

where L is the inductance, E_{magn} the stored magnetic energy and I the current. A factor 2/3 in this equation comes from the connection of the phase windings. The inductance calculations using the magnetic energy have been done with 2D and 3D-FE simulations using the same blocked-rotor test as for the measurements.

Table 7.1 gives the simulated and measured inductances obtained from the search coils or from the computation of the magnetic energy for a negative current, when the iron is out of saturation. First, the 3D-FE inductances calculated from the magnetic energy are slightly higher than the 2D-FE inductances calculated with the same method, certainly due to the larger axial length of the rotor in the 3D-FE model. The sum of the three components calculated from the magnetic energy gives an inductance value close to the value of the total inductance obtained in Chapter 6. The difference is due to the iron in the machine that also stores some magnetic energy. Secondly, there is approximately 6 % difference between the inductances calculated from the search coils and the inductances calculated from the magnetic energy. This suggests that the airgap and slot components of the inductances can be rather accurately estimated with the search coils in the prototype. However, there is 25 % difference between the measured and the 3D-FE simulated airgap-component inductances obtained from the search coil. The slot leakage inductances are closer but this result should be taken with some precaution as the slot component is calculated from the airgap component which did not agree with the 3D-FE airgap component. This discrepancy may be due to measurement inaccuracies. Indeed, the voltages induced in the search coils during the test are low, approximately 50 mV, since the rotor is blocked and the magnets do not induce any voltage. A higher number of turns for the search coils and more adequate measurement instruments could be used for this test. Nevertheless, the results show that the airgap-component, slot-leakage, and end-windings inductances account for approximately one third of the total inductance.

Table 7.1: FE-calculated and measured inductances.

Inductance	Method	2D-FE ind. [mH]	3D-FE ind. [mH]	Measured ind. [mH]
Airgap component	Search coils	35.0	34.2	27.5
	Magnetic energy	33.4	36.5	-
Slot component	Search coils	21.9	22.7	21.8
	Magnetic energy	20.6	21.5	-
End-windings	Magnetic energy	-	30	-

7.4 Results at load condition

In this section, the flux-density waveforms measured at load conditions (at base speed and under field weakening operation) are analyzed and compared to the results from FE simulations. The analysis leads to a discussion on the evaluation of the stator iron losses, their repartition in different regions of the stator and evolution under field-weakening operation.

7.4.1 Field-weakening operation

As mentioned in Chapter 3, Section 3.2.4, surface-mounted PMSM with concentrated windings can achieve a wide constant-power speed range under field-weakening operation due to their large d-axis inductance. As shown with the blocked-rotor test, the prototype motor has a high inductance due to the shortness of the machine that implies a relatively high end-winding inductance and non-negligible fringing-flux effects. Thus, the field-weakening index of this machine, defined in [80] as the ratio of the characteristic current $I_{ch} = \Psi_m/L_d$ over the rated current I_r, is equal to 0.77. The prototype motor can then run at speeds up to 6 times the base speed under constant power, as shown with the measurements in Figure 7.5. The flux-density waveforms and iron losses at base speed (200 rpm), 3 and 4.5 times the base speed (identified with arrows in Figure 7.5) are analyzed in the following.

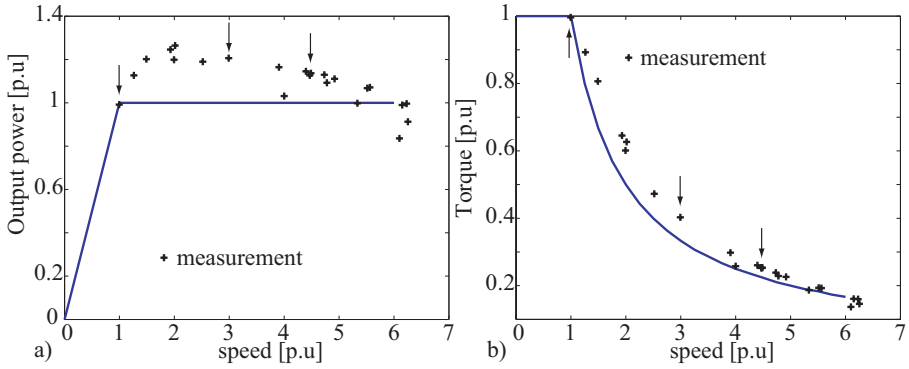

Figure 7.5: Measurements of: a) Torque versus speed; b) Output power versus speed.

7.4.2 Flux-density waveforms

Figure 7.6 show the measured and 3D-FE simulated flux-density waveforms at base speed and 4.5 times the speed, respectively. Several comments can be made from these figures. Firstly, the weakening of the flux can be noticed as the amplitude of the flux density drops e.g. in a tooth from 1.5 T at base speed to 0.6 T at higher speed.

Secondly, there is a difference in amplitude and harmonic content between the waveforms of two consecutive teeth, this difference being larger under field-weakening operation. At 4.5 time base speed (Figure 7.6.b), the amplitude of the flux density in the second tooth (sc_{b2}) is almost half of the amplitude in the first tooth (sc_{b1}). This difference is due to the ratio number of slots over number of poles and to the winding arrangement for which the phases are arranged in groups of two teeth. For this machine, the flux-density waveforms are different in two consecutive teeth, while they are the same (with different phase shift) in every second teeth. Under field-weakening operation, the zigzag leakage flux from one magnet to another is relatively higher, as shown in Figure 7.7 which accentuates the difference in the flux between two consecutive teeth.

In Figure 7.6.b, the FE-simulated flux-density waveforms calculated from the grid (thin broken line) and from the search coils (fat broken line) are plotted. As can be seen, the difference between these waveforms is significant, especially for the flux in "tooth 2". This was not the case at base speed and therefore, only the waveform from the grid was plotted in Figure 7.6.a. Figure 7.7 shows the equiflux lines at base-speed and under field-weakening operation for the same rotor position. As can be seen, under field-weakening operation, the leakage flux flowing from tooth to tooth through the slot and slot opening is relatively higher. The search coil, which is

in the slot over the winding coil, "sees" more flux than the grid placed in the tooth, explaining why the flux density is higher when calculated from the search coils than from the grids.

Finally, the agreement between the measurements and 3D-FE results is good. In Figure 7.6.b, the measured flux-density waveforms in both teeth agree well with the FE-simulated flux-density waveforms obtained from the search coil.

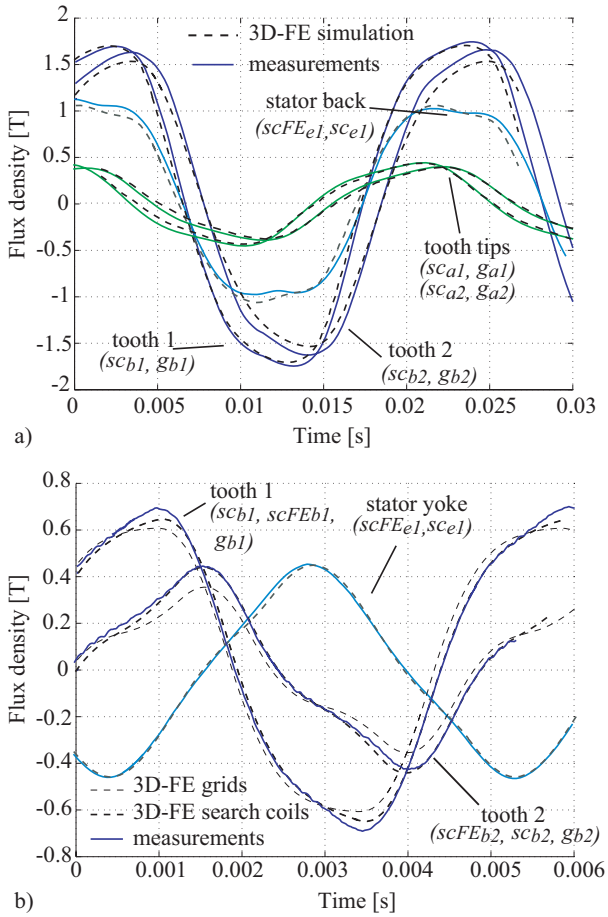

Figure 7.6: Measured and 3D-FE simulated flux-density waveforms: a) At base speed; b) At 4.5 times base speed.

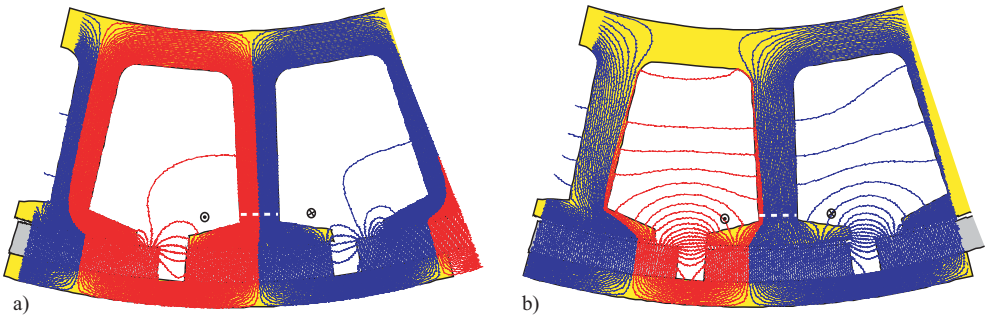

Figure 7.7: Equiflux lines: a) At base speed; b) At 4.5 times base speed.

7.4.3 Iron losses

The stator iron losses can be calculated from the measured flux-density waveforms. In [131], it is shown that the iron losses of a PMSM with buried magnets and distributed windings can be reasonably accurately estimated from one flux-density waveform in the stator tooth under field-weakening operation. In the case of a PMSM with non-overlapping concentrated windings, estimating the iron losses from the flux-density waveforms is more difficult, as is shown in the following. The possibility to evaluate the iron losses is investigated for the different regions defined in Figure 7.8, i.e. in the tooth tips, tooth body and yoke. As seen earlier, the flux-density waveforms are the same in every second teeth (except for the phase shift), thus one twelfth of the motor is represented, which corresponds to two teeth.

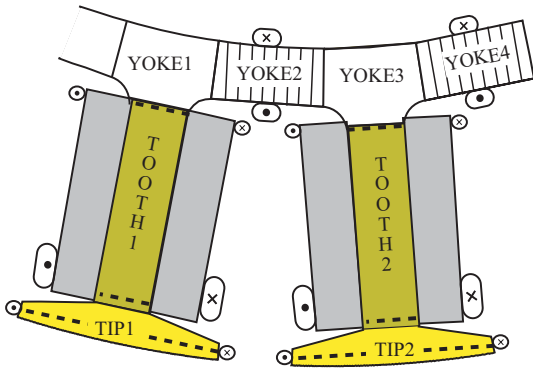

Figure 7.8: Definition of the investigated regions.

As shown in Figure 7.3.a, 7.4.a and 7.7.b, there is a large zigzag leakage flux flowing through the tooth tips. This zigzag leakage flux raises two difficulties for the evaluation of the iron losses in these regions. Firstly, the tooth tips are subject to rotational flux-density variations due to the zigzag leakage flux that flows in several directions. The rotational flux-density variation is shown in Figure 7.9.a, where the 3D-FE calculated tangential components of the flux density in the tooth tip are plotted as a function of the radial components at load conditions. Calculating the iron losses by taking into account the rotational core losses require the use of appropriate models. Calverley discusses this issue in [132] while investigating the iron losses in a switched reluctance machine that has rotational variations of the flux density in the tooth tips. Furthermore, the flux density is not uniform in the tooth tip, as can be seen in Figure 7.9.b. The flux density is high at one side of the tip and low at the other. A search coil around the whole tooth tip as the one placed in the prototype would, therefore, not reflect the non-uniform flux-density distribution in the tooth tip. Additional search coils wound around the tips through the airgap would be required in order to measure the variation of the tangential component of the flux density and to take this non-uniformity of the flux density into account.

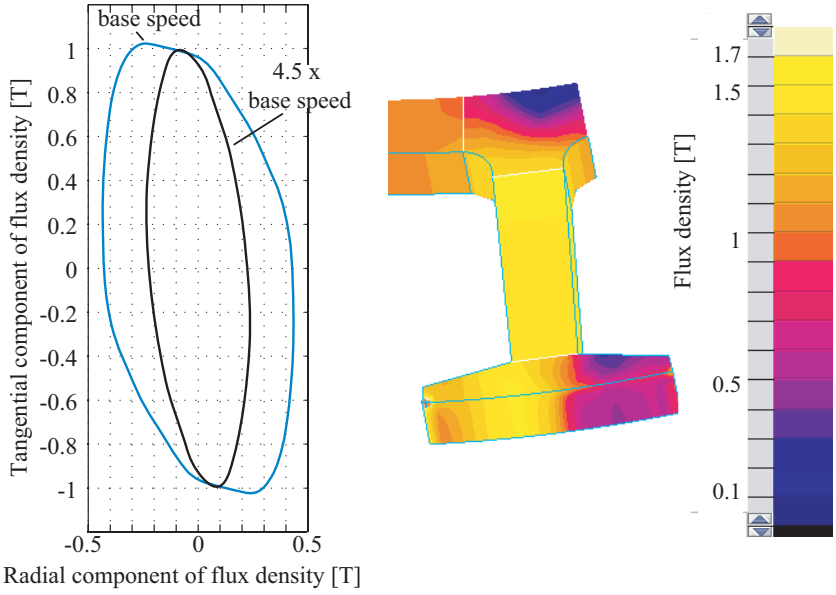

Figure 7.9: a) Tangential versus radial component of the flux density in the tooth tips; b) Flux-density distribution in a tooth at base speed.

In the tooth body, it is possible to use the flux-density waveforms from the search coils shown in Figure 7.6 to estimate fairly accurately the iron losses. Indeed, the tangential component of the flux density is small and the flux density does not vary much along the tooth body. The iron losses are calculated using classical models where the hysteresis loss, excess loss and eddy current loss are separated [133]:

$$dP_{\text{iron}} = \underbrace{k_h B_m^2 f k_f}_{\text{hysteresis loss}} + \frac{1}{T}\int_0^T \left[\underbrace{\sigma \frac{d^2}{12}\left(\frac{dB}{dt}(t)\right)^2}_{\text{eddy current loss}} + \underbrace{k_e \left(\frac{dB}{dt}(t)\right)^{3/2}}_{\text{excess loss}} \right] k_f dt \qquad (7.2)$$

where dP_{iron} is the volume density of the average power over a period T of the losses, B_m is the peak value of the flux density and B the instantaneous flux density. σ is the material's conductivity and d the lamination thickness. k_h and k_e are the hysteresis and losses in excess coefficients, that can be calculated from the steel manufacturer's data sheets. k_f is the stacking factor. The volume density of the power is then integrated over the volume of the investigated region, in order to get the losses P_{iron} dissipated in this region:

$$P_{\text{iron}} = \int\int\int_{region} dP_{\text{iron}} dv \qquad (7.3)$$

Figure 7.10.a shows the iron losses calculated in the tooth bodies from measured (sc_{b1}, sc_{b2}) and FE-simulated (g_{b1}, g_{b2}) flux-density waveforms, using only the radial component in (7.2). These results can be compared to the iron losses calculated in the FE software at each point of the mesh using the same presented models [133]. As expected, the agreement is rather good between the different methods with less than 4 % difference with the losses calculated from the FE software. At 4.5 times base speed, the measured losses are higher than the FE-calculated losses due to the position of the search coil over the winding coil, as has been shown with Figure 7.7.

In the yoke, the same difficulties as in the tooth tips appear. Indeed, as can be seen in Figure 7.7 and Figure 7.9.b, the flux density vector is not unidirectional and the flux-density distribution not uniform especially in the regions over the teeth (named "yoke1" and "yoke 3" in Figure 7.8). Some supplementary search coils would be required, if it is possible to wind any, in order to estimate accurately the losses in the yoke from the measurements, combined with iron losses models taking the rotational losses into account.

Estimating the iron losses from the measured flux-density waveforms is not possible except for the losses in the tooth bodies. However, the measured and FE-simulated flux-density waveforms agree well which shows that the iron losses calculated by the FE software should be reliable when comparing the losses between different load conditions and regions in the stator. The iron losses calculated with the FE software are presented in Figure 7.10.b. The total stator iron losses increase with

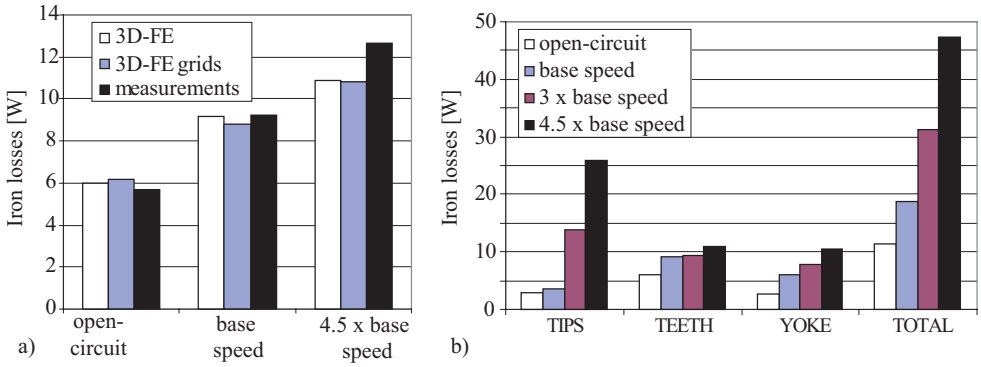

Figure 7.10: a) Iron losses in the teeth calculated from the FE software and from 3D-FE simulated or measured flux-density waveforms;
b) 3D-FE calculated iron losses at different load conditions.

the increasing speed under field-weakening operation. Usually, the iron losses are constant or decrease slightly for higher speeds under field-weakening operation because of the lower amplitude of the flux densities. This unexpected increase is mostly due to the losses in the tooth tips which represent more than 50 % of the total losses at 4.5 times the base speed. The high tooth tips losses are caused by the zigzag flux leakage as has been shown in Figure 7.7. The losses in the tooth bodies are rather constant, while they increase in the yoke. These losses, calculated from the FE software, can be compared to the directly measured motor losses. The difference between the input power and the sum of the output power and copper losses gives the stator and rotor iron losses and mechanical losses. Table 7.2 gives the 3D-FE calculated iron losses and the measured iron and mechanical losses. Unfortunately, it has not been possible to separate the mechanical losses and the iron losses. The large increase in the measured mechanical and iron losses under flux-weakening operation roughly agree with the increase of the FE calculated iron losses considering that the machine's rotating speed is rather low (<1000 rpm) and the losses in the ferrite magnets should be low. However, the 3D-FE calculated losses cannot be accurately validated. These losses may anyway certainly differ from the losses in the motor. Indeed, the loss data given by the steel manufacturer and used for the FE iron losses calculation do not take the punching and welding of the lamination into account, which deteriorate the magnetic properties of the material [104].

This study shows that for the considered PMSM, approximately half of the iron losses under field-weakening operation are due to the losses in the tooth tips. A PMSM designed with open slots and no tooth tips would therefore have much lower iron losses. The coils of a PMSM with open slot can also be placed much more

Table 7.2: FE-calculated iron losses and measured iron and mechanical losses.

	Base speed	3 x base speed	4.5 x base speed
FE-calculated iron losses [W]	19	31	47
Measured iron and mechanical losses [W]	30	70	112

easily which leads to a high slot fill factor. The decrease in the open-circuit airgap flux density can be compensated with a higher current loading without increasing the copper losses, as shown in Chapter 5, Section 5.2.3. However, opening the slots also decreases the d-axis inductance and thus worsens the field-weakening capability of the machine. A compromise can then be found at the design stage between the iron losses value in the tooth tips and the value of the d-axis inductance.

7.5 Conclusions

In this chapter, measurements of the magnetic flux variation in different parts of the prototype motor with surface-mounted PMs and non-overlapping windings are analyzed. Several flux waveforms are obtained from the measurement of the voltages across search coils placed in different parts of the stator. It is shown that the open-circuit measurements allow highlighting the zigzag flux flowing from one magnet to another through a tooth tip, which is characteristic of PMSMs with non-overlapping concentrated windings. With a blocked-rotor test, the slot-leakage and airgap component inductances could roughly be separated. Furthermore, the influence of the end-effect on the inductances is revealed by comparing the results from 2D and 3D-FE simulations. Finally, the possibility to use the measured flux-density waveforms for the calculation of the iron losses is investigated. The iron losses in the tooth bodies can be accurately estimated. However, the tooth tips and yoke are subject to rotational core losses and non-uniform flux-density distribution that are impossible to take into account from the performed measurements with search coils. Nevertheless, the 3D-FE calculated iron losses can be considered to be reliable enough for discussing the distribution of the losses in different parts of the stator, as the FE-calculated flux-density waveforms agree well with the measured ones. Especially, it is shown that the zigzag flux leakage flowing in the tooth tips causes high iron losses in the tooth tips that represent approximately 50 % of the stator iron losses under field weakening operation. In general, the measured and 3D-FE calculated flux-density waveforms agree well.

8 Conclusions and future work

8.1 Conclusions

Induction motors are commonly coupled to a gearbox when an application requires low speed and high torque. A gearbox is expensive, needs maintenance and decreases the efficiency of the drive. Therefore, it is very advantageous to remove the gearbox. The resulting direct drive can be achieved by using a PMSM running directly at low speed. A review of several industrial low-speed applications that successfully changed from a geared to a direct drive shows that different PM machine topologies are suitable, the most conventional being the radial-flux PMSM. In particular, radial-flux PMSMs with non-overlapping concentrated windings are very attractive in comparison to conventional PMSMs with distributed windings. Therefore, this thesis has focused on PMSMs with non-overlapping concentrated windings.

First, particular design features of PMSMs with concentrated windings have been presented. Particularly, it has been shown that the stator core manufacturing method, the number of winding layers, the combination of pole and slot numbers, and the geometry of the tooth tips should be chosen carefully.

Second, a PMSM for a low-speed direct-drive 4.5 kW waste-water treatment mixer has been designed. The most suitable PMSM for this application has an inner rotor with buried ferrite magnets and double-layer concentrated windings. However, mostly due to the over-sized non-active components of the drive as e.g. the seals and the housing, the designed direct-drive mixer could not compete with the existing geared mixer in terms of cost and weight. Furthermore, investigations revealed that manufacturing the stator of a PMSM with concentrated windings may not be as easy and inexpensive as expected. Therefore, the difficulties in manufacturing a stator core with concentrated windings have been investigated. Existing solutions have been compared in terms of cost, required production equipment, and performance of the motor.

Mostly due to economical aspects, no prototype motor has been built for the direct-drive mixer. However, a prototype motor designed for another low-speed direct-drive application was at disposal. This application requires a large constant-power speed range. Since the flux-weakening capability of the machine depends on its d-axis inductance, measurements of the inductances were conducted after having shown that dq theory can be applied to surface-mounted PMSMs with non-overlapping concentrated windings. Three methods to measure the inductances without position sensor have been implemented and compared. Two methods giving different results are based on a blocked-rotor test, while the third one is a novel method to determine the inductances from a load test without the knowledge of the rotor position. The discrepancies between the two blocked-rotor methods have been discussed. The results from the novel method performed at load conditions, from the first blocked-rotor test, and from FE simulations agree well.

Finally, additional measurements on the prototype motor have been presented. Especially, search coils placed in different parts of the stator allowed to indirectly measure the flux in the machine. The analysis of these measurements highlights the zigzag flux flowing from one magnet to another through a tooth tip, which is characteristic for PMSMs with non-overlapping concentrated windings. It has been shown that this zigzag flux leakage causes high iron losses in the tooth tips that represent around 50 % of the total stator iron losses under field weakening operation. The measurements allowed also a thorough validation of the 3D-FE model of the prototype motor. A 3D-FE model was required due to the shortness of the machine and the shorter axial length of the stator lamination stack compared to the rotor.

8.2 Future work

Several suggestions on possible future work are presented in the following:

- In the direct-drive mixer project, the cost and weight of the non-active mechanical parts of the mixer could be implemented as a function of their size in the optimization procedure, in order to calculate a new design of a PMSM. The new results may show if a PM motor with a larger axial length and smaller diameter, which is heavier and more expensive than the designed PM motor, would lead to a lighter and cheaper direct drive because of the smaller mechanical components. A prototype motor would be required to further continue the study, especially to check if the particular rotor with buried magnets can be built without major problems.
- The investigation on the manufacturing methods of the stator cores could be completed by adding some figures on the cost of the different methods, allowing

a better comparison between them. Moreover, replacing the laminated stator of the prototype machine by a stator in SMC could be investigated further.

- The new proposed method to measure the inductances at load conditions without position sensor could be tested on a PM machine equipped with a reliable position sensor. The d- and q-axes currents found with this method could then directly be compared with the known values.
- Additional investigations on the iron losses of PMSMs with concentrated windings could be performed. Analytical models to calculate the iron losses in the stator could be developed, following the recommendations made in Chapter 7. The analytical models and results from FE simulations could be validated by separating the measured mechanical losses to the iron losses.

During this thesis work, analytical and FE models have been implemented and validated with the measurements on a prototype motor. These analytical models are currently further implemented in a web-based version called Emetor [XI]. This web-based version is intended to anybody with knowledge on electrical machine design and especially to students. The concept of a design tool on the web offers a huge potential for further developments such as e.g. the improvement of the analytical models or the implementation of tutorials or user forums.

Bibliography

[1] D. Botting, "Power and productivity for a better world - Vision or reality?." Keynote presentation of the IET Int. Conf. on Power Electronics Machines and Drives (PEMD), 2008.

[2] J. Ikäheimo, "Permanent magnet motors eliminate gearboxes," in *ABB review no. 4, pp. 22-25*, 2002.

[3] T. Haring, K. Forsman, T. Huhtanen, and M. Zawadzki, "Direct drive - Opening a new era in many applications," in *Proc. of Pulp and Paper Industry Technical Conf., pp. 171-179*, 2003.

[4] J. Ribrant and L. Bertling, "Survey of failures in wind power systems with focus on Swedish wind power plants during 1997-2005," in *IEEE Trans. on Energy Conversion, vol. 22, no. 1, pp. 167-173*, 2007.

[5] C. Versteegh, "Design of the Zephyros Z72 wind turbine with emphasis on the direct drive PM generator," in *Proc. of Nordic Workshop on Power and Industrial Electronics (NORPIE)*, 2004.

[6] C. von Schultz, "Billig vindkraft i sikte," in *Ny teknik, (7), 14 February*, 2006.

[7] B. Chalmers, W. Wu, and E. Spooner, "An axial-flux permanent-magnet generator for a gearless wind energy system," in *IEEE Trans. on Energy Conversion, vol. 14, no. 2, pp. 251-257*, 1999.

[8] E. Muljadi, C. Butterfield, and Y. Wan, "Axial flux, modular, permanent-magnet generator with a toroidal winding for wind turbine applications," in *IEEE Trans. on Industry Applications, vol. 35, no. 4, pp. 831-836*, 1999.

[9] L. Söderlund, J. Eriksson, J. Salonen, H.Vihriälä, and R. Perälä, "A permanent-magnet generator for wind power applications," in *IEEE Trans. on Magnetics, vol. 32, no. 4, pp. 2389-2392*, 1996.

[10] H. Weh and H. May, "Achievable force densities for permanent magnet excited machines in new configurations," in *Proc. of Int. Conf. on Electrical Machines, (ICEM), vol. 3, pp. 1107-1111*, 1990.

[11] M. Dubois, N. Dehlinger, H. Polinder, and D. Massicotte, "Clawpole transverse-flux machine with hybrid stator," in *Proc. of Int. Conf. on Electrical Machines, (ICEM), paper no. 412*, 2006.

[12] D. Svechkarenko, "On analytical modeling and design of a novel transverse flux generator for offshore wind turbines." Licentiate thesis, Department of Electrical Machines and Power Electronics, Royal Institute of Technology, Stockholm, Sweden, 2007.

[13] Enercon, "www.enercon.se."

[14] D. Kane and M. Warburton, "Integration of permanent magnet motor technology," in *IEEE Power Engineering Society Summer Meeting, vol. 1, pp. 275-280*, 2002.

[15] F. Caricchi, F. Crescimbini, and O. Honorati, "Modular axial-flux permanent-magnet motor for ship propulsion drives," in *IEEE Trans. on Energy Conversion, vol. 14, no. 3, pp. 673-679*, 199.

[16] B. Bean, "Invasion of the Azipods: The first change to screws in 200 years causes quite a stir," in *The TRITON-Megayacht News, www.the-triton.com/megayachtnews/*, 2005.

[17] A. Mitcham, "Transverse flux motors for electric propulsion of ships," in *IEE Colloquium on New Topologies for Permanent Magnet Machines, Digest NORPIE 1997/090, pp. 3/1-3/6*, 1997.

[18] R. Lain and A. Bedford, "Recent developments in the design of gearless machines for elevators," in *Proc. of Int. Conf. on Electrical Machines and Drives, pp. 334-338*, 1993.

[19] H. Hakala, "Integration of motor and hoisting machine changes the elevator business," in *Proc. of Int. Conf. on Electrical Machines, (ICEM), vol. 3, pp. 1242-1245*, 2000.

[20] R. Ficheux, F. Caricchi, F. Crescimbini, and H. Onorato, "Axial-flux permanent-magnet motor for direct-drive elevator systems without machine room," in *IEEE Trans. on Industry Applications, vol. 37, no. 6, pp 1693-1701*, 2001.

[21] H. Lim and R. Krishnan, "Ropeless elevator with linear switched reluctance motor drive actuation systems," in *IEEE Trans. on Industrial Electronics, vol. 54, no. 4, pp. 2209-2218*, 2007.

[22] Kone, "www.kone.com."

[23] A. Bianchi and L. Buti, "Three-Phase A.C. Motor Drive and Controller for Clothes Washers," in *Int. Appliance Technical Conference, available on www.appliancemagazine.com*, 2003.

[24] LG Electronics, "www.lge.com."

[25] J. Ikäheimo, "Permanent magnet motors eliminate gearboxes," in *ABB review, April pp. 22-25*, 2002.

[26] S. Evon and R. Schiferl, "Direct-drive induction motors: using an induction motor as an alternative to a motor with reducer," in *IEEE Industry Application Magazine, vol. 11, no. 4, pp. 45-51*, 2005.

[27] P. Salminen, "Fractional slot permanent magnet synchronous motors for low speed applications." Doctoral thesis, Lappeenranta University of Technology, Finland, 2004.

[28] A. Holzknecht, "Torque motors do the trick," in *machinedesign.com*, 2003.

[29] ITT Water & Wastewater, "www.flygt.se."

[30] J. Johansson and J. Lazarevic, "Hydrauliskt drivna omrörare." Master thesis, Royal Institute of Technology, Stockholm, Sweden, 2003.

[31] J. Hallberg, "Conceptual evaluation and design of a direct-driven mixer." Master thesis, Department of Mechanical Engineering, Linköpings University, Linköping, Sweden, 2005.

[32] Discussion with professor H.P. Nee, Royal Institute of Technology, Sweden, 2008.

[33] M. Mueller, A. McDonald, and D. Macpherson, "Structural analysis of low-speed axial-flux permanent-magnet machines," in *IEE Proc. on Electric Power Application, vol. 152, no. 6, pp. 1417-1426*, 2005.

[34] M. Cistelecan, M. Popescu, and M. Popescu, "Study of the number of slots/pole combinations for low speed permanent magnet synchronous generators," in *Proc. of IEEE Int. Electric Machines and Drives Conf., (IEMDC), vol. 2, pp. 1616-1620*, 2007.

[35] J. Germishuizen, "Design and performance characteristics of IPM machines with single layer non-overlapping concentrated windings," in *Proc. of IEEE Industry Applications Society Conf., pp. 141-147*, 2007.

[36] J. Cros and P. Viarouge, "Synthesis of high performance PM motors with concentrated windings," in *IEEE Trans. on Energy Conversion, vol. 17, no. 2, pp. 248-253*, 2002.

[37] F. Magnussen and C. Sadarangani, "Winding factors and joule losses of permanent magnet machines with concentrated windings," in *Proc. of Electric Machines and Drives Conf., (IEMDC), vol. 1, pp. 333-339*, 2003.

[38] R. Wrobel and P. Mellor, "Design considerations of a direct drive brushless machine with concentrated windings," in *IEEE Trans. on Energy Conversion, vol. 23, no. 1, pp. 1-8*, 2008.

[39] A. EL-Refaie, "High speed operation of permanent magnet machines." Doctoral thesis, University of Wisconsin-Madison, USA, 2005.

[40] M. Cistelecan, B. Cosan, and M. Popescu, "Tooth Concentrated Fractional Windings for low speed three phase a.c. machines," in *Proc. of Int. Conf. on Electrical Machines, (ICEM), paper no. 362*, 2006.

[41] A. Rix, M. Kamper, and R. Wang, "Design and performance evaluation of concentrated coil permanent magnet machines for in-wheel drives," in *Proc. of IEEE Int. Electric Machines and Drives Conf., (IEMDC), vol. 1 pp. 770-775*, 2007.

[42] P. Salminen, M. Niemelä, and J. Pyrhönen, "Performance analysis of fractional slot wound PM-motors for low speed applications," in *Proc. of IEEE Industry Applications Society Conf., vol. 2, pp. 1032-1037*, 2005.

[43] N. Bianchi, S. Bolognani, and M. D. Pré, "Magnetic loading of fractional-slot three-phase PM motors with non-overlapped coils," in *Proc. of IEEE Industry Applications Society Conf., vol. 1, pp. 37-43*, 2006.

[44] A. EL-Refaie, M. Shah, and J. K. R. Qu, "Effect of number of phases on losses in conducting sleeves of high speed surface PM machines rotors," in *Proc. of IEEE Industry Applications Society Conf., pp. 1522-1529*, 2007.

[45] J. Wang, K. Atallah, Z. Zhu, and D. Howe, "Modular 3-phase permanent magnet brushless machines for in-wheel applications," in *IEEE Trans. on Vehicular Technology : Accepted for future publication*, 2008.

[46] F. Magnussen and H. Lendenmann, "Parasitic effects in PM machines with concentrated windings," in *IEEE Trans. on Industry Applications, vol. 43, no. 5, pp. 1223-1232*, 2007.

[47] N. Bianchi, S. Bolognani, M. D. Pré, and G. Grezzani, "Design considerations for fractional-slot winding configurations of synchronous machines," in *IEEE Trans. on Industry Applications, vol. 42, no. 4, pp. 997-1006*, 2006.

[48] D. Ishak, Z. Zhu, and D. Howe, "Comparison of PM brushless motors, having either all teeth or alternate teeth wound," in *IEEE Trans. on Energy Conversion, vol. 21, no. 1, pp. 95-103*, 2006.

[49] D. Ishak, Z. Zhu, and D. Howe, "Eddy-curent loss in the rotor magnets of permanent-magnet brushless machines having a fractional number of slots per pole," in *IEEE Trans. on Magnetics, vol. 41, no. 9, pp. 2462-2469*, 2005.

[50] D. Ishak, Z. Zhu, and D. Howe, "Permanent magnet brushless machines with unequal tooth widths and similar slot and pole numbers," in *IEEE Trans. on Industry Applications, vol. 41, no. 2, pp. 584-590*, 2005.

[51] N. Bianchi and M. D. Pré, "Use of the star of slots in designing fractional-slot single-layer synchronous motors," in *IEE Proc. on Electric Power Applications, vol. 153, no. 3, pp. 459-466*, 2006.

[52] S. Skaar, O. K. vel, and R. Nilssen, "Distribution, coil-span and winding factors for AFPM with concentrated windings," in *Proc. of Int. Conf. on Electrical Machines, (ICEM), paper no. 346*, 2006.

[53] L. Wang, J. Shen, Y. Wang, and K. Wang, "A novel magnetic-geared outer-rotor permanent-magnet brushless motor," in *Proc. of IET Int. Conf. on Power Electronics, Machines and Drives (PEMD), pp. 33-36*, 2008.

[54] K. Maliti and C. Sadarangani, "Modelling magnetic noise in induction machines," in *Proc. of IEE* 8^{th} *International Conference on Electrical Machines and Drives, (EMD)*, 1997.

[55] D. Ishak, Z. Zhu, and D. Howe, "Unbalanced magnetic forces in permanent magnet brushless machines with diametrically asymmetric phase windings," in *Proc. of IEEE Industry Applications Society Conf., vol. 2, pp. 1037-1043*, 2005.

[56] U. Hoefer, A. Jack, and B. Mecrow, "Unbalanced magnetic pull in high-speed brushless permanent magnet motors - experimental observations and results," in *Proc. of Int. Conf. on Electrical Machines, (ICEM), paper no. 426*, 2006.

[57] J. Wang, Z. Xia, and D. Howe, "Comparison of vibration characteristics of 3-phase permanent magnet machines with concentrated, distributed and modular windings," in *Proc. of Int. Conf. on Electrical Machines, (ICEM), paper no. 131*, 2006.

[58] J. Wang, Z. Xia, D. Howe, and S. Long, "Vibration characteristics of modular permanent magnet brushless AC machines," in *Proc. of IEEE Industry Applications Society Conf., vol. 3, pp. 1501-1506*, 2006.

[59] J. Wang, Z. Xia, S. Long, and D. Howe, "Radial force density and vibration characteristics of modular permanent magnet brushless AC machine," in *IET Proc. on Electric Power Applications, vol. 153, no. 6, pp. 793-801*, 2006.

[60] J. Hsu, B. Scoggins, M. Scudiere, L. Marlino, D. Adams, and P. Pillay, "Nature and assessments of torque ripples of permanent-magnet adjustable-speed motors," in *Proc. of IEEE Industry Applications Society Conf., pp. 2696-2702*, 1995.

[61] Z. Zhu and D. Howe, "Influence of design parameters on cogging torque in permanent magnet machines," in *IEEE Trans. on Energy Conversion, vol. 15, no. 4, pp. 407-412*, 2000.

[62] T. Jahns and W. Soong, "Pulsating torque minimization techniques for permanent magnet AC motor drives - A review," in *IEEE Trans. on Industrial Electronics, vol. 43, no. 2, pp. 321-330*, 1996.

[63] Z. Zhu and D. Howe, "Analytical prediction of the cogging torque in radial-field permanent magnet brussless motors," in *IEEE Trans. on Magnetics, vol. 28, no. 2, pp. 1371-1374*, 1992.

[64] S. Huang, M. Aydin, and T. Lipo, "Comparison of (nonslotted and slotted) surface mounted PM motors and axial flux motors for submarine ship drives," in *Proc. of 3^{rd} Naval Symposium on Electrical Machines, Online, Available: http://www.mipsis.com/mds/pdf/navy00.pdf*, 2000.

[65] Z. Zhu, D. Howe, and C. Chan, "Improved analytical model for predicting the magnetic field distribution in brushless permanent-magnet machines," in *IEEE Trans. on Magnetics, vol. 38, no. 1, pp. 229-238*, 2002.

[66] Z. Zhu and D. Howe, "Instantaneous magnetic field distribution in brushless permanent magnet dc motors, Part III: Effect of stator slotting," in *IEEE Trans. on Magnetics, vol. 29, no. 1, pp. 143-151*, 1993.

[67] P. Salminen, J. Mantere, J. Pyrhönen, and M. Niemelä, "Performance analysis of fractional slot wound PM-motors," in *Proc. of Int. Conf. on Electrical Machines, (ICEM), paper no. 509*, 2004.

[68] A. EL-Refaie, T. Jahns, and D. Novotny, "Analysis of surface permanent magnet machines with fractional-slot concentrated windings," in *IEEE Trans. on Energy Conversion, vol. 21, no. 1*, 2006.

[69] M. Nakano, H.Kometani, and M. Kawamura, "A study on eddy-current losses in rotors of surface permanent magnet synchronous machines," in *Proc. of IEEE Industry Applications Society Conf., vol. 3, pp. 1696-1702*, 2004.

[70] N. Bianchi, S. Bolognani, and E. Fornasiero, "A general approach to determine the rotor losses in three-phase fractional-slot PM machines," in *Proc. of Electric Machines and Drives Conf., (IEMDC), vol. 1, pp. 634-641*, 2007.

[71] J. Ede, K. Atallah, G. Jewell, J. Wang, and D. Howe, "Effect of axial segmentation of permanent magnets on rotor loss of modular brushless machines," in *Proc. of IEEE Industry Applications Society Conf., vol. 3, pp. 1703-1708*, 2004.

[72] K. Atallah, D. Howe, P. Mellor, and D. Stone, "Rotor loss in permanent-magnet brushless AC machines," in *IEEE Trans. on Industry Applications, vol. 36, no. 6, pp. 1612-1618*, 2000.

[73] A. EL-Refaie and T. Jahns, "Comparison of synchronous PM machine types for wide constant-power speed range operation," in *Proc. of IEEE Industry Applications Society Conf., vol. 2, pp. 1015-1022*, 2005.

[74] A. EL-Refaie and T. Jahns, "Impact of winding layer number and magnet type on synchronous surface PM machines designed for wide constant-power speed range operation," in *IEEE Trans. on Energy Conversion, vol., no. 1, pp. 53-60*, 2008.

[75] M. Voigt, "Magnets, magnetization and magnetic measurement - Sura Magnets." Seminar at the Royal Institute of Technology, 2004.

[76] C. Deak, A. Binder, and K. Magyari, "Magnet loss analysis of permanent-magnet synchronous motors with concentrated windings," in *Proc. of Int. Conf. on Electrical Machines, (ICEM), paper no. 457*, 2006.

[77] Z. Zhu, K. Ng, N. Schofield, and D. Howe, "Improved analytical modelling of rotor eddy current loss in brushless machines equipped with surface-mounted permanent magnets," in *IEE Proc. on Electric Power Applications, vol. 151, no. 6, pp. 641-650*, 2004.

[78] W. Soong and T. Miller, "Field weakening performance of brushless synchronous AC motor drives," in *IEE Proc. on Electric Power Applications, vol. 141, no. 6, pp. 331-340*, 1994.

[79] F. Magnussen, P. Thelin, and C. Sadarangani, "Performance evaluation of permanent magnet synchronous machines with concentrated and distributed windings including the effect of field-weakening," in *Proc. of IEE Int. Conf. on Power Electronics and Electrical Machines, (PEMD), vol.2, pp. 679-685*, 2004.

[80] A. EL-Refaie and T. Jahns, "Optimal flux weakening in surface PM machines using concentrated windings," in *IEEE Trans. on Industry Applications, vol. 41, no. 3, pp. 790-800*, 2004.

[81] A. EL-Refaie and T. Jahns, "Scalability of surface PM machines with concentrated windings designed to achieve wide speed ranges of constant-power operation," in *IEEE Trans. on Energy Conversion, vol. 21, no. 2, pp. 362-369*, 2005.

[82] A. EL-Refaie, T. Jahns, P. McCleer, and J. McKeever, "Experimental verification of optimal flux weakening in surface PM machines using concentrated windings," in *IEEE Trans. on Industry Applications, vol. 42, no. 2, pp. 443-453*, 2006.

[83] S. O. Kwon, S. I. Kim, and J. P. Hong, "Comparison of IPMSM with distributed and concentrated windings," in *Proc. of Int. Conf. on Electrical Machines, (ICEM), paper no. 635*, 2006.

[84] E. Lovelace, T. Jahns, T. K. Jackson Wai, J. Lang, D. D. Wentzloff, F. Leonardi, and J. Miller, "Design and experimental verification of a direct-drive interior PM synchronous machine using a saturable lumped-parameter model," in *Proc. of IEEE Industry Applications Society Conf., vol. 4, pp. 2486-2492*, 2002.

[85] W. Soong, P. Reddy, A. EL-Refaie, T. Jahns, and N. Ertugrul, "Surface PM machine parameter selection for wide field-weakening applications," in *Proc. of IEEE Industry Applications Society Conf., pp. 882-889*, 2007.

[86] A. Mitcham, G. Antonopoulos, and J. Cullen, "Favourable slot and pole number combinations for fault-tolerant PM machines," in *IEE Proc. on Electric Power Applications, vol. 151, no. 5, pp. 520-525*, 2004.

[87] Z. Zhu and D. Howe, "Instantaneous magnetic field distribution in brushless permanent magnet dc motors, part I: open-circuit field," in *IEEE Trans. on Magnetics, vol. 38, no. 1, pp. 124-135*, 1993.

[88] Z. Zhu and D. Howe, "Instantaneous magnetic field distribution in brushless permanent magnet dc motors, part II: armature-reaction field," in *IEEE Trans. on Magnetics, vol. 38, no. 1, pp. 136-142*, 1993.

[89] A. Proca, A. Keyhani, A. EL-Antably, W. Lu, and M. Dai, "Analytical model for permanent magnet motors with surface mounted magnets," in *IEEE Trans. on Energy Conversion, vol. 18, no. 3, pp. 386-391*, 1993.

[90] Z. Zhu, D. Howe, and J. Mitchell, "Magnetic field analysis and inductances of brushless DC machines with surface-mounted magnets and non-overlapping stator windings," in *IEEE Trans. on Magnetics, vol. 31, no. 3*, 1995.

[91] Z. Zhu and D. Howe, "Winding inductance of brushless machines with surface-mounted magnets," in *Proc. of IEEE Int. Electric Machines and Drives Conf., pp. WB2/2.1-WB2/2.3*, 1997.

[92] F. Magnussen, "On design and analysis of synchronous permanent magnet machines for field-weakening operation in hybrid electric vehicles." Doctoral thesis, Royal Institute of Technology, Stockholm, Sweden, 2004.

[93] F. Tourkhani and P. Viarouge, "Accurate analytical model of winding losses in round Litz wire windings," in *IEEE Trans. on Magnetics, vol. 37, no. 1, pp. 538-543*, 2001.

[94] H. Polinder, M. Hoeijmakers, and M. Scuotto, "Eddy-Current Losses in the Solid Back-Iron of PM Machines for different Concentrated Fractional Pitch Windings," in *Proc. of IEEE Int. Electric Machines and Drives Conf., (IEMDC), vol. 1, pp. 652-657*, 2007.

[95] A. Jack, C. Mecrow, P. Dickinson, D. Stephenson, J. Burdess, N. Fawcett, and J. Evans, "Permanent-magnet machines with powdered iron cores and prepressed windings," in *IEEE Trans. on Industry Applications, vol. 36, no. 4, pp. 1077-1084*, 2000.

[96] F. Magnussen, D. Svechkarenko, P. Thelin, and C. Sadarangani, "Analysis of a PM machine with concentrated fractional pitch windings," in *Nordic Workshop on Power and Industrial Electronics, (NORPIE)*, 2004.

[97] J. Wang, Z. Xia, and D. Howe, "Three-phase modular permanent magnet brushless machine for torque boosting on a downsized ICE vehicle," in *IEEE Trans. on Vehicular Technology, vol. 54, no. 3, pp. 809-816*, 2005.

[98] A. Muetze, A. Jack, and B. Mecrow, "Alternate designs of low cost brushless-DC motors using soft magnetic composites," in *Proc. of Int. Conf. on Electrical Machines, (ICEM), paper no. 237*, 2002.

[99] J. Chen, C. Nayar, and L. Xu, "Design and finite-element analysis of an outer-rotor permanent-magnet generator for directly coupled wind turbines," in *IEEE Trans. on Magnetics, vol. 36, no. 5, pp. 3802-3809*, 2000.

[100] K. Kim and J. Lee, "The dynamic analysis of a spoke-type permanent magnet generator with large overhang," in *IEEE Trans. on Magnetics, vol. 41, no. 10, pp. 3805-3807*, 2005.

[101] Discussion with sale agent Tommy Andersson from Sura Magnets. www.suramagnets.se, 2008.

[102] C. Sadarangani, "Design and analysis of induction and permanent magnet motors." Book, Royal Institute of Technology, Stockholm, ISBN 91-7170-627-5, 2000.

[103] Catalogue from Sura Magnets, www.suramagnets.se.

[104] W. Arshad, T. Ryckebush, F. Magnussen, H. Lendenmann, J. Soulard, B. Eriksson, and B. Malmros, "Incorporating lamination processing and component manufacturing in electrical machine design tools," in *Proc. of IEEE Industry Applications Society Conf., pp. 94-102*, 2007.

[105] T. Mitsuhiro, A. Hiroshi, D. Noriyuki, and O. Izumi, "Manufacture of spiral lamination core." Patent JP2231943, 1990.

[106] A. Yasuo and F. Toshihiko, "Method and apparatus for rolling up stator core." Patent JP2004159417, 2004.

[107] T. Mitsuhiro, "Manufacturing device for spiral laminated core." Patent JP1148046, 1989.

[108] S. Lee, "Laminated body of motor and manufacturing method thereof." United States Patent Application 20050073211, 2005.

[109] H. Akita, Y. Nakahara, N. Miyake, and T. Oikawa, "New core structure and manufacturing method for high efficiency of permanent magnet motors," in *Proc. of IEEE Industry Applications Society Conf., vol. 1, pp. 367-372*, 2003.

[110] K. Takahiro and K. Mototeru, "Stator of electric motor." Patent JP2000139052, 2000.

[111] W. Sami, I. Ilkka, P. Matti, and A. Jiri, "Segmented stator and the winding of it." European Patent EP1382107, 2004.

[112] B. Mecrow, A. Jack, J. Haylock, U. Hoefer, and P. Dickinson, "Simplifying the manufacturing process for electrical machines," in *Proc. of Int. Conf. on Power Electronics, Machines and Drives (PEMD), vol. 1, pp. 169-174*, 2004.

[113] T. Yamada, T. Kawamara, N. Mizutani, T. Sato, K. Miyaoka, and M. Mochizuki, "Stator for dynamoelectric machine and method for making the same." European patent application, EP 0871282, 1998.

[114] T. Miller, M. Popescuand, C. Cossar, and M. McGilp, "Computation of the voltage-driven flux-MMF diagram for saturated PM brushless motors," in *Proc. of IEEE Industry Applications Society Conf., vol. 2, pp. 1023-1028*, 2005.

[115] P. Barret, "Les cours de l'Ecoles Supérieure d'Electricité - Régimes transitoires des machines tournantes électriques." Book, Eyrolles second edition, 1987.

[116] J. Wang, Z. Xia, and D. Howe, "Analysis of three-phase surface-mounted magnet modular permanent magnet machines," in *Proc. of IEE Int. Conf. on Power Electronics and Electrical Machines, (PEMD)*, 2004.

[117] V. Petrovic and A. Stankovic, "Modeling of PM synchronous motors for control and estimation tasks," in *Proc. of IEEE Conf. on Decision and Control, vol. 3, pp. 2229-2234*, 2001.

[118] D. Pavlik, V. Garg, J. Repp, and J. Weiss, "A finite element technique for calculating the magnet sizes and inductances of permanent magnet machines," in *IEEE Trans. on Energy Conversion ,vol. 3, no. 1, pp. 116-122*, 1988.

[119] N. Demerdash, F. Fouad, and T. Nehl, "Determination of winding inductances in ferrite type permanent magnet electric machinery by finite element," in *IEEE Trans. on Magnetics, vol. 18, no. 6, pp. 1052-1054*, 1982.

[120] N. Demerdash and T. Nehl, "Electric machinery parameters and torques by current and energy perturbations from field computations - Part I: Theory and formulation," in *IEEE Trans. on Energy Conversion, vol. 14, no. 4, pp. 1507-1513*, 1999.

[121] N. Bianchi and S. Bolognani, "Magnetic models of saturated interior permanent magnet motors based on finite element analysis," in *Proc. of IEEE Industry Applications Society Conf., vol. 1, pp. 27-34*, 1998.

[122] M. Rahman and P. Zhou, "Determination of saturated parameters of PM motors using loading magnetic fields," in *IEEE Trans. on Magnetics, vol. 27, no. 5, pp. 3947-3950*, 1991.

[123] H. Jianhui, Z. Jibin, and L. Weiyan, "Finite element calculation of the saturation DQ-axes inductance for a direct-drive PM synchronous motor considering cross-magnetization," in *Proc. of Int. Conf. on Power Electronics and Drive Systems, (PEDS), vol. 1, pp. 677-681*, 2003.

[124] B. Stumberger, B. Kreca, and B. Hribernik, "Determination of parameters of synchronous motor with permanent magnets from measurement of load conditions," in *IEEE Trans. on Energy Conversion, vol. 14, no. 4, pp. 1413-1416*, 1999.

[125] R. Dutta and M. Rahman, "A comparative analysis of two test methods of measuring *d*- and *q*-axes inductances of interior permanent-magnet machine," in *IEEE Trans. on Magnetics, vol. 42, no. 11, pp. 3712-3718*, 200.

[126] P. Mellor, F. Chaaban, and K. Binns, "Estimation of parameters and performance of rare-earth permanent-magnet motors avoiding measurements of load angle," in *IEE Proc. on Electric Power Applications, vol. 138, no. 6, pp. 322-330*, 1991.

[127] K. Rahman and S. Hiti, "Identification of machine parameters of a synchronous motor," in *IEEE Trans. on Industry Applications, vol. 41, no. 2, pp. 557-565*, 2005.

[128] H.-P. Nee, L. Lefevre, P. Thelin, and J. Soulard, "Determination of d and q reactances of permanent-magnet synchronous motors without measurements of the rotor position," in *IEEE Trans. on Industry Applications, vol. 36, no. 5, pp. 1330-1335*, 2000.

[129] T. Miller, M. Popescu, C. Cossar, M. McGilp, and J. Walker, "Calculating the interior permanent-magnet motor," in *Proc. of IEEE Int. Electric Machines and Drives Conf., (IEMDC), vol. 2, pp. 1181-1187*, 2003.

[130] R. Qu and T. Lipo, "Analysis and modeling of air-gap and zigzag leakage fluxes in a surface-mounted permanent-magnet machine," in *IEEE Trans. on Industry Applications, vol. 40, no. 1, pp. 121-127*, 2004.

[131] V. Zivotic-Kukolj, W. Soong, and N. Ertugrul, "Iron Loss Reduction in an Interior PM Automotive Alternator," in *IEEE Trans. on Industry Applications, vol. 42, no. 6, pp. 1478-1486*, 2006.

[132] S. Calverley, G. Jewell, and R. Saunders, "Prediction and measurements of core losses in a high-speed switched-reluctance machine," in *IEEE Trans. on Magnetics, vol. 41, no. 11*, 2005.

[133] Manual of the FE software Flux from Cedrat.

[134] K. Sitapati and R. Krishnan, "Performance Comparisons of Radial and Axial Field, Permanent-Magnet, Brushless Machines," in *IEEE Trans. on Industry Applications, vol. 37, no. 5*, 2001.

[135] M. Say, "The performance and design of alternating current machines." Book, Pitman, ISBN 999-184258-6, 1948.

Glossary of symbols and acronyms

Symbols

B	flux density	[T]
B	Park transformation matrix (Chapter 6)	-
B_δ	fundamental open-circuit airgap flux density	[T]
B_n	radial component of the airgap flux density	[T]
B_t	tangential component of the airgap flux density	[T]
B_m	peak value of the flux density	[T]
B_r	remanence flux density of the PM	[T]
d	denominator of q	-
d	lamination thickness (eq. (7.2))	[m]
D	inner stator diameter	[m]
E	induced voltage	[V]
$\overrightarrow{E_i}$	EMF phasor of conductor i	[V]
E_0	fundamental back-EMF	[V]
E_{magn}	stored magnetic energy	[J]
E_n	n^{th} harmonic component of the phase back-EMF (eq. (3.8))	[V]
f	frequency	[Hz]
H_m	coercive magnetic field intensity of the PM	[A/m]
i	phase current	[A]
i_f	current in a winding modelling the PM	[A]
I	amplitude of the current	[A]
I_{ch}	characteristic current	[A]
I_r	rated current	[A]
I_d	d-axis current	[A]
I_q	q-axis current	[A]
k	integer 1, 2, 3...	-
k_C	Carter factor	-
k_h	hysteresis coefficient	[W.s/T^2/m^3]
k_e	coefficient of excess loss	[W.(s/T)$^{3/2}$/m^3]
k_f	stacking factor	-

k_{wn}	n^{th} harmonic component of winding factor	-
L	active length	[m]
L	inductance	[H]
L_a	self-inductance of phase a	[H]
L_d	d-axis inductance	[H]
$\mathcal{L}$	self-inductance varying with θ	[H]
l_m	PM thickness	[m]
$\mathcal{M}$	mutual inductance varying with θ	[H]
m	number of phases	-
n	rotational speed	[rpm]
n	integer 1, 2, 3...	-
n_l	number of layers of the winding	-
n_u	numerator of q	-
p	number of poles	-
P_{in}	input power	[W]
P_{out}	output power	[W]
P_{cu}	copper losses	[W]
P_{iron}	iron losses	[W]
q	number of slots per pole per phase	-
Q	reactive power	[VAR]
Q_s	number of stator slots	-
R	resistance of one phase of the stator winding	[Ω]
$\Re$	reluctance	[At/Wb]
S	vector describing a sequence of conductors of phase A	-
S_1	fundamental current loading	[A/m]
t	time	[s]
T	torque	[Nm]
T	period (eq. (7.2))	[s]
T_{cog}	cogging torque	[Nm]
T_{loss}	"loss" torque	[Nm]
T_{mean}	mean value of the torque	[Nm]
T_{rip}	torque ripple	[p.u.]
u	voltage	[V]
V	supplied phase voltage	[V]
v	volume	[m^3]
W	magnetic energy	[J]
w_m	PM length	[m]
X	machine periodicity	-
X'	number of symmetries in the winding layout without conductors orientation	-

Greek symbols

α	magnet angle	[rad]
β	angle between the d-axis and the current vector	[rad]
δ	airgap length	[mm]
δ	load angle	[rad]
γ	angle between the line current and back-EMF	[rad]
μ_0	magnetic permeability of free space ($4\pi.10^{-7}$)	[H/m]
μ_r	relative magnet permeability	-
ϕ	angle between phase current and phase voltage	[rad]
ψ_a	flux seen by phase a	[Wb]
Ψ_m	magnet flux linkage	[Wb]
σ	material conductivity (eq. (7.2))	[Ωm^{-1}]
σ	radial magnetic force density (eq. (3.7))	[N/m^2]
θ	angular position	[rad]
ω	electrical angular frequency	[Hz]
Ω	rotor speed	[rad/s]

Subscripts

a	phase a
b	phase b
c	phase c
d	direct-axis component
f	PM component (Chapter 6)
q	quadrature-axis component

Acronyms and abbreviations

an.	analytical
AC	alternative current
AFPM	axial-flux permanent magnet
app.	appendix
BLDC	brushless DC
bur.	buried
CW	concentrated windings
d-	direct
DC	direct current
deg	degree

DFIG	doubly-fed induction generator
DW	distributed windings
elec.	electrical
EMF	electro-motive force
e.w.	end-windings
FE	finite element
GCD	greatest common divisor
HPD	High Performance Electrical Machines and Drives
ind.	inductance
int.	international
KTH	Royal Institute of Technology
LCM	least common multiple
mech.	mechanical
Meas.	measurements
MMF	magneto-motive force
nb	number
NdFeB	neodymium iron boron
neg.	negative
pos.	positive
Proc.	Proceedings
PWM	pulse width modulation
ref.	reference
RFPM	radial-flux permanent magnet
RMS	root mean square value
SMC	soft magnetic composites
SMPM	surface-mounted permanent magnet
surf.	surface
TFPM	transverse-flux permanent magnet
Trans.	Transaction
PM	permanent magnet
PMSM	permanent-magnet synchronous machine
pp.	page
p.u.	per unit
q-	quadrature
vol.	volume
weak.	weakening
2D	two-dimensional
3D	three-dimensional

A PM machine topologies

A.1 Radial-flux PM machines

RFPM synchronous machines are the most conventional PM machines. Figure A.1 shows two views of a RFPM machine with the direction of the flux and current. The flux flows radially through the airgap of the machine while the current circulates in the axial direction.

RFPM machines are the easiest and cheapest to manufacture among the PM machines. However, they are much larger than the axial-flux and transverse-flux machines in terms of active weight and axial length [134]. Different rotor configurations of RFPM machines are shown in Figure A.2.

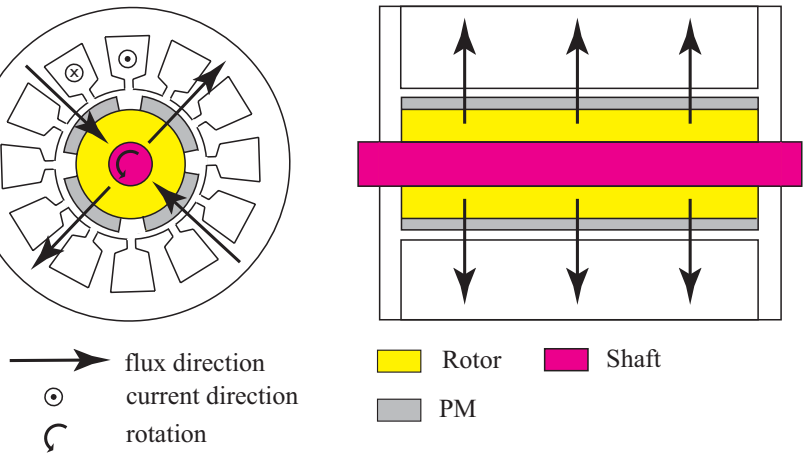

Figure A.1: RFPM machine with flux and current directions.

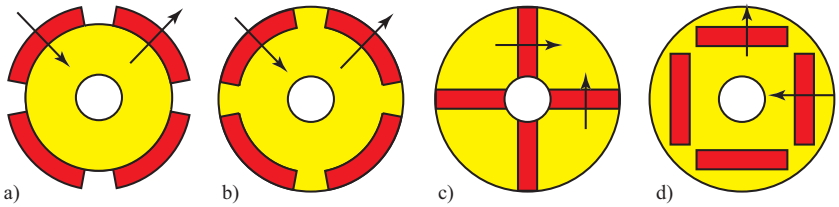

Figure A.2: Rotor configurations:
a) Surface-mounted PM; b) Inset PM; c) Tangentially-magnetized buried PM; d) Radially magnetized buried PM.

A.2 Axial-flux PM machines

AFPM machines feature a large diameter and a relatively short axial length compared to RFPM machines. As suggested by its name and Figure A.3, the flux flows axially through the airgap while the current flows in the radial direction.

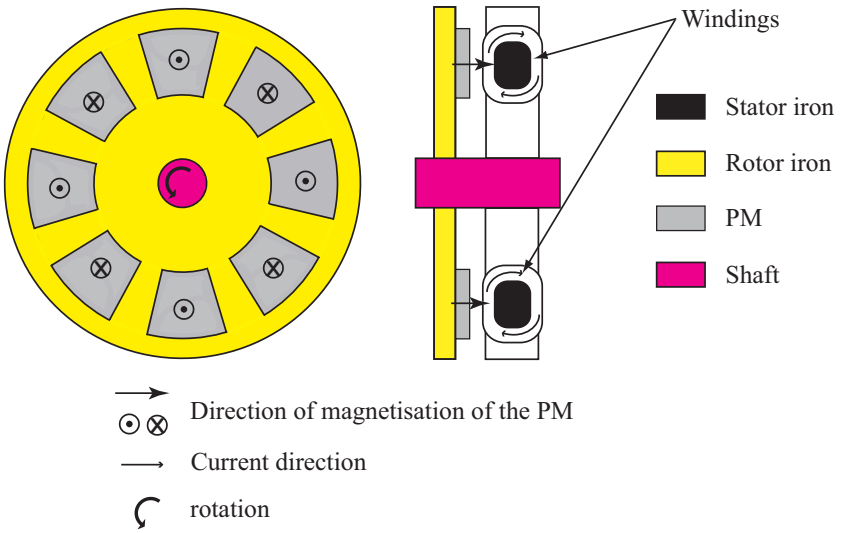

Figure A.3: AFPM machine with flux and current directions.

A.3 Transverse-flux PM machines

The basic arrangement of a TFPM machine is shown in Figure A.4. This type of machine suits well for low-speed direct-drive applications because of a small pole pitch. Nevertheless, it is not very common yet.

The advantage of the TFPM machine is the high specific torque that allows the compactness of the machine. The major drawbacks are the poor power factor at high specific torque and the complexity of the structure which leads to high manufacturing cost.

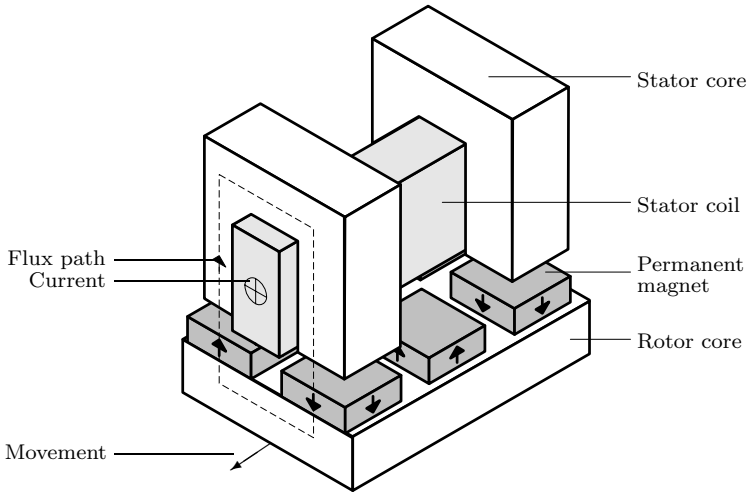

Figure A.4: Basic single-phase transverse flux topology with permanent-magnet excitation [12].

B Methods to find the winding layout of concentrated windings

In this appendix, two different methods to find the winding layout that gives the highest winding factor are presented.

B.1 Winding layout from Cros' method

This method proposed in [36] is based on the decomposition of the number of slots per pole per phase q. It is similar to the method used for the large synchronous machines with a fractional value of q [135]. The method is illustrated in Figure B.1 using $Q_s = 24$ and $p = 28$ and a double-layer winding as an example.

a) The number of slots per pole per phase q is written as a fraction which is cancelled down to its lowest terms: $q = n_u/d = 2/7$ where n_u and d are integers.

b) A sequence of $d - n_u = 5$ zeros ("0") and $n_u = 2$ ones ("1") is found, the ones being distributed in the sequence as regularly as possible.

c) The found sequence is repeated $3p/d = Q_s/n_u = 12$ times. It is compared to the layout of the distributed winding with $3p$ slots and $q = 1$.

d) Those conductors from the distributed winding that correspond to the "1" are kept and form one layer of the double-layer concentrated winding. The second winding layer is obtained by writing the corresponding return conductor on the other side of the tooth for every obtained conductor, i.e. A' for A.

e) A vector S is written to describe the layout of phase A. It will be used to calculate the winding factor. Thereby, the slots are numbered from 1 to Q_s. The vector S consists of the numbers corresponding to these slots that contain conductors of the phase A. If both layers of one slot contain conductors of phase A, the number of the slot is written twice in the vector. S has thus $2Q_s/3$ elements. For conductors A', a minus is added to the corresponding slot number.

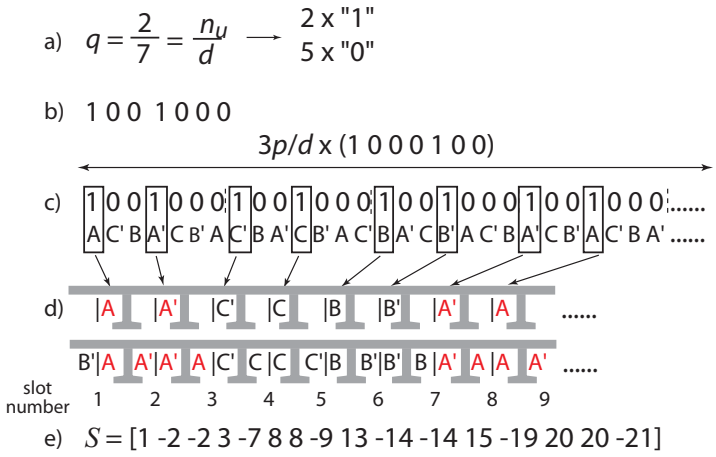

Figure B.1: Determination of the winding layout for Q_s=24 and $p = 28$.

The layout for the single layer winding can be found from step d). The single layer winding layout for the 24-slot 28-pole is simply $A|A'|C'|C|B|B'|A'|A|C|C'|B'|B...$

For other cases, such as when $Q_s = 18$ and $p = 14$, the layout cannot be found applying the described method. The layout that gives the highest winding factor for this combination of slot and pole numbers is indeed $A|A|C|C|A|A|C|C|B|B|C|C|B|B|A|A|B|B$.

B.2 Winding layout from the star of slot

The winding layout can also be found by using the star of slots [51]. The method is fully described by Bianchi in [51] for different cases. "The star of slot is the phasor representation of the main EMF harmonic induced in the coil side of each slot", [51]. The method described in Section 3.2.3 is thus related to the star of slot. The winding layout for single-layer windings can be found in any of the possible cases with the star of slot.

The star of slot is constituted of $Q_s/\text{GCD}(Q_s,p/2)$ spokes. The angle between the phasors of two consecutive slots is $\pi p/Q_s$ in electrical radians. Two opposite sectors covering π/m radians (m is the number of phases) are plotted on the star of slots. The phasors inside the sectors are those belonging to a same phase. The phasors in the opposite sector give the slots containing the coil sides with negative polarity. From this star of slot, the winding layout of double-layer windings can be found. Different rules to find the winding layout of single-layer windings are defined in [51],

starting from the defined star of slot.

Figure B.2 illustrates this method with the example of a double-layer 28-pole, 24-slot PMSM. As can be seen, the phasors numbered 1, 8, 13, 20 and 2, 7, 14, 19 belongs to phase A. The winding layout is then completed as in step d) of Cros' method, and the same winding layout is found.

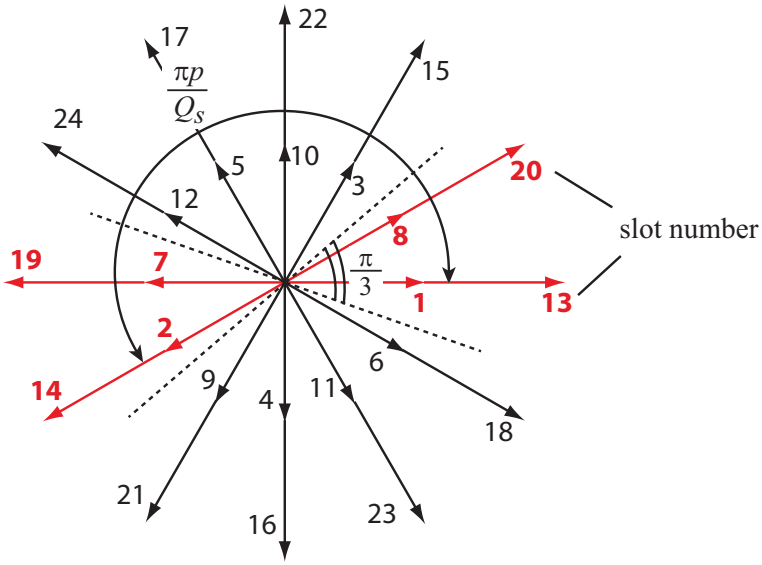

Figure B.2: Star of slot of a PMSM with Q_s=24 and $p = 28$.

C Prototype motor and measurement instruments

C.1 Characteristics

The calculations and measurements presented in Chapters 5-7 are performed on the prototype motor presented in this appendix. This motor has been built by Danaher Motion for a direct-drive low-speed application.

This motor has 28 poles, 24 slots and a double-layer concentrated windings. The PMs are in ferrite and mounted on the surface of the outer rotor. The stator is short (20 mm without end-windings) for a large diameter (400 mm), and the rotor with its PMs is longer than the stator (25 mm). Figure C.1.a and C.1.b show respectively the stator and rotor of the prototype motor.

This 800 W motor has a nominal speed of 200 rpm and can rotate over 1000 rpm at constant power under field-weakening operation. Table C.1 gives more characteristics of the motor.

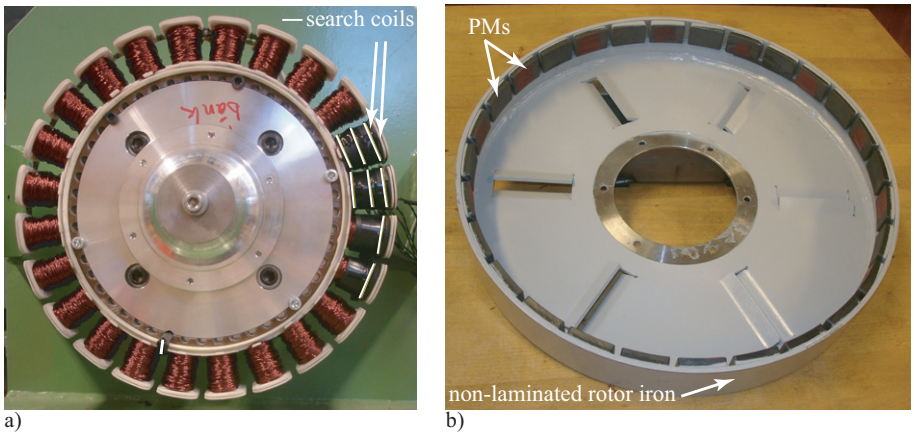

a) b)

Figure C.1: Prototype motor: a) Stator; b) Rotor

Table C.1: Some characteristics of the 28-pole, 24-slot prototype motor.

airgap thickness [mm]	1
magnet remanence flux density [T] at 25 deg	0.41
magnet relative permeability	1.04
RMS PM flux linkage Ψ_m [Wb]	0.25
RMS rated current I_r [A]	3.4
measured d-axis inductance L_d [mH]	0.96
flux-weakening index $\Psi_m/(L_d I_r)$	0.77
slot fill factor [%]	0.4

C.2 Instruments used during the measurements

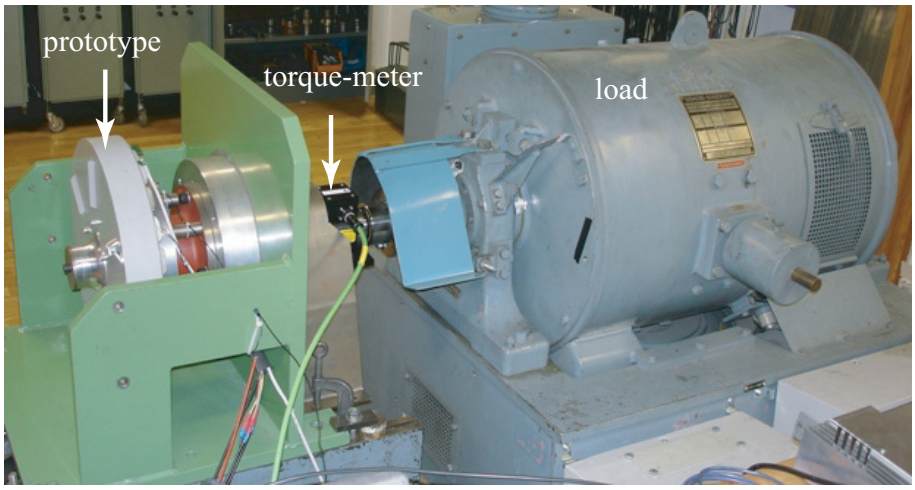

Figure C.2: Test bench for measurements at open-circuit and load conditions.

Figure C.2 shows the test bench for the measurements at open-circuit and load conditions. The motor is supplied by a PWM converter. The control consists of current controllers in dq system and a speed regulator. The motor speed is kept constant whatever the applied load torque (if the torque does not exceed the torque limit).

The followings instruments are used for the measurements at open-circuit and load conditions:

- Powers, RMS and waveforms of voltages and currents - Digital power analyzer Yokogawa WT3000.

- Torque and speed - Torque-meter Magtrol model TM311 with its torque transducer display, model 6400. Measurement range 0-100 Nm, minimum resolution 0.1 Nm, speed range 0-10000 rpm.
  Torque-meter Ono Sokki model SS200, measurement range 0-20 Nm, minimum resolution 0.01 Nm, speed range 0-8000 rpm.
- Windings temperature - Data acquisition / switch unit HP 34970A connected to a thermocouple type J in the windings.

The sinusoidal voltage supply used for the test at blocked rotor (Method I and II in Chapter 6) is an Elgar 1751B.

D Open-circuit airgap flux density for tangentially-magnetized buried PM motors

The analytical model of the open-circuit airgap flux density used for the tangentially-magnetized buried PM motors is presented here. Correction factors determined from few FE-simulations are defined in order to be able to compare fairly and quickly different designs of this machine obtained with the optimization procedure.

D.1 Analytical calculation of the open-circuit airgap flux density

The calculation of the maximum open-circuit airgap flux density B_m is determined from the Ampere's law and the equivalent magnetic circuit of the motor (Figure D.1). The considered part of the PM is seen as a constant magneto-motive force source $H_m l_m$, in series with a constant internal reluctance $\Re_m$. H_m is the coercive magnetic field intensity of the magnet.

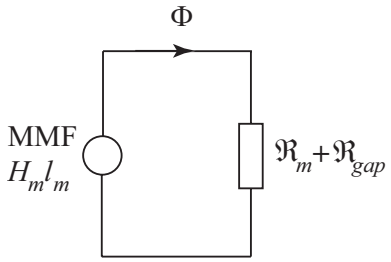

Figure D.1: Equivalent magnetic circuit for half a pole (half a PM and airgap for half iron width).

$$H_m l_m = \frac{B_r}{\mu_0 \mu_r} l_m \tag{D.1}$$

and

$$\Re_m = \frac{l_m}{\mu_0 \mu_r L w_m} \tag{D.2}$$

The airgap reluctance is equal to:

$$\Re_{gap} = \frac{\delta k_C}{\mu_0 L l_{iron}} \tag{D.3}$$

with k_C the Carter factor and l_{iron} defined in Figure D.2 and:

$$l_{iron} = \left(\frac{\pi}{2} - \alpha\right) \frac{D_{rc}}{p}. \tag{D.4}$$

α is the magnet angle. Assuming that the permeability of iron is infinite, the following equation can be obtained from the equivalent lumped circuit:

$$H_m l_m = (\Re_m + \Re_{gap})\Phi \tag{D.5}$$

where the flux Φ is:

$$\Phi = B_m L l_{iron} \tag{D.6}$$

Finally B_m is given by:

$$B_m = \frac{B_r}{1 + \frac{\mu_r \delta k_C w_m}{l_m l_{iron}}} . \frac{w_m}{l_{iron}} \tag{D.7}$$

The approximation used to calculate the fundamental airgap flux density is described in Figure D.2. As illustrated in the figure, a factor $k_{leak\alpha}$ is introduced to correct the pole angle. It is determined from FE simulations:

- $k_{leak\alpha} = 1$ for $B_m \leq 0.9\,\mathrm{T}$
- $k_{leak\alpha} = 0.9$ for $0.9\,\mathrm{T} < B_m \leq 1\,\mathrm{T}$
- $k_{leak\alpha} = 0.8$ for $1\,\mathrm{T} < B_m$

D.2 Comparison with results from FE-simulations

Table D.1 shows how accurate the analytical calculations are, compared with the respective FE values. This model is restricted to the B/H curve of the iron used for the simulations.

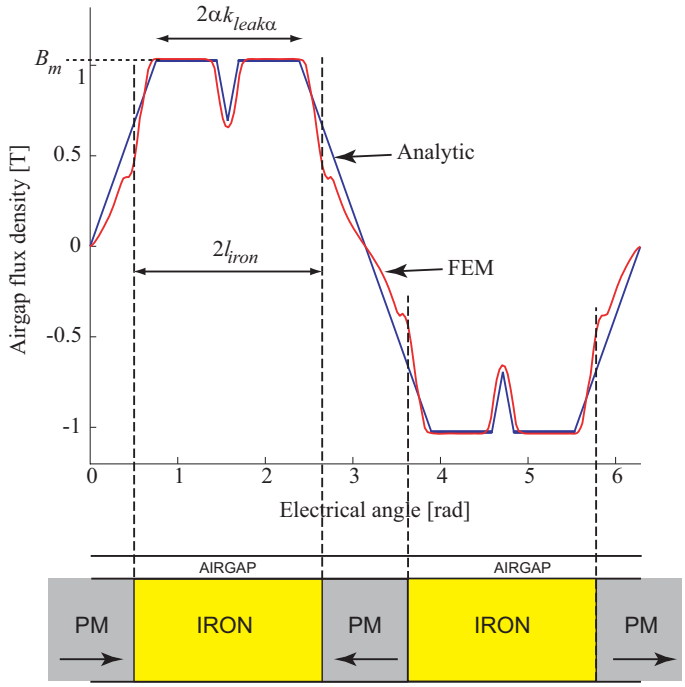

Figure D.2: FE simulated and analytically calculated flux densities in the airgap for a tangentially-magnetized PM motor.

Table D.1: Comparison of analytical and FE values of the fundamental airgap flux density for tangentially-magnetized PM motors.

Pole number		30	40	50	60	70
$k_{leak\alpha} = 0.8$ $1\,\mathrm{T} < B_m$	$\hat{B}_{\delta,an}$ [T]	1.06	1.10	1.10	1.09	1.03
	$\hat{B}_{\delta,FEM}$[T]	1.09	1.06	1.12	1.11	0.99
	Relative error [%]	-2.7	3.8	-1.8	-1.8	4.0
$k_{leak\alpha} = 0.9$ $0.9\,\mathrm{T} < B_m \leq 1\,\mathrm{T}$	$\hat{B}_{\delta,an}$ [T]	1.10	1.03	0.98	0.99	0.96
	$\hat{B}_{\delta,FEM}$[T]	1.08	1.03	0.93	0.97	0.96
	Relative error [%]	2.0	0	5.3	2.0	0
$k_{leak\alpha} = 1$ $B_m \leq 0.9\,\mathrm{T}$	$\hat{B}_{\delta,an}$ [T]	1.05	1.00	0.93	0.89	0.92
	$\hat{B}_{\delta,FEM}$[T]	1.01	1.00	0.91	0.84	0.88
	Relative error [%]	4.0	0	2.2	5.9	4.5

E FE models and simulations

2D- and 3D-FE tools are used to simulate the prototype motor and verify the analytical models developed for the design of the mixer motor. These tools are powerful as the saturation of the magnetic circuit can easily be taken into account. The FE models of the prototype motor, as well as the performed simulations are described in this appendix. The software Flux from Cedrat has been used for the simulations.

E.1 Models

E.1.1 2D-FE model

With a 2D-FE model, the simulating time is much shorter than in 3D. Another advantage is the possibility to plot the equiflux lines, which helps to understand more easily some phenomena. Half of the machine is modelled because of the symmetry in the winding layout ($X = gcd(p/2,Q_s) = 2$). The axial length of the machine is set to the length of the stator lamination stack, i.e. 20 mm.

E.1.2 3D-FE model

The 2D-FE model is used to construct the 3D-FE model. In 3D, the rotor can be modelled with a larger axial length than the stator lamination stack. As the machine is short, the end-effects that are neglected in 2D can be taken into account in 3D. Figure E.1 shows the geometry of the modelled stator and rotor, the rotor being rotated. A quarter of the machine is modelled due to one axial and one radial symmetry. Part of the mesh is shown in Figure E.2. A large volume over the iron lamination that includes the end-windings is meshed. There are around 300 000 volume elements in the model. The coils are modelled as shown in Figure E.3. They are not meshed. The search coils and grids employed in Chapter 7 can be seen in Figure E.3 and E.4 respectively. The coils are coupled to an electrical circuit that is presented in the next section.

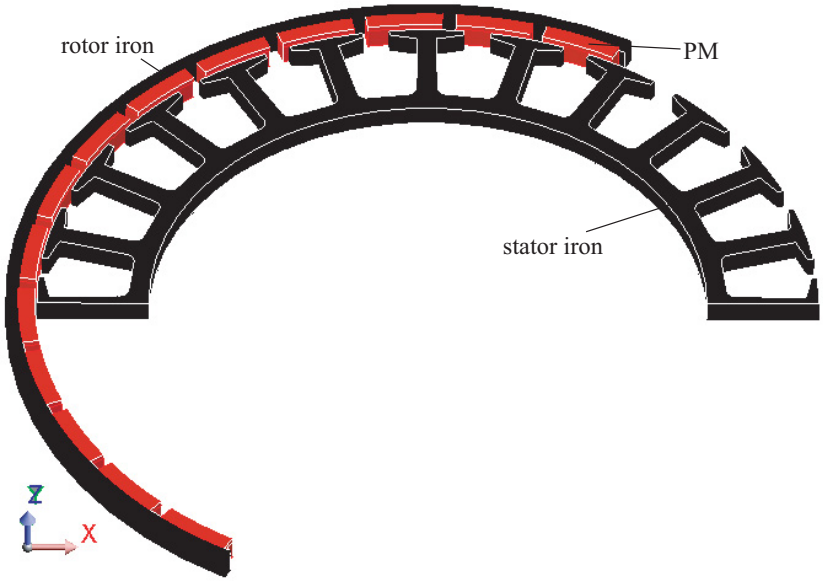

Figure E.1: Geometry of the 3D-FE model of the prototype motor.

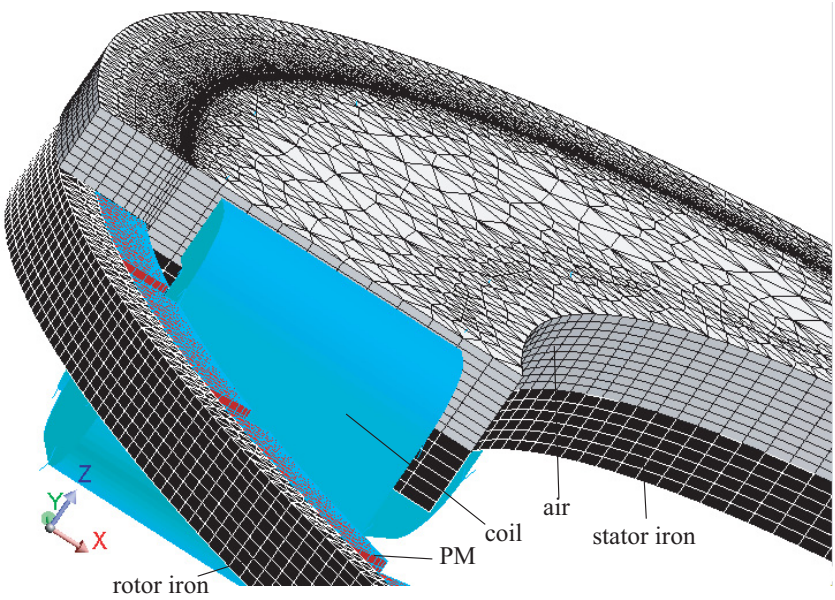

Figure E.2: Part of the meshed 3D-FE model.

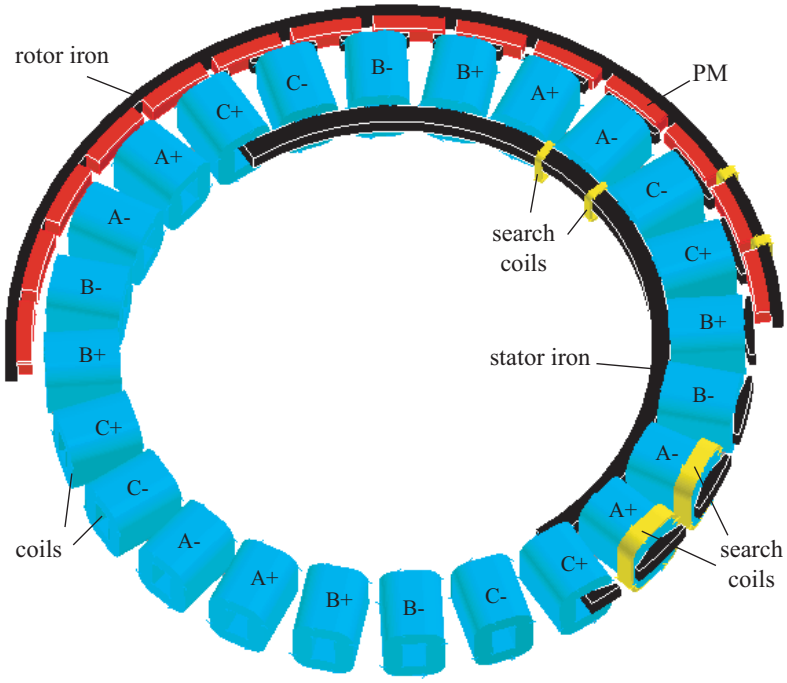

Figure E.3: Winding coils and search coils in the 3D-FE model.

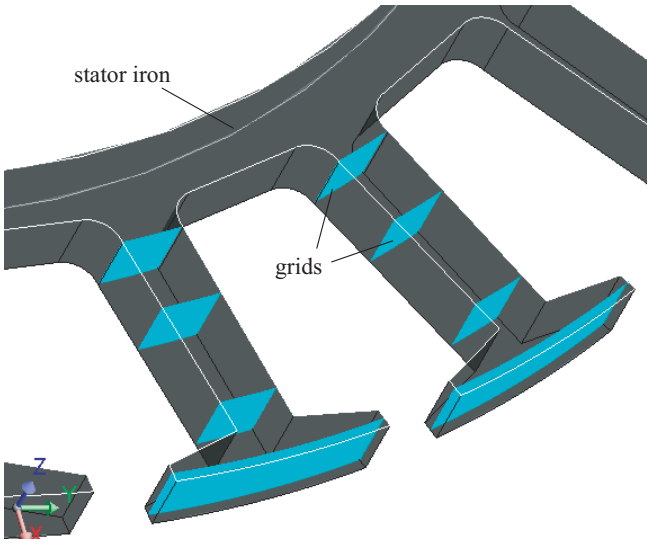

Figure E.4: Grids used for the calculation of the flux density in Chapter 7.

E.2 Simulations

The results from 3 types of simulations are presented in this thesis. The performed FE simulations are time-step computations at zero or constant speed with 80 steps over an electrical period.

E.2.1 Simulations at open-circuit condition

The open-circuit condition is simulated by using the circuit shown in Figure E.5. In this circuit, the coils are coupled to the coils of Figure E.3. The resistances are very large so that the current in the coils is negligible. The rotor is rotating at a constant speed. The open-circuit airgap flux density, PM flux linkage, back-EMF, and cogging torque can be computed from this simulation.

E.2.2 Simulations to obtain the inductances

Blocked rotor
The test to obtain the inductance from method I and II in Chapter 6 is simulated using the circuit shown in Figure E.6. Two phases of the windings are parallel connected and supplied with a sinusoidal current. The rotor speed is set to zero. The flux-linkage seen by the phases as well as the magnetic energy in different regions can be computed.

Inductance as a function of the position
To obtain the inductance as a function of the position, as in Figure 6.3, no circuit is required. The rotor is rotating at a constant speed and the coils are supplied with a constant current.

E.2.3 Simulations at load conditions

In order to avoid any transients in the FE-computation, the load is simulated by supplying the windings with sinusoidal currents and rotating the rotor at a constant speed. The circuit that is coupled to the FE-model is given in Figure E.7. The coils of the circuit are coupled to the search coils and connected to very large resistances. Two current sources are connected in parallel in order to easily decompose the current in d- and q- axes. The torque and iron losses can be computed from this simulation.

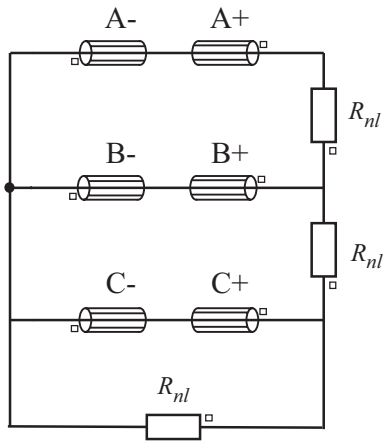

Figure E.5: Circuit used for FE simulations at open-circuit condition.

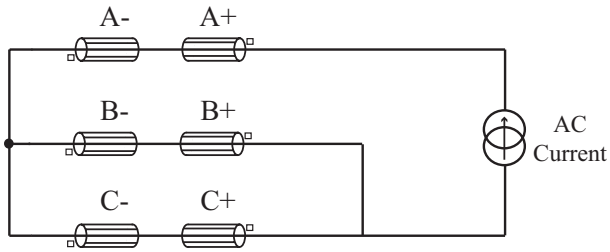

Figure E.6: Circuit used for FE simulations with blocked rotor and AC current.

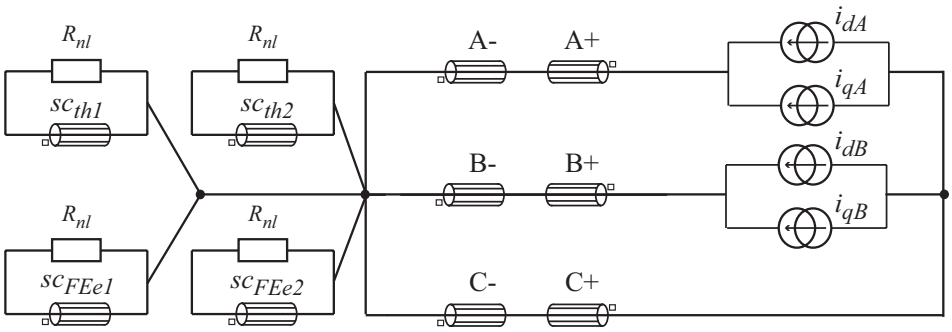

Figure E.7: Circuit used for FE simulations at load conditions.